UNIVERSITY OF CALIFORNIA
Los Angeles

Heat Pipe Vapor Dynamics

A dissertation submitted in partial satisfaction of the
requirements for the degree Doctor of Philosophy
in Mechanical Engineering

by

Farrokh Issacci

1990

To Shalva, Dror, and Adiel

CONTENTS

LIST OF FIGURES

List of Tables

NOMENCLATURE

A_w	wick cross sectional area
b	channel width
C	concentration
C_t	terminal velocity
c_p	specific heat
d	beam diameter
f	friction factor
g	gravity acceleration
h_{fg}	latent heat
K	wick permeability
k	thermal conductivity
L	heat pipe length
L_a	adiabatic section length
L_c	condenser length
L_e	evaporator length
l	test section width
M	molecular weight
m	total mass

$\dot{m}$	mass flux
N	molar refractivity
n	refractive index
p	pressure
$\bar{p}$	space averaged pressure
$\tilde{p}$	pressure deviation
Pr	Prandtl number
$\dot{q}$	input heat flux
R	gas constant
Re	Reynolds number
r	radius of curvature
r_h	hydraulic radius
r_p	particle radius
S	interference order
St	Stokes number
T	temperature
t	time
U	perpendicular velocity component of particle
U_s	shifted velocity
u	axial velocity
V	volume
v	vertical velocity
x	axial coordinate
y	vertical coordinate

α	thermal diffusivity
ε	wick porosity
δ	liquid layer thickness
Δp	pressure drop
Δz	fringe spacing
λ	wavelength
μ	viscosity
ν_D	Doppler frequency
ν_S	shifted frequency
ρ	density
σ	surface tension
τ	Fourier number
φ	inclination angle
ϕ	angle between two beams
θ	liquid contact angle
ω	oscillation frequency

Subscripts

a	adiabatic
a,b	mixture components
c	condenser
cap	capillary
e	evaporator
eff	effective

f	fluid
g	gravity
j	wavelength 457.9 nm
k	wavelength 632.8 nm
l	liquid
in	input
out	output
p	particle
sat	saturation
v	vapor

Acknowledgments

I wish to express my profound gratitude to my advisors, Professors Ivan Catton and Nasr Ghoniem, for the support and assistance they have continuously provided over the past four years. I am also thankful to the other committee members, Professors Lavine, Smith and Anderson, for their participation and review of the transcript. Special thanks are extended to Professor James McDonough for his guidance and help.

The supports by NASA Lewis, NASA Dryden and Department of Energy are gratefully acknowledged.

VITA

[redacted] Born, [redacted]

1980	B.Sc., Mechanical Engineering Pahlavi University Shiraz, Iran
1981-85	Research and Teaching Assistant Technion-Israel Institute of Technology Haifa, Israel
1985	M.Sc., Mechanical Engineering Technion-Israel Institute of Technology Haifa, Israel
1985-89	Post Graduate Research Engineer Department of Mechanical Engineering University of California, Los Angeles
1987-89	Teaching Associate Department of Mechanical Engineering University of California, Los Angeles

Publications

Issacci, F., Catton, I., and Ghoniem, N. M., "Vapor Dynamics of Heat Pipe startup," submitted for publication in *J. Heat Transfer*, 1990.

Issacci, F., McDonough, J. M., Catton, I., and Ghoniem, N. M., "Non-linear Filtering for Shock Capturing and Cell-Reynolds Number Problems in Compressible Vapor Dynamics," submitted for publication in *J. Comp, Phys.*, 1990.

Issacci, F., Catton, I., and Ghoniem, N. M., "Modeling of Startup Transient of Vapor Flow in Heat Pipes," *Proceedings, 9th International Heat Transfer Conf.*, Jerusalem, Israel, 1990.

Stroes, G., Fricker, D., Issacci, F., and Catton, I., "Heat Flux Induced Dryout and Rewet in Thin Films," *Proceedings, 9th International Heat Transfer Conf.*, Jerusalem, Israel, 1990.

Issacci, F., Ghoniem, N. M., and Catton, I., "Vapor Flow Patterns During Startup Transient in Heat Pipes," *Proceedings, the 5th AIAA/ASME Joint Thermophysics and Heat Transfer Conf.*, Seattle, Washington, 1990.

Marn, J., Issacci, F., and Catton, I., "Measurements of Temperature and Concentration Fields in Rectangular Heat Pipes," *Proceedings, the 5th AIAA/ASME Joint Thermophysics and Heat Transfer Conf.*, Seattle, Washington, 1990.

Issacci, F., Catton, I., and Ghoniem, N. M., "Vapor Dynamics of Heat Pipe Startup," *Proceedings, 7th Sypm. on Space Nuclear Power Systems*, Vol. 2, pp 1002-1007, Albuquerque, NM, 1990.

Roche, G. L., Issacci, F., and Catton, I., "Liquid Phase Transient Behavior of a High Temperature Heat Pipe," *Proceedings, 7th Sypm. on Space Nuclear Power Systems*, Vol. 2, pp 875-882, Albuquerque, NM, 1990.

Marn, J., Issacci, F., and Catton, I., "The Use of Single Beam Holographic Interferometry in Temperature Measurements in Rectangular Heat Pipes," *Proceedings, 7th Sypm. on Space Nuclear Power Systems*, Vol. 2, pp 995-1001, Albuquerque, NM, 1990.

Stroes, G., Fricker, D., Issacci, F., and Catton, I., "Studies of Wick Dryout and Rewet," *Proceedings, 7th Sypm. on Space Nuclear Power Systems*, Vol. 2, pp 1008-1010, Albuquerque, NM, 1990.

Issacci, F., Catton, I., Heiss, A., and Ghoniem, N. M., "Analysis of Heat Pipe Vapor Flow Dynamics," *Chem. Eng. Comm.*, Vol. 85, pp 85-94, 1989.

Issacci, F., Ghoniem, N. M., and Catton, I., "MHD Flow in Curved Pipes," *J. Physics of Fluids*, Vol. 31, No. 1, pp 65-71,1988.

Issacci, F., Zvirin, Y., and Grossman, G., "Heat Transfer Analysis of a Finned Solar Air Heater," *ASME, J. Solar Eng.*, Vol. 110, No. 2, PP 145-155, 1988.

Catton, I., Issacci, F., and Heiss, A., "Use of Optical Methods for Study of the Dynamic Behavior of Heat Pipes," *Proceedings, 1st World Conf. on Experimental Heat Transfer, Fluid Mechanics and Thermodynamics*, pp 1656-1661, Dubronick, Yugoslavia, 1988.

Issacci, F., Catton, I., Heiss, A., and Ghoniem, N. M., "Analysis of Heat Pipe Vapor Flow Dynamics," *Proceedings, 25th National Heat Transfer Conf.*, Vol. 1, pp 361-365, Houston, TX, 1988.

Issacci, F., Roche, G. L., Klein, D. B., and Catton, I., "Heat Pipe Vapor Dynamics," *Report, UCLA-ENG-88-28,* University of California Los Angeles, 1988.

Issacci, F., "Analysis of Finned Solar Air Heaters," *M.Sc. Thesis*, Technion, IIT, Haifa, Israel, 1985.

ABSTRACT OF DISSERTATION

Heat Pipe Vapor Dynamics

by

Farrokh Issacci
Doctor of Philosophy in Mechanical Engineering
University of California, Los Angeles, 1990
Professor Ivan Catton, Co-chair
Professor Nasr M. Ghoniem, Co-chair

The dynamic behavior of the vapor flow in heat pipes is investigated at startup and during operational transients. The vapor is modeled as two-dimensional, compressible viscous flow in an enclosure with inflow and outflow boundary conditions.

For steady-state and operating transients, The SIMPLER method is used. In this method a control volume approach is employed on a staggered grid which makes the scheme very stable. It is shown that for relatively low input heat fluxes the compressibility of the vapor flow is low and the SIMPLER scheme is suitable for the study of transient vapor dynamics.

When the input heat flux is high or the process under a startup operation starts at very low pressures and temperatures,

the vapor is highly compressible and a shock wave is created in the evaporator. It is shown that for a wide range of input heat fluxes, the standard methods, including the SIMPLER scheme, are not suitable. A nonlinear filtering technique, along with the centered difference scheme, are then used for shock capturing as well as for the solution of the cell Reynolds-number problem. For high heat flux, the startup transient phase involves multiple shock reflections in the evaporator region. Each shock reflection causes a significant increase in the local pressure and a large pressure drop along the heat pipe. Furthermore, shock reflections cause flow reversal in the evaporation region and flow circulations in the adiabatic region. The maximum and maximum-averaged pressure drops in different sections of the heat pipe oscillate periodically with time because of multiple shock reflections. The pressure drop converges to a constant value at steady state. However, it is significantly higher than its steady-state value at the initiation of the startup transient.

The time for the vapor core to reach steady-state condition depends on the input heat flux, the heat pipe geometry, the working fluid, and the condenser conditions. However, the vapor transient time, for an Na-filled heat pipe is on the order of seconds. Depending on the time constant for the overall system, the vapor transient time may be very short. Therefore, the vapor core may be assumed to be quasi-steady in the transient analysis of a heat pipe operation.

Chapter I

INTRODUCTION

1.1 SCOPE

A heat pipe is a device which transfers heat by evaporating and condensing a fluid. A wick structure is used to return the liquid to the evaporation zone by capillary effect. Figure 1.1 shows a typical sketch of a heat pipe which consists of the case, the wick structure and the vapor space. The input heat at one end of the pipe increases the temperature of the liquid in the wick structure. The liquid then evaporates, the pressure in the vapor core increases and the vapor flows to the other end. At this end the temperature is lower and the vapor condenses and releases heat. The liquid, then, flows from the condenser to the evaporator by capillary action through the wick structure.

The heat pipe is considered as a heat transfer device with very high conductivity. It can operate in weightless environments and transfer a huge amount of heat under conditions of very low temperature differences. These advantages make the heat pipe unique in space applications, electronic cooling systems and fusion energy systems. Although the steady state operation of heat pipes is well established, the transient behavior is not entirely understood.

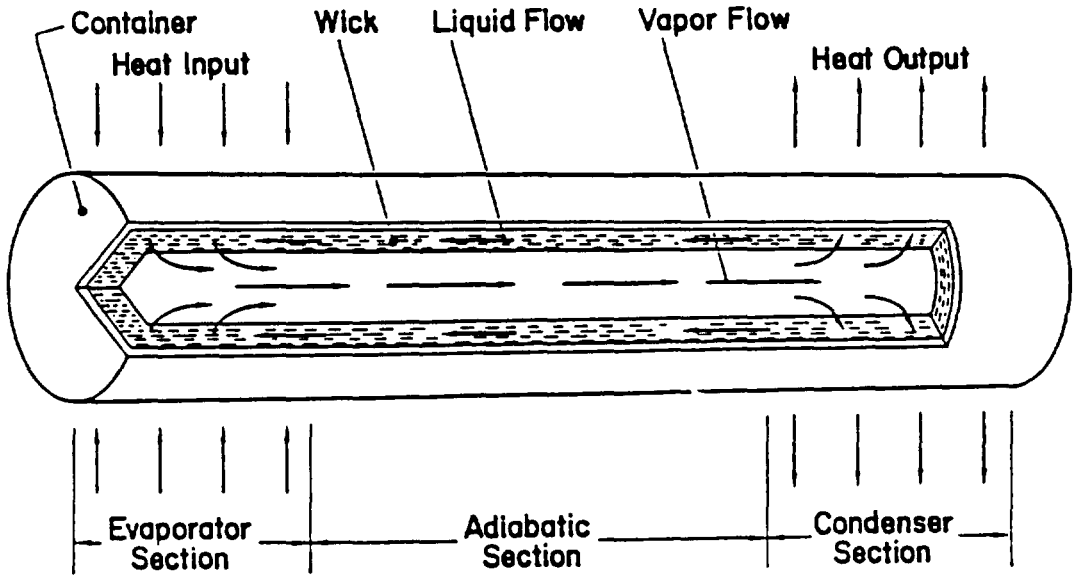

Fig. 1.1. Schematic of a heat pipe

The reliability of a heat pipe for space applications depends on its ability to respond to a sudden change in the heat load, and startup and shut down of the thermal system. A comprehensive experimental and theoretical study is needed to understand and properly model the physical phenomena which occur in heat pipes during operational transients.

1.2 HEAT PIPE APPLICATIONS

Gaugler [1] was the first to develop the concept of a heat pipe in 1942 proposing to apply heat pipes for cooling the interior of an ice box. During the early sixties, intensive work in this field was

started by Grover and his coworkers [2] at the Los Alamos National Laboratory. Their objective was to apply heat pipes in spacecraft designs. The first quantitative analysis of heat pipes was performed by Cotter in 1965 [3]. Since then there have been many advances in the theory, design and practice of heat pipes.

The fact that heat pipes are able to operate under very low gravity conditions and that they do not include any moving parts, has motivated the continued development of the heat pipe for space applications. In these applications, the temperature is very high ($1000\text{-}2000^{\circ}C$) and liquid metals (such as sodium and lithium) are used as working fluids.

A heat pipe was proposed by Grover [2] to supply heat to the emitters of thermionic electrical generators and to remove heat from the collectors of these devices. In space based nuclear power systems, heat pipes are considered as a means of transferring heat from the generating point to the radiators, providing a uniform temperature on the radiator surfaces [4].

Recently heat pipes have been proposed to be used in internal cooling of the leading edges of reentry vehicles and hypersonic aircrafts to reduce the peak temperature and alleviate the thermal gradients at the edge [5]. In this case, the working fluid (a liquid metal) which is initially in the solid state, is melted by the reentry heat load and the heat pipe operation is initiated. The use of high temperature heat pipes as a heat transfer device

has also been considered in rocket engines to cool and make the nozzles isothermal [6].

In case of a loss of coolant accident in a fusion reactor, it is desirable to ensure that no first wall melting or evaporation occurs. Such melting or evaporation of constituent elements can lead to the dispersal of radioactive waste hazards. In contrast to fission systems, a fusion power core usually contains enough thermal capacity to distribute the after-heat efficiently. Since the major component of decay after-heat is within a thin zone close to the first wall structure, a design incorporating heat pipes would result in an effective and fast redistribution of the decay after-heat. A heat pipe with a proper working fluid may be chosen such that the mechanism of heat transport through the pipe will start above a threshold design temperature. This would make the heat pipe operative only when needed, that is in the case of a loss of coolant accident.

1.3 THEORETICAL BACKGROUND

The theory of heat pipe operation is briefly outlined in this section. Pressure drop and heat flux in a heat pipe are discussed for engineering calculations along with the limits on the heat pipe operation. The section concludes with a discussion of the transient operation of heat pipes. The detailed explanation of heat pipe theory may be found in Dunn and Reay [7].

1.3.1 *Pressure Drop*

In order for heat pipes to operate, the capillary driving force in the wick, Δp_{cap}, must overcome the pressure drop in the liquid phase, Δp_l, in the vapor phase, Δp_v, and the gravitational head, if any, Δp_g. That is

$$\Delta p_{cap} \geq \Delta p_l + \Delta p_v + \Delta p_g \tag{1.1}$$

The pressure difference across the interface of liquid and vapor is

$$\Delta p = \frac{2\sigma \cos\theta}{r} \tag{1.2}$$

where σ is the surface tension, θ is the contact angle, and r is the radius of curvature.

Figure 1.2 illustrates the operational conditions of the vapor-liquid interface. The radius of curvature in the condenser section is very large, whereas evaporation causes the radius of curvature at the evaporator menisci to decrease. The difference between the radii of curvature in condenser and evaporator, provides the capillary force. Thus, the capillary driving force, using Equation 1.2, is

$$\Delta p_{cap} = 2\sigma\left(\frac{\cos\theta_e}{r_e} - \frac{\cos\theta_c}{r_c}\right) \tag{1.3}$$

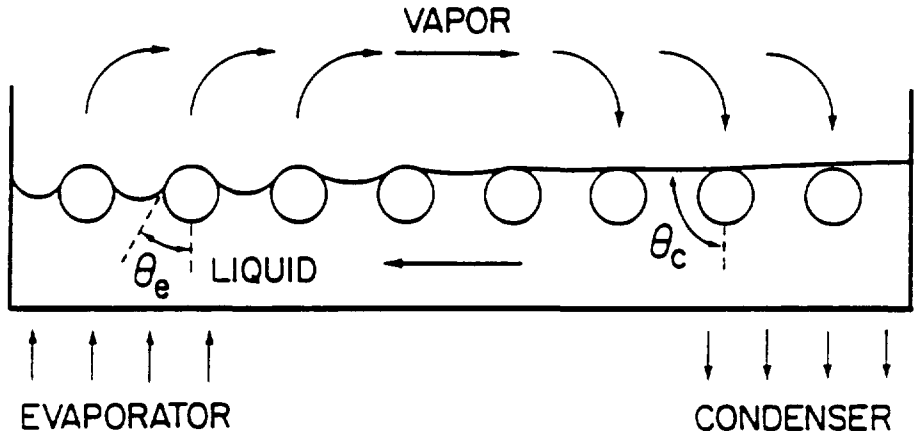

Fig. 1.2. Operational level of interface between liquid and vapor

where the subscripts e and c refer to evaporator and condenser, respectively, and r is the radius of the capillary pore. Usually r_c is very large with respect to r_e. This yields

$$\Delta p_{cap} \cong \frac{2\sigma\cos\theta}{r_e} \tag{1.4}$$

The pressure drop in the liquid phase, Δp_l, depends mainly on the structure of the wick and the properties of the liquid. For engineering calculations, the liquid phase is modeled as a liquid flow in a porous medium. Since the mass flow in the evaporator and condenser is not constant, an effective length, l_{eff}, is defined for the porous medium. The effective length, through which the mass flow is constant, is approximated as

$$l_{eff} = l_a + (l_e + l_c)/2 \tag{1.5}$$

where l_a is the length of the adiabatic section which is between the evaporator and condenser sections. l_e and l_c are the lengths of the evaporator and condenser. Thus, Darcy's law is used to relate the pressure drop in the liquid phase to the wick and liquid properties, i.e.,

$$\Delta p_l = \frac{\mu_l l_{eff} \dot{m}}{\rho_l K A_w} \tag{1.6}$$

where μ_l and ρ_l are viscosity and density of the liquid, $\dot{m}$ is the liquid flow rate, A_w is the wick cross sectional area and K is the wick permeability given by

$$K = \frac{2\varepsilon r_h^2}{f_l Re_l}$$

where ε is the wick porosity, r_h is the hydraulic radius and $f_l Re_l$ is the friction factor-Reynolds number product for laminar duct flow. The values of K for different types of wick structure are tabulated in Chi [8].

The pressure drop in the vapor phase, Δp_v, consists of the pressure drop in the adiabatic section, Δp_{va}, and the pressure drop in the evaporator, Δp_{ve}, and in the condenser, Δp_{vc}. That is,

$$\Delta p_v = \Delta p_{va} + \Delta p_{ve} + \Delta p_{vc} \tag{1.7}$$

In order to calculate the pressure drop in the adiabatic section, the vapor flow in this region is assumed to be laminar Poiseuille flow in a circular tube [7]. Then the pressure drop Δp_{va}, is given by

$$\Delta p_{va} = \frac{8\mu_v \dot{m} l_a}{\pi \rho_v r_v^4} \tag{1.8}$$

where r_v is the radius of the vapor core. Applying a one-dimensional analysis Cotter [3] calculated the pressure drop in the evaporator and condenser. The momentum equation was solved for the pressure gradient written as a perturbation expansion in powers of $1/Re$, where Re is the radial Reynolds number. The calculations resulted in

$$\Delta p_{ve} = \frac{\dot{m}^2}{8\rho_v r_v^4} \tag{1.9a}$$

$$\Delta p_{vc} = \frac{-\dot{m}^2}{2\pi^2 \rho_v r_v^4} \tag{1.9b}$$

Upon substituting Equations (1.8) and (1.9) in Equation (1.7), we get

$$\Delta p_v = \frac{8\mu_v \dot{m} l_a}{\pi \rho_v r_v^4} + 0.074 \frac{\dot{m}^2}{\rho_v r_v^4} \tag{1.10}$$

However, Busse [9], by using a modified Poiseuille velocity profile in Navier-Stokes equations, has shown that Δp_v can be expressed as

$$\Delta p_v = \frac{8\mu_v \dot{m} l_{eff}}{\pi \rho_v r_v^4} \tag{1.11}$$

where l_{eff} is defined in Equation (1.5).

The hydrostatic head, Δp_g, is written as

$$\Delta p_g = g \rho_l L \sin\varphi \tag{1.12}$$

where φ is the inclination angle of the heat pipe and L is the total length of the heat pipe.

Upon substituting Equations (1.6), (1.11) and (1.12) into Equation (1.1), the circulation rate, $\dot{m}$ is given by

$$\dot{m} = \frac{\Delta p_{cap} - g \rho_l L \sin\varphi}{l_{eff}\left(\frac{\mu_l}{\rho_l K A_w} + \frac{8\mu_v}{\pi \rho_v r_v^4}\right)} \tag{1.13}$$

1.3.2 *Heat Flux*

Neglecting the sensible heat which is small compared to the latent heat, the axial heat flux rate, $\dot{q}$, is given by

$$\dot{q} = \dot{m} h_{fg} \tag{1.14}$$

where, $\dot{m}$ is the circulation rate of the working fluid and h_{fg} is the latent heat of evaporation.

From Equations (1.13) and (1.14) the heat transfer rate can be expressed as a function of the capillary driving force, the geometry and the properties of the working fluid; i.e.,

$$\dot{q} = \frac{\left(\Delta p_{cap} - g\rho_l L \sin\varphi\right) h_{fg}}{l_{eff}\left(\frac{\mu_l}{\rho_l K A_w} + \frac{8\mu_v}{\pi \rho_v r_v^4}\right)} \tag{1.15}$$

1.3.3 *Limitations*

There are several limitations on the output heat transported through heat pipes, during the steady state or transient operations. These limitations are briefly described below [8].

1. Viscous limit: In long pipes and at low temperatures, the vapor pressure is low and the effect of viscous friction on the vapor flow may dominate inertial forces. In this situation the circulation of the working fluid is limited, which consequently, limits the heat transfer through the pipe.

2. Sonic limit: At low vapor pressures, the velocity of the vapor at the exit of the evaporator may reach the speed of sound. Then the evaporator cannot respond to further decrease in the condenser

pressure (i.e., the vapor flow is choked), which limits the vapor flow rate.

3. Capillary limit: A capillary structure is able to provide circulation of a given fluid up to a certain limit. This limit depends on the permeability of the wick structure and the properties of the working fluid.

4. Entrainment limit: The vapor flow exerts a shear force on the liquid in the wick which flows opposite the direction of the vapor flow. If the shear force exceeds the resistive surface tension of the liquid, the vapor flow entrains small liquid droplets (Kelvin-Helmholtz instabilities). The entrainment of liquid increases the fluid circulation but not the heat transfer through the pipe. If the capillary force cannot accommodate the increased flow, dryout of the wick in the evaporator may occur.

5. Boiling limit: At high temperatures, nucleate boiling may take place which produces vapor bubbles in the liquid layer. The bubbles may block the wick pores and decrease the vapor flow. Furthermore, presence of bubbles decreases the conduction of heat through the liquid layer which limits the heat transfer from the heat pipe shell to the liquid which is by conduction only.

The above limits are fully explained in several textbooks (for example, Chi [8]) which explain how they are to be determined. These limitations dictate the operational envelope for a given design of a heat pipe, as shown schematically in Fig. 1.3 [2]. The

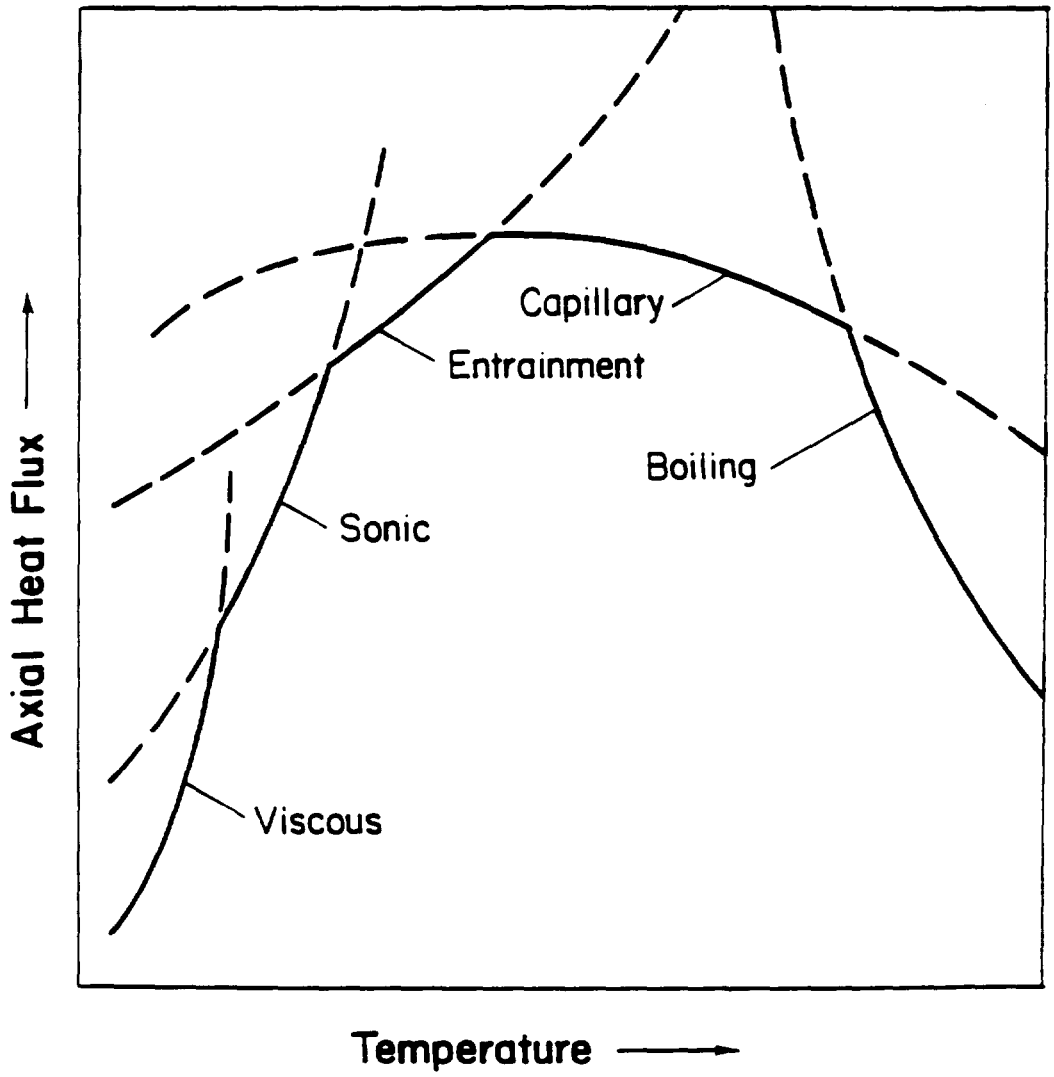

Fig. 1.3. Heat pipe operating limits

shape of the operational envelope changes for different working fluids and different wick materials.

1.3.4 *Transient Operation*

Transient operation of heat pipes may be considered in terms of three different regimes: startup, operating transients and shut down. The following is a brief description of these regimes.

Startup

Heat pipe startup is a transient process through which the heat pipe starts its operation from an static condition. The working fluid of a heat pipe may initially be very cold or frozen in the wick. Under this condition, the vapor pressure is very low and the vapor flow is free molecular. The heat transferred from the evaporator melts the frozen working fluid in the evaporator and evaporation takes place at the liquid-vapor interface. The vapor pressure is initially very low and the vapor flow is highly accelerated. Then the flow may be choked at the exit from the evaporation zone if its velocity reaches the sonic velocity. By addition of heat, the frozen working fluid is completely melted and continuum vapor flow prevails throughout the vapor core.

Behavior of the vapor flow during the startup of a heat pipe from a frozen state may be considered in three distinct phases: *(i)* free molecular flow throughout the vapor core, *(ii)* establishment of continuum flow in the evaporation zone with a front, moving towards the condenser with possibility of choked flow at the evaporator exit and *(iii)* continuum flow of vapor throughout the vapor core.

Operating Transients

Operating transients involve power changes during nominal operating conditions. There are several transient conditions of interest. A heat pipe may operate in a low power stand-by mode but be required to quickly respond to full power operation. A heat pipe may also be required to perform under load-following conditions, which depend on changing demands of the power conversion system. A nuclear reactor control system may also require changes in heat generation that would have to be handled by the heat pipe system.

The physics of interest for these situations depend on the initial conditions, the rate of change and magnitude of input power and condenser conditions. A heat pipe operating in stand-by mode at low vapor pressure may encounter the sonic limit while powering up. Large temperature gradients and complex vapor dynamics would develop. After passing through the sonic-limited operation, or for a heat pipe initially operating at high vapor pressure, the capillary, entrainment and boiling limits are of concern.

Shut Down

Shut-down of a heat pipe refers to the transient process occurring when the power of the thermal system is shut-off. The input heat of the heat pipe is suddenly reduced to zero and the pipe cools down to a static condition. There are several problems encountered with this mode of transient operation. After the

power is shut off, the working fluid of the heat pipe cools down and eventually solidifies. This phase change may affect the wick structure. The screen sheets of the wick are very delicate structures with fine meshes. Freezing of the working fluid in the screen holes may damage the wick structure by tearing the screen. Also if for some reason, the working fluid freezes mainly inside the screen holes, it will cause a major reduction in the driving force of the liquid flow.

Another possible problem is the appearance of cracks or bubbles in the solidified mass of the working fluid. The presence of cracks or bubbles can decrease the conduction of heat in the solidified mass during the startup, thereby the subsequent startup time increases. Cracks can also cause strain on the structure of the heat pipe and the screen and fatigue may become a serious problem after many shut downs. A proper heat pipe design must take into account the problems involved in the shut down transient mode, in order to have a reliable and long lasting heat pipe.

1.4 LITERATURE REVIEW

The heat pipe studies were initiated by the experimental work of Grover et al. [2] and the quantitative analysis of Cotter [3]. Initial qualitative experiments were performed on heat pipes with water and sodium as working fluids. Cotter considered a right circular heat pipe with large length-to-diameter ratio. He

performed a simple one-dimensional analysis on the vapor flow to develop the general basic theory for quantitative engineering calculations of heat pipe operations.

The vapor flow in heat pipes is a complicated problem due to high nonlinearities of the governing equations and the inflow and outflow boundaries in the evaporator and condenser. Different approaches have been used to simplify the problem. In most of the work done so far, the vapor flow is analyzed under steady state conditions, in one- [10-13] and two-dimensions [14-24].

Banskton and Smith [14,15] developed numerical solutions for incompressible, steady state, two-dimensional vapor flow in a heat pipe. Their results show flow reversal in the condenser for radial Reynolds numbers larger than two. Indication of reverse flow is important in the design of a heat pipe in calculating the shear forces acting on the wick structure. Flow reversal may also affect the entrainment limit. They also found that the pressure profiles across the heat pipe were two dimensional. Their study recommended the solution of the complete (compressible) two dimensional Navier-Stokes equations to provide an accurate prediction of the pressure drop along the pipe.

McDonald et al. [16] analyzed a vapor flow in an enclosure in the presence of air as a noncondensible gas. The coupled governing equations for steady state two-dimensional flow were numerically solved to study the effects of air on the evaporation and condensation rates of the water heat pipe. They concluded that the

two-dimensionality of the flow field had a very small effect on the concentration of the noncondensible gas and on the temperature distributions in the vapor core.

However, Rohani and Tien [17,18] showed that in liquid metal gas-loaded heat pipes, a one-dimensional analysis is not adequate. This conclusion was explained by averaging the two-dimensional results over the cross section, and comparing these with those of a one-dimensional analysis [15]. They performed a numerical analysis of the steady state two-dimensional heat and mass transfer in the vapor gas region of a gas loaded heat pipe. Their results show that the vapor flow in the vicinity of the vapor-gas front is negligibly small and they concluded that heat and mass are transferred only by conduction and diffusion at the front. But, in an analysis done by Peterson and Tien [19], it was shown that the natural convection and radial diffusion have a significant effect on the noncondensible gas distribution in the vicinity of the vapor-gas front.

Gas controlled heat pipes (GCHP) were recently investigated by Galaktionov and his colleagues from the Moscow Energy Institute [20,21]. In their analysis, they included convection and diffusion across the front under heat loads considerably smaller than the sonic limit of heat pipe operation. Galaktionov et al. [20] presented a mathematical model for the incompressible, steady state, two dimensional problem for the heat and mass transfer in the region of the vapor-gas front in a GCHP. In their analysis, using

boundary layer assumptions in the evaporator zone, they applied an integral method and approximated the axial velocity by a fourth-order polynomial.

The same problem was analyzed by Galaktionov and Trukhanova [21], taking into account the compressibility of the vapor. By defining a stream function for the velocity field, the momentum equation was written in terms of the vorticity and stream function. The governing equations were solved numerically by the Gauss-Seidel method.

They also carried out experimental studies of a planar gas controlled heat pipe. The results show that the variations of temperature in axial and radial directions are quite comparable, which clearly demonstrates the two dimensional character of the problem. The velocity profiles show the reverse flows in the region of the vapor-gas front.

Reverse flow in the condenser section was also observed by Ooijen and Hoogindoorn [22] who performed experimental and numerical studies on heat pipe vapor flow. Their analysis was confined to a steady-state, incompressible, two-dimensional flow. They also found that the total pressure drop over the heat pipe, for high radial Reynolds numbers, was higher than that approximated by a Poiseuille flow model.

Narayana [23] performed a numerical study of incompressible, steady state, two-dimensional vapor flow. He showed that the pressure terms in the Navier-Stokes equations

could be eliminated by integrating the momentum equation in the axial direction, on the pipe cross section. In this analysis, using boundary layer assumptions, the radial pressure variation was neglected.

A double-walled concentric heat pipe was proposed by Faghri [24]. Two pipes with different diameters create an annular space for the vapor flow. The wick structures are attached to the inner surface of the outer pipe and the outer surface of the inner pipe. In this kind of heat pipe the area of heat transfer into and out of the pipe is increased and its efficiency of performance is expected to be higher. Faghri has carried out a numerical study of the vapor flow in such a double-walled heat pipe. He used an implicit marching finite difference method to solve the incompressible, steady state, two dimensional flow problem. His results show that for low Reynolds numbers, viscous effects dominate. For radial Reynolds numbers greater than one, pressure decreases in the vapor flow direction in the evaporator section, whereas it increases in the condenser section due to partial dynamic pressure recovery from the decelerating flow. For high radial Reynolds numbers, flow reversal was shown to occur in the condenser section.

In studies of the dynamic behavior of heat pipes, three different areas of concern are startup, shut-down and operational transients. Among these the startup mode of transient is the most difficult one. As mentioned above, the startup of a heat pipe may

be encountered with melting of the working fluid at solid state, free molecular flow of vapor and dry out and rewetting of the wick.

Extensive studies of startup and shut down operations of heat pipes [25-29] have been carried out at the Los Alamos National Laboratory. The objectives were the applications of high temperature, liquid metal heat pipes to space power system heat rejection. Experiments were performed on a long heat pipe with a molybdenum container. Using liquid sodium and potassium as working fluids, design characteristics of high temperature heat pipes have been evaluated. For the temperature range of 700 to $1600^{o}K$, the useable length of $30m$ with length-to-diameter ratio of 300 was found for potassium heat pipes, whereas for sodium heat pipes useful lengths of more than $40m$ with length-to-diameter ratio of 800 were predicted.

In the numerical studies by Castello et al. [29], heat pipe performance was modeled to include startup from the frozen state of the working fluid, with provision for free molecule flow of the vapor. Vapor core dynamics were simulated by a transient one dimensional compressible flow with friction and mass flow from the wick. The governing equations were solved using the KACHINA method [30], a numerical code is still under development. In the present status it requires 30 minutes of the Cray computational time per hour of actual time.

Bystrov and Goncharov [31] performed experimental and theoretical studies on a heat pipe with and without a foreign gas. The steady state operation and startup from a frozen state of liquid were analyzed. By averaging over the axial cross section, they solved unsteady, one dimensional governing equations for the vapor and liquid phases. Their numerical scheme could be run only for very small time steps (10^{-5} to $10^{-7}s$) because of numerical stability problems and as a result needed a large amount of computational time. In order to increase the time steps, they used a lumped parameter approach for heat balance and avoided calculations of detailed temperature distributions.

Figure 1.4 shows the qualitative features of the temperature fields for startup of a heat pipe with a noncondensible gas, predicted by Bystrov and Goncharov [31]. Sharp discontinuities in the temperature distribution are the result of shock waves at the deceleration of vapor from supersonic flow. The heat pipe being initially at a uniform temperature (curve 1), is heated up uniformly and melting takes place (curve 2). The temperature increases and an intensive evaporation begins. As the vapor flows into the condenser the velocity increases up to the local sonic speed (curves 3 and 4). The volume of the condenser occupied by vapor increases and the noncondensible gas front is compressed further into the condenser (curves 5, 6 and 7). Supersonic flow occurs over the length of the active condenser. Curves eight through ten show the shock reflection back to the evaporator.

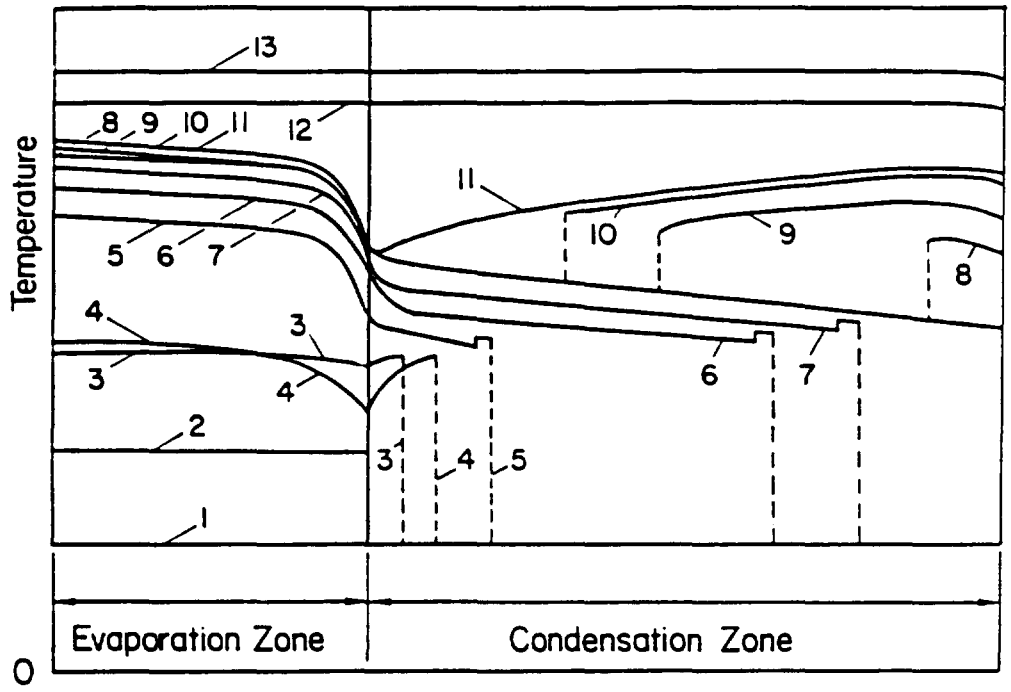

Fig. 1.4. Frontal startup temperature history of a gas-loaded heat pipe [31]

Further heating raises the vapor pressure and eliminates the shock wave (curve 11). Finally, the heat pipe reaches near isothermal conditions at its full operating temperature (curves 12 and 13).

Experimental studies of the heat pipe startup were performed by Ivanovskii et al. [32]. They measured the temperature distribution along a sodium heat pipe initially at frozen state at ambient temperature. Temperature measurements were made in the vapor by a moveable microthermocouple placed directly in the vapor core. Free molecule flow and transition to

continuum flow were observed at the early stages of the experiment. Then the vapor flow reached the sonic limit and a shock wave was created which caused an abrupt temperature drop. Non-isothermal conditions during sonic limit operation were seen to exceed 300 ^{o}C . Continuum vapor flow was found to occupy the whole vapor core and vapor pressure increased along the pipe. The process then proceeded to a steady state condition with an isothermal temperature distribution along the pipe. The transient time from a frozen state to a steady state condition was reported to be about ninety minutes.

Chang and Colwel [33-35] studied the transient operation of low temperature heat pipes experimentally and numerically. Experiments were performed with Freon 11 as a working fluid to study the dryout and rewetting of the liquid phase. The temperature range in experiments was between the room temperature and well above the critical temperature. At low heat fluxes, the liquid temperature was nearly uniform in the slab wick and only small gradient existed in the vapor. The measured transient time to reach steady state was about ninety minutes. At high heat fluxes, partial and complete drying of the wick were observed. In their analysis the vapor core temperature was assumed to vary with time only, allowing the solution of a two dimensional conduction problem for the liquid and wick structure.

Ambrose [36] studied the pulsed startup of heat pipes. A pulsed startup refers to applying a step increase in input heat flux

to a heat pipe under steady state conditions. They performed experiments on a simple-screen-wicked copper-water heat pipe to investigate the transient time and the dryout and rewetting behavior. The transient time was found to be dependent on the capillary force, the cooling mechanism and the heat capacity of the pipe. Dryout of the wick at the evaporator was found to occur only for heat fluxes greater than the capillary limit. Dryout and rewetting were modeled using a lumped parameter method. Good agreement between the experimental data and the theoretical results was reported.

Bowman [37] also studied the dynamics of vapor flow in heat pipes analytically and experimentally. In the experiments an air flow was pumped through a porous medium into a pipe at one end and sucked from the other end. The pressure and velocity field in the vapor core were measured. He also solved the steady state compressible, axisymmetric two-dimensional form of the Navier-Stokes equations numerically. Using the experimental and analytical results, he derived a friction coefficient expression to be used in a one dimensional transient model of heat pipe vapor flow. The friction coefficient is expressed as a function of local axial Reynolds number, Mach number, pipe aspect ratio and radial Reynolds number.

Recently Jang [38] studied an overall analysis of heat pipe startup from the frozen state, numerically. In this analysis, the conjugate problem of conduction in the heat pipe case and melting

and convection in the liquid phase is solved during the transient mode. In the vapor core, the free molecule flow, choked and continuum flow of vapor are taken into account, separately. However, the vapor core is assumed to be at steady state at any flow regime. This is rationalized by the fact that the transient time for vapor flow to reach a steady state is much shorter than that for the liquid flow.

1.5 OBJECTIVES

The research performed so far on the transient behavior of heat pipes mainly concerns the startup and shut down operations. However, these modes of transients are still not well established. Furthermore, no major work has been done on the operational transient of heat pipes. For a comprehensive study of the dynamics of heat pipes, the vapor flow should be thoroughly investigated theoretically and experimentally.

The previous theoretical studies of dynamics of vapor flow have considered a transient one-dimensional model. In these studies the friction coefficients of the vapor flow boundaries have been approximated using a steady state two-dimensional model. In addition, in steady state two-dimensional analyses it has been shown that the one-dimensional model of vapor flow is not able to accurately predict the axial heat and mass transfer and the axial pressure drops. Furthermore, two-dimensional steady-state studies indicate that flow reversal takes place in the condensation

section. It is therefore important to establish the conditions for this mode during transient operations.

The study of dynamic behavior of heat pipes at UCLA started by analyzing the liquid and vapor phases separately [39,40]. The objective was to develop very detailed computer codes for each phase, and then to combine them in a comprehensive code. Roche [39] developed a numerical code for the liquid phase during the startup transient mode by assuming the vapor phase at a constant temperature and pressure. He used a kinetic theory approach to model the phase change at the liquid-vapor interface. The model results in an expression which consists of a large coefficient multiplied by a very small temperature difference and requires very small time steps for stability. The large coefficient also transforms temperature differences that are otherwise beyond machine accuracy into computationally significant terms. He recommended investigation of an alternative model for the phase change process.

The objectives of this work are to investigate thoroughly the dynamic behavior of the vapor flow in heat pipes at startup and during operating transients. The vapor flow in a heat pipe is mathematically modeled and the equations governing the transient behavior of the vapor core are solved numerically. The modeled vapor flow is a transient, two-dimensional, compressible, viscous flow in a closed chamber. The boundary conditions include inflow and outflow of heat and mass which simulate the

boundaries of the vapor core in a heat pipe. The different solution methods are discussed and compared in Chapter Two. The numerical results of these methods are presented in Chapters Three through Five.

The need for and difficulties of experiments on the vapor core are then discussed in Chapter Six. In this Chapter the proper optical methods for temperature and velocity measurements are described along with the advantages and shortcomings of these methods. This Chapter also includes a rather simple but fundamental experiment to study the dryout and rewet of the liquid phase. Conclusions and recommendations of this work are given in Chapter 7.

Chapter II
THEORETICAL MODEL OF THE VAPOR CORE

2.1 INTRODUCTION

Flow patterns found in a heat pipe are shown schematically in Fig. 2.1. The working fluid evaporates in the evaporation zone. The local pressure increases and the vapor flows towards the condensation zone, at which it condenses back to the liquid phase. The liquid flows from the condenser to the evaporator by capillary force through the wick structure. The main concern of this analysis is the vapor core response to changes in the evaporation and condensation rates due to a sudden increase, or decrease, in the input heat flux, or the condenser temperature.

In this chapter the dynamic behavior of the vapor flow is analyzed using a transient two dimensional compressible flow model. The proper equations which govern the model problem will be written along with initial and boundary conditions which properly simulate heat pipe transient operations. Different numerical schemes and their advantages and disadvantages will then be discussed for different operational regimes. The

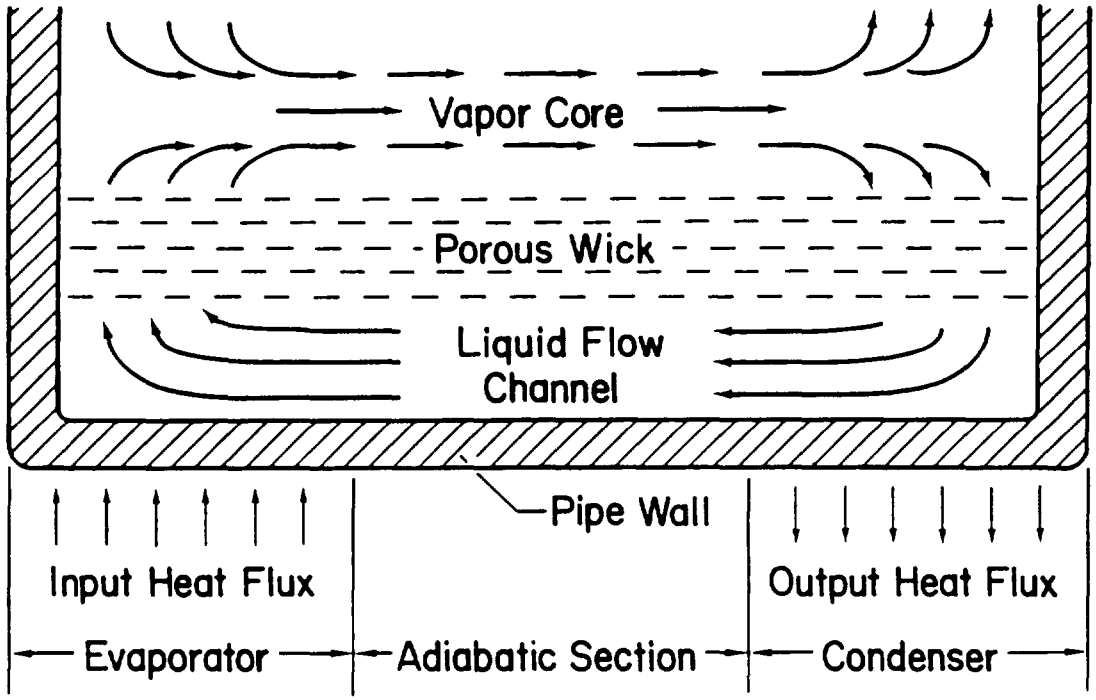

Fig. 2.1. Flow patterns in a heat pipe

application and numerical results of these schemes will be presented in Chapters Three through Five.

2.2 GOVERNING EQUATIONS

Vapor flow in the heat pipe vapor core, shown in Fig. 2.1, is modeled as a channel flow shown in Fig. 2.2. The bottom boundary of the channel is a thin porous medium which includes the liquid. The input heat flux to the evaporator and the temperature of the

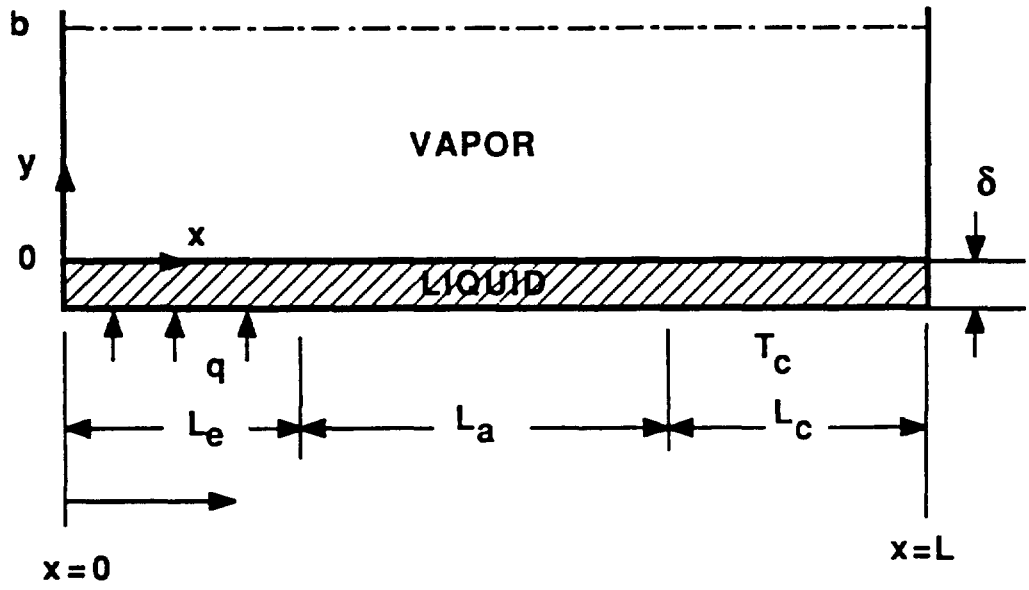

Fig. 2.2. Vapor core model of a heat pipe

outer surface of the condenser are specified. The planar side walls are assumed adiabatic.

The equations governing the vapor flow are time dependent, viscous, compressible momentum, continuity and energy equations. An equation of state is used to relate pressure, density and temperature within the vapor core. These equations in Cartesian coordinates (x',y') are

continuity

$$\frac{\partial \rho'}{\partial t'} + \frac{\partial (\rho' u')}{\partial x'} + \frac{\partial (\rho' v')}{\partial y'} = 0, \tag{2.1}$$

x-momentum

$$\frac{\partial (\rho' u')}{\partial t'} + \frac{\partial (\rho' u' u')}{\partial x'} + \frac{\partial (\rho' u' v')}{\partial y'} = -\frac{\partial p'}{\partial x'} + \frac{\partial}{\partial x'}\left(\mu' \frac{\partial u'}{\partial x'}\right) + \frac{\partial}{\partial y'}\left(\mu' \frac{\partial u'}{\partial y'}\right) + \left[\frac{\partial}{\partial x'}\left(\mu' \frac{\partial u'}{\partial x'}\right) + \frac{\partial}{\partial y'}\left(\mu' \frac{\partial v'}{\partial x'}\right) - \frac{2}{3}\frac{\partial}{\partial x'}\left(\mu' \frac{\partial u'}{\partial x'} + \mu' \frac{\partial v'}{\partial y'}\right)\right], \tag{2.2}$$

y-momentum

$$\frac{\partial (\rho' v')}{\partial t'} + \frac{\partial (\rho' u' v')}{\partial x'} + \frac{\partial (\rho' v' v')}{\partial y'} = -\frac{\partial p'}{\partial y'} + \frac{\partial}{\partial x'}\left(\mu' \frac{\partial v'}{\partial x'}\right) + \frac{\partial}{\partial y'}\left(\mu' \frac{\partial v'}{\partial y'}\right) + \left[\frac{\partial}{\partial x'}\left(\mu' \frac{\partial u'}{\partial y'}\right) + \frac{\partial}{\partial y'}\left(\mu' \frac{\partial v'}{\partial y'}\right) - \frac{2}{3}\frac{\partial}{\partial y'}\left(\mu \frac{\partial u'}{\partial x'} + \mu' \frac{\partial v'}{\partial y'}\right)\right], \tag{2.3}$$

energy conservation

$$c'_p\left[\frac{\partial (\rho' T')}{\partial t'} + \frac{\partial (\rho' u' T')}{\partial x'} + \frac{\partial (\rho' v' T')}{\partial y'}\right] = \frac{\partial}{\partial x'}\left(k' \frac{\partial T'}{\partial x'}\right) + \frac{\partial}{\partial y'}\left(k' \frac{\partial T'}{\partial y'}\right) + \frac{\partial p'}{\partial t'} + u' \frac{\partial p'}{\partial x'} + v' \frac{\partial p'}{\partial y'} + \mu'\left[2\left(\frac{\partial u'}{\partial x'}\right)^2 + 2\left(\frac{\partial v'}{\partial y'}\right)^2 + \left(\frac{\partial u'}{\partial y'} + \frac{\partial v'}{\partial x'}\right)^2\right], \tag{2.4}$$

state

$$p' = f(\rho', T'). \tag{2.5}$$

In these equations, ρ' is density, u' and v' are velocities in x' and y' directions, respectively, T' is temperature and p' is pressure. The properties μ', c'_p and k' are dynamic viscosity, specific heat and thermal conductivity of vapor, respectively.

In the momentum equations, 2.2 and 2.3, the last term in brackets accounts for compressibility of the fluid. Viscous dissipation in flows at high velocity or with high velocity gradients is not negligible. In heat pipe transient operations, where the vapor velocity may reach the speed of sound (sonic limit), with a large gradient at the initial stage of the process, the viscous dissipation is significant. This is taken care of by the last term in brackets in the energy equation 2.4. In the right hand side of the same equation, the terms involving pressure p', are presented owing to the compressibility of the flow.

2.2.1 *Normalization of the Equations*

The governing equations are normalized by using characteristic parameters of the problem, for parametric studies presented later. The characteristic length is the vapor core thickness, b. The characteristic velocity is related to the inflow mass flux of vapor in the evaporator, $\dot{m}''_c$; that is

$$\dot{m}''_c = \frac{\dot{q}''_o}{h_{fg}} \quad , \tag{2.6}$$

where $\dot{q}_o''$ is the maximum input heat flux and h_{fg} is the latent heat of vaporization. Then the characteristic velocity is

$$U_c = \frac{\dot{m}_c''}{\rho_r'} \quad , \tag{2.7}$$

In this equation ρ_r' is density of the vapor at a reference condition discussed below. Having the characteristic length and velocity, time is normalized by t_c, defined as

$$t_c = \frac{b}{U_c} = \frac{\rho_r' b}{\dot{m}_c''} \quad , \tag{2.8}$$

The normalized parameters are therefore defined as

$$\begin{aligned} &(x,y) = (x',y')/b, \qquad (u,v) = (u',v')/U_c, \qquad t = t'U_c/b, \\ &p = p'/(\rho_r' U_c^2), \qquad T = RT'/U_c^2 \end{aligned} \tag{2.9}$$

and

$$\varphi = \varphi'/\varphi_r' \quad , \tag{2.10}$$

where R is the gas constant. Here φ' is ρ', μ', k', or c_p' and the subscript r stands for the property value at a reference condition according to the initial conditions of the process.

The governing equations, 2.1 through 2.5, in nondimensional form, using normalized parameters, 2.9 and 2.10, are written as

$$\frac{\partial \rho}{\partial t}+\frac{\partial(\rho u)}{\partial x}+\frac{\partial(\rho v)}{\partial y}=0 \tag{2.11}$$

$$\begin{aligned}\frac{\partial(\rho u)}{\partial t}+\frac{\partial(\rho u u)}{\partial x}+\frac{\partial(\rho u v)}{\partial y}=&-\frac{\partial p}{\partial x}+\frac{1}{Re}\frac{\partial}{\partial x}\left(\mu\frac{\partial u}{\partial x}\right)+\frac{1}{Re}\frac{\partial}{\partial y}\left(\mu\frac{\partial u}{\partial y}\right)\\&+\frac{1}{Re}\left[\frac{\partial}{\partial x}\left(\mu\frac{\partial u}{\partial x}\right)+\frac{\partial}{\partial y}\left(\mu\frac{\partial v}{\partial x}\right)-\frac{2}{3}\frac{\partial}{\partial x}\left(\mu\frac{\partial u}{\partial x}+\mu\frac{\partial v}{\partial y}\right)\right]\end{aligned} \tag{2.12}$$

$$\begin{aligned}\frac{\partial(\rho v)}{\partial t}+\frac{\partial(\rho u v)}{\partial x}+\frac{\partial(\rho v v)}{\partial y}=&-\frac{\partial p}{\partial y}+\frac{\partial}{\partial x}\frac{1}{Re}\left(\mu\frac{\partial v}{\partial x}\right)+\frac{1}{Re}\frac{\partial}{\partial y}\left(\mu\frac{\partial v}{\partial y}\right)\\&+\frac{1}{Re}\left[\frac{\partial}{\partial x}\left(\mu\frac{\partial u}{\partial y}\right)+\frac{\partial}{\partial y}\left(\mu\frac{\partial v}{\partial y}\right)-\frac{2}{3}\frac{\partial}{\partial y}\left(\mu\frac{\partial u}{\partial x}+\mu\frac{\partial v}{\partial y}\right)\right]\end{aligned} \tag{2.13}$$

$$\begin{aligned}\left[\frac{\partial(\rho T)}{\partial t}+\frac{\partial(\rho u T)}{\partial x}+\frac{\partial(\rho v T)}{\partial y}\right]=&\frac{1}{RePrc_p}\left[\frac{\partial}{\partial x}\left(k\frac{\partial T}{\partial x}\right)+\frac{\partial}{\partial y}\left(k\frac{\partial T}{\partial y}\right)\right]+\\&\frac{\gamma-1}{\gamma c_p}\left[\frac{\partial p}{\partial t}+u\frac{\partial p}{\partial x}+v\frac{\partial p}{\partial y}\right]+\frac{\gamma-1}{\gamma c_p}\frac{\mu}{Re}\left[2\left(\frac{\partial u}{\partial x}\right)^2+2\left(\frac{\partial v}{\partial y}\right)^2+\left(\frac{\partial u}{\partial y}+\frac{\partial v}{\partial x}\right)^2\right]\end{aligned} \tag{2.14}$$

$$p=f(\rho,T) \tag{2.15}$$

The nondimensional parameters are Reynolds number, Re, Prandtl number, Pr, and specific heat ratio, γ, defined as

$$Re=\frac{\dot{m}_c''b}{\mu_r'},\qquad Pr=\frac{\mu_r'c_{p_r}'}{k_r'},\qquad \gamma=\frac{c_{p_r}'}{c_{v_r}'} \tag{2.16}$$

2.3 INITIAL AND BOUNDARY CONDITIONS

The working liquid is assumed initially at a very low temperature (close to the freezing point). Further there is no input heat and the stagnant vapor is in thermodynamic equilibrium with the liquid. The boundaries of the vapor core are shown in Fig. 2.2. A no-slip condition for the velocity and an adiabatic condition for the temperature are assumed on the side walls:

@ $x = 0$ and $x = L$,

$$u = 0 \quad , \qquad v = 0 \quad , \qquad \frac{\partial T}{\partial x} = 0. \tag{2.17}$$

On the center line the symmetry condition implies,

@ $y = b$,

$$\frac{\partial u}{\partial y} = 0 \quad , v = 0 \quad , \quad \frac{\partial T}{\partial y} = 0. \tag{2.18}$$

The boundary conditions at the liquid-vapor interface are the challenging ones. The liquid flow is assumed to be in a porous medium of thickness δ which is much smaller than the vapor core thickness b. The axial velocity is assumed zero on this boundary. That is,

$$@\ y = 0 \quad , \qquad u = 0 \, . \tag{2.19}$$

To assign boundary conditions for the temperature and vertical velocity, the liquid-vapor interface is divided into three regions. In the evaporation zone the input flux, $\dot{q}''$, is a given parameter and the input flow is approximated by,

@ $y = 0$ and $0 < x \leq L_e$,

$$\rho v = \dot{m}'' \approx \frac{\dot{q}''}{h_{fg}(T)} \quad , \qquad T = T_{sat(p)} \cdot \tag{2.20}$$

In the above equation, h_{fg} is the heat of vaporization and conduction in the liquid layer is neglected. The temperature is assumed to be the saturation temperature of the liquid corresponding to the interface pressure. In the adiabatic zone the boundary conditions are

@ $y = 0$ and $L_e < x \leq (L_e + L_C)$,

$$v = 0 \quad , \qquad \frac{\partial T}{\partial y} = 0. \tag{2.21}$$

In the condensation zone the temperature of the outer surface, T_C is given. By equating the heat of evaporation to the heat conduction in the liquid layer, the outflow from this region is approximated by,

@ $y = 0$ and $(L_e + L_C) < x \leq L$,

$$\rho v = \dot{m}'' \approx -\frac{k_{eff}}{\delta}\left(\frac{T - T_C}{h_{fg}(T)}\right) \quad , \; T = T_{sat(p)} \, , \tag{2.22}$$

where k_{eff} is the effective conductivity of the liquid layer and the temperature is assumed to be the saturation temperature corresponding to the pressure at the interface. This neglects transient conduction in the fluid layer which may be an important contribution to the process.

2.4 SOLUTION METHODS

The five governing equations, (2.11) to (2.15) are solved numerically for the five variables, ρ, ρu, ρv, T and p. The boundary conditions associated with these equations are Eqs. (2.17) to (2.22). The boundary conditions on the vapor-liquid interface depend on the interface pressure, which is not known a priori. However, in the numerical methods described below, the pressure does not need to be specified on the boundaries, and is not calculated there. After completion of calculations, an interpolation method is used to determine the pressure on the boundaries.

For low compressible flow, Issacci et al. [41] showed that the staggered grid made the numerical scheme very stable. In heat pipe transient operation, there are regions of high as well as low compressibility. Therefore, the governing equations are finite differenced on a staggered grid, shown in Fig. 2.3. The variables on this grid are not evaluated at the same point. By choosing control volumes which have the main grid points at their center, the velocity components are evaluated at the points that lie on the

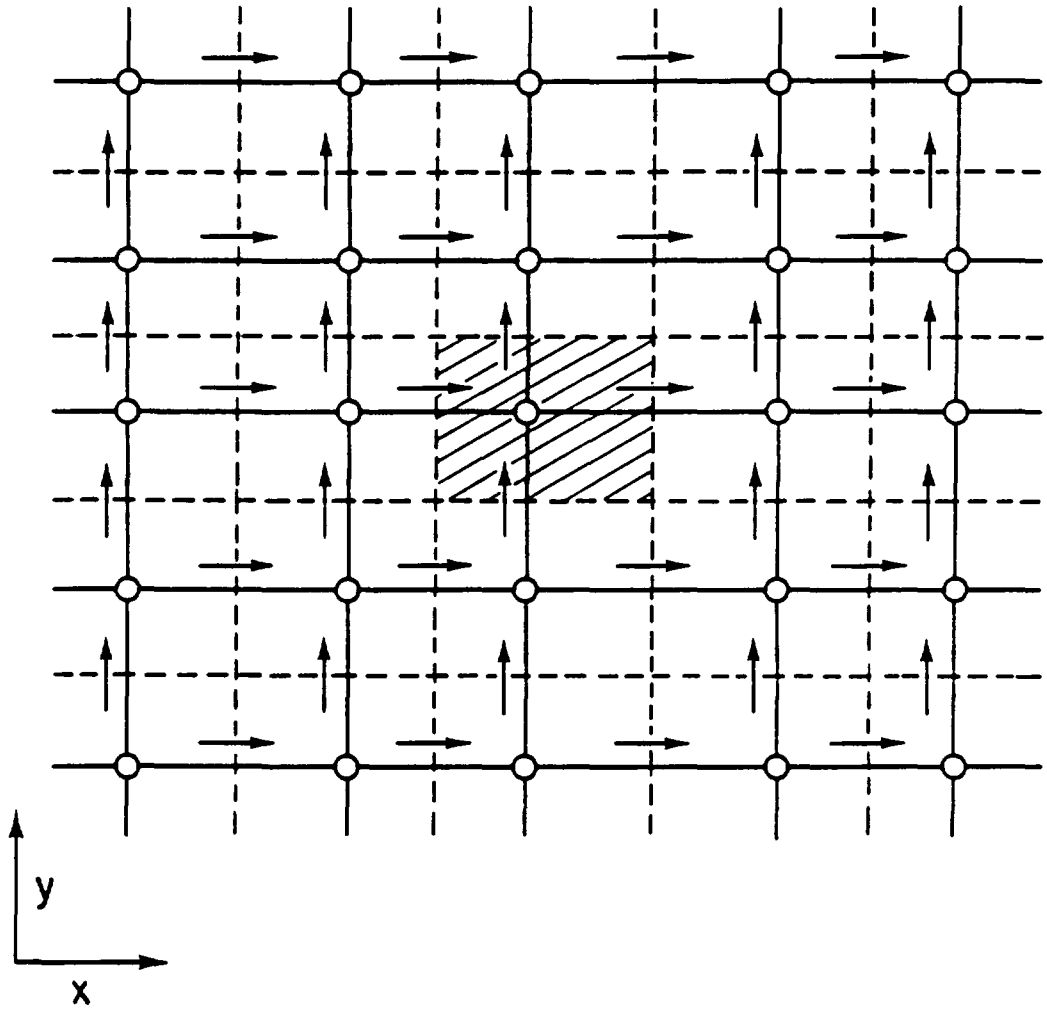

Fig. 2.3 Staggered grid

faces of the control volumes. The locations for u and v are shown by short arrows in the figure. The other dependent variables, namely, ρ, T and p, are calculated for the cell centers shown by small circles. The cell centers do not lie on the boundaries.

Several different methods are available to solve the governing equations. Among these, the SIMPLER scheme, introduced by Patankar [42], is the simplest one. In this method a control volume approach is employed on a staggered grid which makes the scheme very stable. The main advantageous point is that the pressure field is guessed and the momentum equations are solved for the velocity field. Then the continuity equation is used to correct the pressure for the next iteration. Therefore for the problems where pressure is not specified on the boundaries, this scheme is very useful. When the continuity equation is used for pressure correction, the density is assumed to be independent of pressure. This limits the scheme to be limited to incompressible flows and low compressible flows. In Chapter Three the algorithm of this method is discussed in detail. Application of the SIMPLER scheme in the operating transient mode of the heat pipe vapor dynamics, is also presented in Chapter Three. It will be shown that for relatively low input heat fluxes the compressibility of the vapor flow is low and the SIMPLER scheme results in some interesting calculations.

When the input heat flux is high or the process under a startup operation starts at a very low pressure and temperature, the vapor is highly compressible and a shock is created in the evaporator. Therefore, in the general analysis of heat pipes with a wide range of input heat flux, the standard methods, including the SIMPLER scheme, are not suitable. A nonlinear filtering technique,

along with the centered difference scheme, was used by Issacci et al. [43] for shock capturing as well as the cell-Reynolds-number problem. The basic principles of this filter and its application in a one-dimensional model of heat pipe vapor dynamics will be the subject of Chapter Four. It will be shown that the nonlinear filtering technique is quite simple to implement, is significantly more efficient than the standard methods, and is also found suitable for calculation of shock reflections. Then the full governing equations of the two-dimensional model will be solved using the nonlinear filtering technique. The results of these calculations are presented in Chapter Five for low- and high-input heat fluxes.

CHAPTER III
OPERATING TRANSIENT MODE OF HEAT PIPES

3.1 INTRODUCTION

In thermal systems in which a heat pipe is used as a device to conduct a large amount of heat in a short time, the question "How much, how fast?" is the main issue in designing such systems. The research performed so far on heat pipe transient behavior, is mainly concerned with the startup and shut down operations and the analyses are carried out mostly on a one-dimensional model.

In this chapter, the transient behavior of vapor flow is analyzed numerically using the two-dimensional model, described in Chapter Two. The main concern is the vapor core response to changes in the evaporation and condensation rates due to a sudden increase, or decrease, in the input heat flux, or the condensation temperature.

In operating transient operation, when a step change in the input heat flux is imposed on a steady-state operation at moderate pressure and temperature, the vapor compressibility is low. Under these conditions the SIMPLER method is quite efficient for analyzing vapor flow. An algorithm for this method and its application in heat pipe transients are described below. The results

of calculations for a water heat pipe following a sudden change in input heat flux are then presented.

3.2 THE SIMPLER METHOD

The governing equations, (2.11) to (2.15), derived in Chapter Two, are solved for ρ, ρu, ρv, T and p. The boundary conditions are given by Eqs. (2.17) to (2.22). The equations are finite differenced on a staggered grid shown in Fig. 2.3. The method used here is based on the SIMPLER method described by Patankar [42]. The time-dependent terms are discretized using the backward Euler method while the power law scheme was used for differencing the convective terms.

The calculational algorithm is as follows: The system pressure is assumed to be composed of two parts

$$p(x,y,t) = \bar{p}(t) + \tilde{p}(x,y,t) \tag{3.1}$$

where $\bar{p}(t)$ is the space averaged system pressure whereas $\tilde{p}(x,y,t)$ includes the space variation of the pressure. Assuming a pressure distribution, the momentum equations (Eqs. (2.12) and (2.13)) are solved for the velocity components u and v at a time step. Then using the continuity equation and density ρ from the last iteration on temperature, the pressure is corrected to be used again in the momentum equations. Upon accomplishing these iterations, the velocity field and $\tilde{p}(x,y,t)$ will be found.

Using the velocity field, the energy equation (Eq. (2.14)) is then solved for temperature. In order to calculate the density from the equation of state, and to evaluate the boundary conditions, we need the absolute value of the pressure. Global mass balance is used to calculate the absolute pressure. The total mass, for an ideal gas, m, is related to the pressure by

$$m = \int_V \rho dV = \int_V \frac{p}{RT} dV \tag{3.2}$$

where V is the volume. The increase in the total mass in one time step is

$$m(t+\Delta t) - m(t) = (\dot{m}_{in} - \dot{m}_{out})\Delta t \tag{3.3}$$

where $\dot{m}_{in}$ and $\dot{m}_{out}$ are the input and output mass fluxes, respectively, and are calculated from the boundary conditions. Equations (3.2) and (3.3) are combined to yield

$$(\dot{m}_{in} - \dot{m}_{out})\Delta t = \int_V \left(\frac{p|_{t+\Delta t}}{RT|_{t+\Delta t}} - \frac{p|_t}{RT|_t} \right) dV \tag{3.4}$$

Thus Eq. (3.4) is used to evaluate the absolute pressure of the system. For a real gas, using an equation of state, the above procedure is followed to calculate the total pressure.

3.3 RESULTS

The computational procedure described above was implemented in a two dimensional time-dependent compressible flow with the same type of heat pipe boundary conditions mentioned above. The computations were performed for several evaporator heat fluxes for water as a working fluid. The pipe dimensions used in the calculations were $b = 2.5\ cm$ and $L = 3b$ and the computational grid spacings were $\Delta x = 0.1$ and $\Delta y = 0.05$. The temperature and pressure variations, and consequently, the density variation, were found to be quite small inside the pipe. This is expected of systems in which condensation takes place without a non-condensible gas.

The steady state results are shown in Figs. 3.1, 3.2 and 3.3. The steady state was assumed to be reached when the relative change of all variables in one time step was less than 0.5%. Figures 3.1 show the axial velocity profiles at different axial cross sections along the pipe, for low-input heat flux, Fig. 3.1(a), and for high-input heat flux, Fig. 3.1(b). The flow stream lines for these two cases are shown schematically in Fig. 3.2.

When the input heat flux is relatively low (Re=1.0), the evaporation rate is low and the vapor flows smoothly towards the condensation region (Figs. 3.1(a) and 3.2(a)). However, with high input heat flux (Re=1000) the evaporation rate is high, the vapor is ejected with a high momentum from the evaporator and under steady state conditions, condenses at a high rate at the condenser.

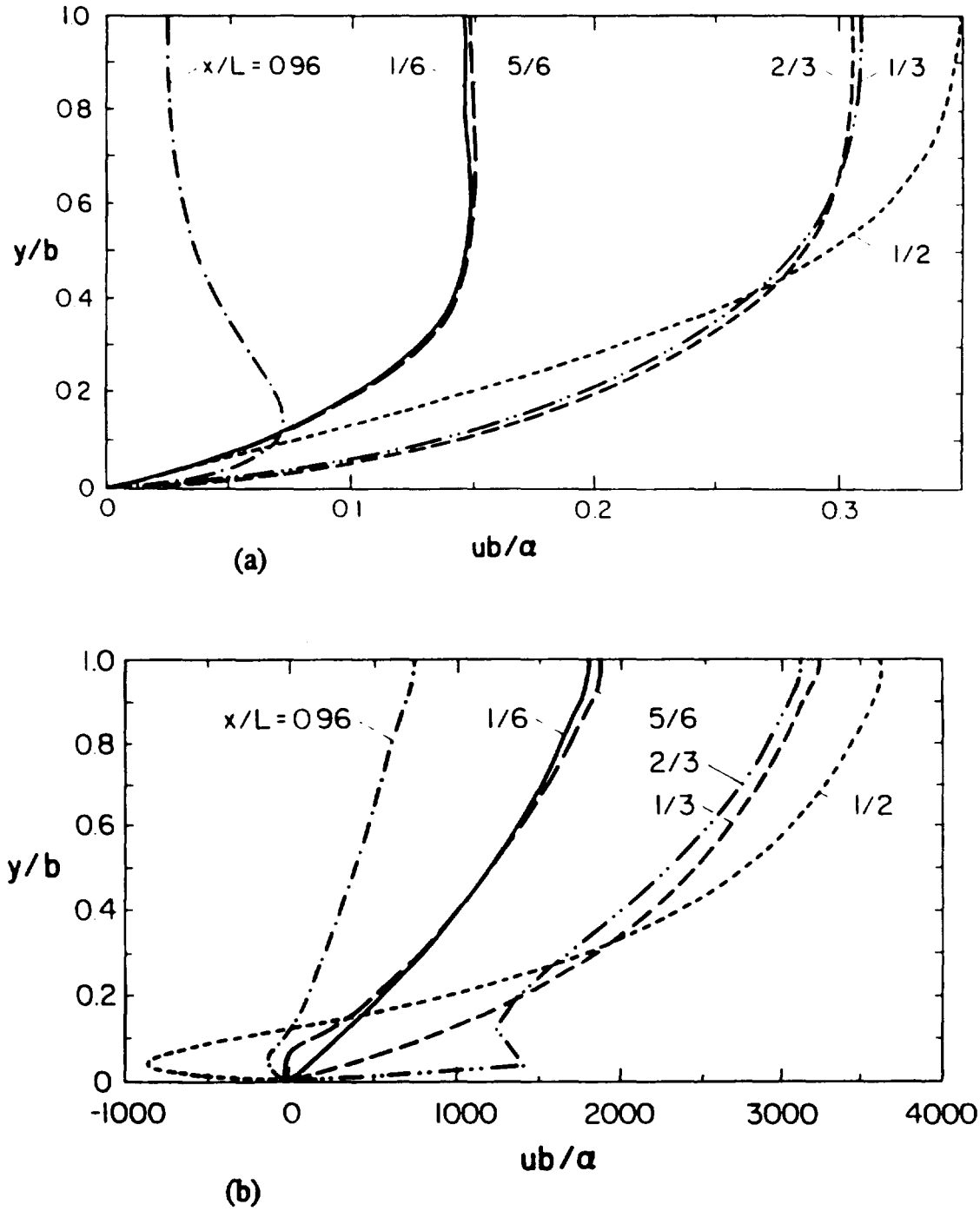

Fig. 3.1 Axial velocity profile. (a) Low-input heat flux (Re=1), (b) high-input heat flux (Re=1000)

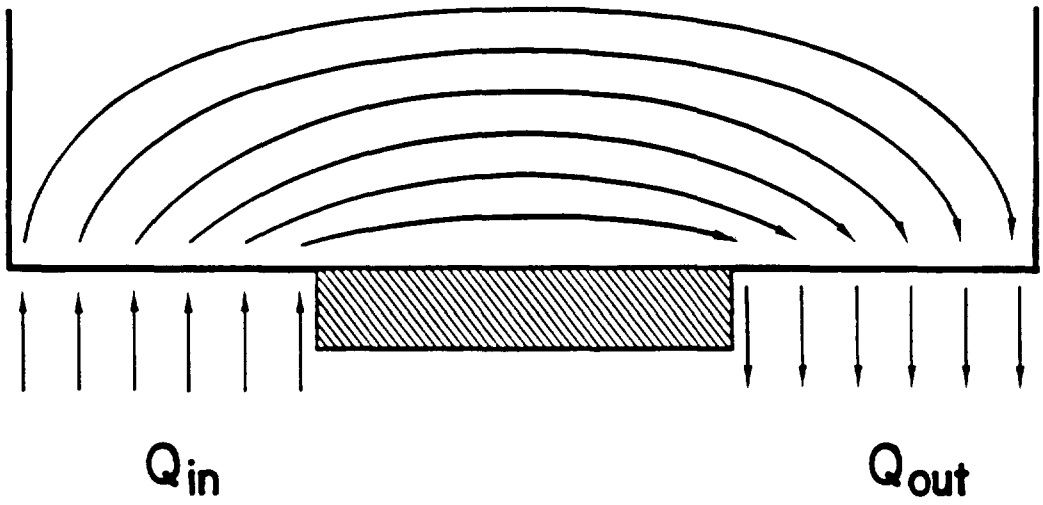

(a)

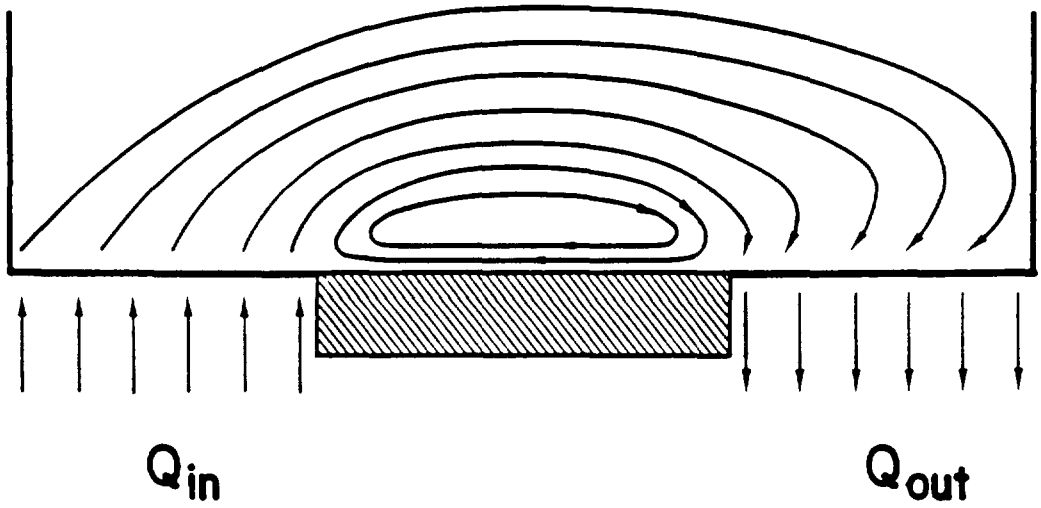

(b)

Fig. 3.2 Vapor flow pattern. (a) Low-input heat flux, (b) high-input heat flux

The high momentum flow at the two ends of the adiabatic section results in circulation flow in this region. That is, on the adiabatic surface there is a reverse flow. In addition, in the condensation region the high momentum vapor flow impacts the rigid end wall, returns and then condenses in the liquid region. This return flow is shown in Figs. 3.1(b) and 3.2(b). The vertical velocity profiles for different vertical cross sections are shown in Fig 3.3. The flow is clearly two dimensional.

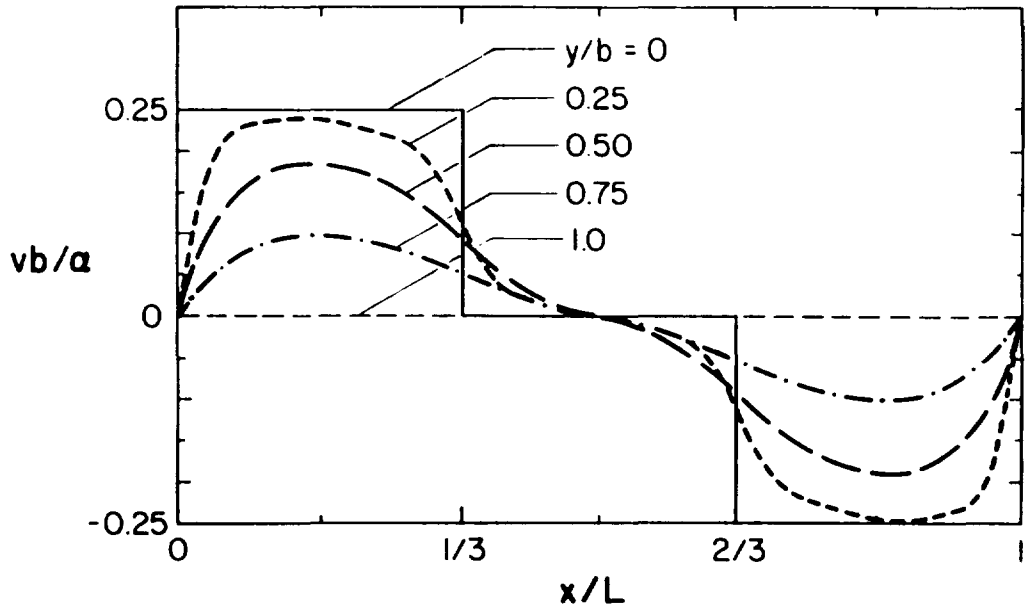

Fig. 3.3 Vertical velocity profiles

It is worth noting that Galaktionov and Trukhanova [21] observed reverse flow in the gas-controlled heat pipe. To obtain the high heat flux solution, we used an incremental procedure where the magnitude of the input heat flux was increased and previous solutions were used as initial guesses for higher heat fluxes. It has been shown by Serrin [44] that the Navier-Stokes equations have a unique solution if they are considered as an initial value problem. Therefore, reverse flow is both unique and a valid solution for a high input heat flux.

Transient behavior of vapor flow was studied by using a steady-state solution as the initial conditions for different input parameters. As an example, Fig. 3.4 shows the axial velocity profiles at the middle of the pipe, at different time steps. Curve 0- on this Figure is the steady state solution for $Re = 100$ where Reynolds number is defined as

$$Re = \frac{\dot{m}_{in} b}{\mu} \tag{3.5}$$

and $\dot{m}_{in}$ is the input mass flux. Curves 1 to 4 show this velocity profile at different time steps after a sudden increase in input heat flux for $Re = 200$. At the outset, the increase in input heat flux overcomes the reverse flow, see curve 1. As the velocity profile develops with time, the steady state profile, curve 4, shows a higher reverse flow at the liquid-vapor interface.

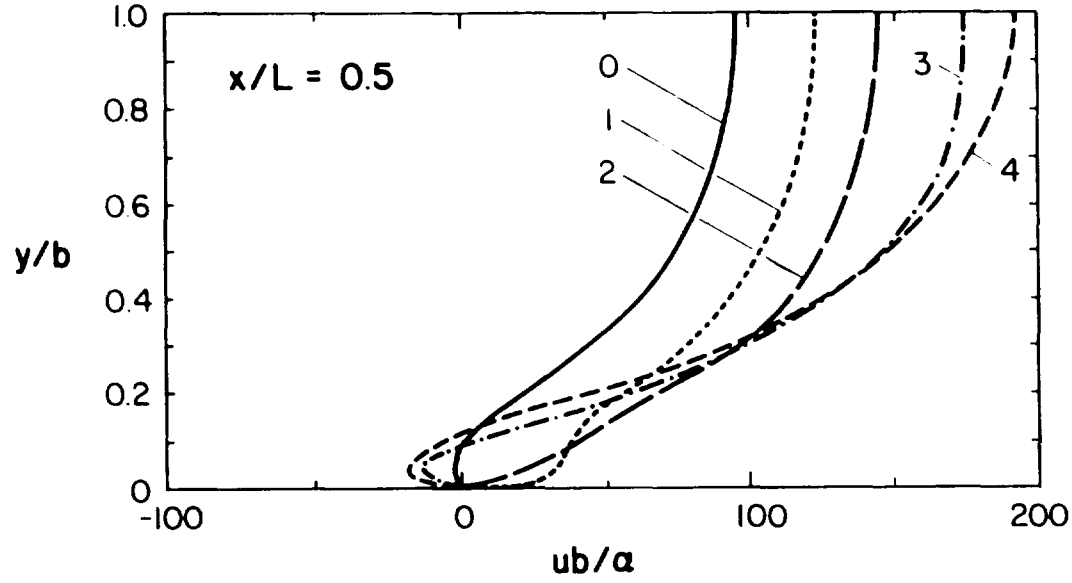

Fig. 3.4. Axial velocity profile at different time steps. 0- initial profile (τ=0), 1- $\tau=10^{-4}$, 2- $\tau=2.5\text{x}10^{-3}$, 3- $\tau=10^{-2}$, 4- steady state ($\tau=2.5\text{x}10^{-2}$) where $\tau=t\alpha/b^2$.

3.4 CONCLUSIONS

The dynamic behavior of vapor flow in heat pipes was studied in this chapter for transient operations. Although the solution is presented for Cartesian coordinates, the computational code can be easily modified for circular heat pipes. Interesting phenomena have been observed in the adiabatic and condensation regions. in these sections high input heat flux causes flow reversal. This can result in negative shear forces on the wick structure.

Further, in transient operations the shear force at one location may change sign. Detailed information on the magnitude and direction of the shear force is needed for design purposes, and this needs a proper two-dimensional analysis.

Chapter IV
NONLINEAR FILTERING TECHNIQUE

4.1 INTRODUCTION

Shock capturing and treatment of cell-Reynolds-number problems are among the major challenges in numerical approximations of nonlinear equations associated with fluid flow and heat and mass transfer. The earlier schemes proposed for shock computation, based on centered differencing, typically use artificial dissipation to control oscillations in the shock neighborhood. The only complete remedy is the use of monotone schemes, such as that by Godunov [45], which are only first order. The recent methods for shock capturing, using field-by-field decomposition and flux limiting (e.g., Harten [46] or Chakravarthy and Osher [47]), are able to capture a sharp discontinuity without oscillations. However, these methods are quite complicated and not efficient numerically. Filters have also been used in shock capturing [48], however a major problem is low accuracy and smearing of the shock front. Recently, Engquist, Lötstedt and Sjögreen [49] proposed a nonlinear filter to accurately capture a shock without oscillations. The algorithms for this filtering

technique are quite simple to implement, and they are significantly more efficient than earlier methods with comparable ability.

The cell-Reynolds-number (or cell-Peclet-number) problem refers to a class of fluid dynamic problems with large-grid Reynolds number. Discretization of advective terms in these cases plays a significant role. The centered-difference scheme (CDS) is ill-behaved for grid Reynolds numbers larger than two because the coefficients of the difference equation are not necessarily positive, consequently, diagonal dominance of the corresponding system matrix may be lost. As a result, solutions to the difference equations may not be unique and may result in nonphysical spatial oscillations. Several different methods have been proposed to modify the CDS to guarantee positivity of coefficients. Probably the most popular of these schemes are the upwinding [50], hybrid [51], and power law [52]. These methods are well-behaved, but they cause high numerical diffusion. Recently, Runchal [53] proposed the CONDIF method which is designed to yield positive coefficients and, at the same time, retain the second-order accuracy of CDS. Although it was developed specifically to treat the cell-Reynolds-number problem in incompressible flows, there have recently been conjectures regarding its applicability to compressible flows with shocks, particularly its possible total variation diminishing (TVD) properties. In the sample problem examined below, it will be shown that this method is stable but that it is not TVD. Thus, it is not generally suitable for shock capturing.

In this model problem, a nonlinear filter, based on a concept introduced by Engquist et al. [49], is used to study the dynamics of compressible vapor flow. The cell-Reynolds-number problem is involved as are shock capturing and shock reflections for intermediate and high Reynolds numbers. Other schemes (upwinding, power law, and CONDIF) will also be used to solve the problem, showing the numerical diffusion resulting from the use of these methods.

4.2 SAMPLE PROBLEM

The dynamics of compressible vapor flow are studied as a model problem. The vapor is assumed to be initially stagnant. A sudden increase in the input mass flux is imposed at a higher temperature. An example of this problem is the vapor flow dynamics of heat pipes, Fig. 4.1, in the transient mode. The governing equations are the usual continuity, momentum, and energy equations of compressible fluid flow. An equation of state relates the pressure to the temperature and density. These equations in normalized, one-dimensional (1-D) form are

$$\frac{\partial \rho}{\partial t} + \frac{\partial \rho u}{\partial x} = 0 , \tag{4.1}$$

$$\frac{\partial \rho u}{\partial t} + \frac{\partial \rho u u}{\partial x} = -\frac{\partial p}{\partial x} + \frac{\partial}{\partial x}\left(\frac{1}{Re}\frac{\partial u}{\partial x}\right), \tag{4.2}$$

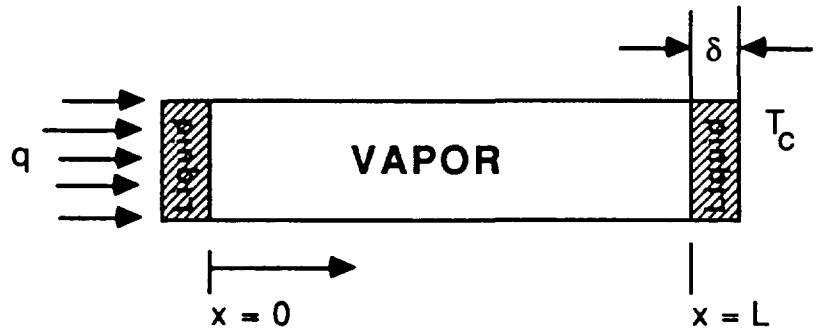

Fig. 4.1. One-dimensional vapor core model of a heat pipe

$$\frac{\partial \rho T}{\partial t} + \frac{\partial \rho u T}{\partial x} = \frac{\partial}{\partial x}\left(\frac{1}{RePr}\frac{\partial T}{\partial x}\right), \tag{4.3}$$

$$p = \rho T , \tag{4.4}$$

and are solved on the domain $(x,t) \in (0,1)$ x $(0,t_f)$. In these equations, ρ is density, u is velocity, T is temperature, and p is pressure in nondimensional form. The nondimensional parameters are Reynolds number, Re, and Prandtl number, Pr, defined as

$$Re = \frac{\rho u D}{\mu}, \qquad Pr = \frac{\mu C_p}{k}, \tag{4.5}$$

where μ is dynamic viscosity, k is thermal conductivity, C_p is specific heat, and D is the pipe diameter.

The initial and boundary conditions are

$$\rho(x, 0) = 1,$$

$$\rho u(x, 0) = 0, \tag{4.6}$$

$$T(x, 0) = T0(x),$$

and

$$\rho(0, t) = \rho_e ,$$

$$\rho u(0, t) = 1, \tag{4.7}$$

$$T(0,t) = T_e ,$$

where ρ_e and T_e are, respectively, the density and temperature of the vapor at the evaporator of the heat pipe.

4.3 NUMERICAL SOLUTION

The governing Eqs. (4.1)-(4.3) are solved for ρ, ρu, and T, respectively, with p recovered from the equation of state [Eq. (4.4)]. For the sake of analysis, the nonlinear partial-differential equations are cast in the general form

$$\frac{\partial \Phi}{\partial t} + \frac{\partial}{\partial x}\left(u\Phi - \Gamma \frac{\partial \Phi/\rho}{\partial x}\right) = S \,. \tag{4.8}$$

This equation is discretized on the staggered grid shown in Fig. 4.2. The temperature, density, and pressure are calculated at points indexed by i, and the mass flux, ρu, is calculated at points indexed by ℓ, where $\ell = i + 1/2$.

Using the backward Euler algorithm for time differencing and centered differences in space, Eq. (4.8) is approximated by

$$- a_{1,i}\Phi_{i-\ell} + a_{2,i}\Phi_i - a_{3,i}\Phi_{i+\ell} = b_i \,, \tag{4.9}$$

where

$$\begin{aligned} a_{1,i} &= D_{\ell-1}\,(1 + \frac{1}{2}\ Pe_{\ell-1}) \,, \\ a_{3,i} &= D_{\ell}\,(1 - \frac{1}{2}\ Pe_{\ell}) \,, \\ a_{2,i} &= a_{1,i} + a_{3,i} + (u_\ell - u_{\ell-1}) + \frac{\Delta x}{\Delta t} \\ b_i &= \Delta x\, S_i + \frac{\Delta x}{\Delta t}\,\Phi_i^n \end{aligned} \tag{4.10}$$

with

$$D_{\ell-1} = \frac{\Gamma_{\ell-1}}{\rho_{i-1}\Delta x} \,, \quad D_1 = \frac{\Gamma_\ell}{\rho_{i+1}\Delta x} \,, \quad Pe_\ell = \frac{u_\ell}{D_\ell} \,, \tag{4.11}$$

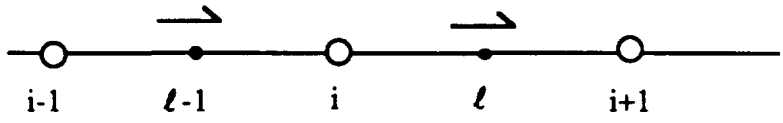

Fig. 4.2. The staggered grid and nodes

For stability and a unique solution, the coefficients of Eq. (4.9) should be positive. If the grid Peclet number, Pe_ℓ, is greater than two in magnitude, some of the coefficients defined by Eq. (4.10) are not positive.

4.3.1 *Standard Schemes*

The coefficients of Eq. (4.9) are written in a general form as

$$a_{1,i} = D_{\ell-1} A(Pe_{\ell-1}) + \max(0, u_{\ell-1}) ,$$

$$a_{3,i} = D_{\ell} A(Pe_{\ell}) + \max(0, -u_{\ell}) ,$$

$$a_{2,i} = a_{1,i} + a_{3,i} + (u_{\ell} - u_{\ell-1}) + \frac{\Delta x}{\Delta t} . \qquad (4.12)$$

Expressions for $A(Pe)$ for different schemes are listed in Table 4.I. Derivation of $A(Pe)$ for upwinding and power-law schemes can be

TABLE 4.I

The Function $A(Pe)$ for Different Schemes

Scheme	$A\,(Pe)$
CDS	$1 - 0.5\,\lvert Pe\rvert$
Upwinding	1
Power law	$\max[0,(1 - 0.1\,\lvert Pe\rvert)^5]$
CONDIF	$A\,(Pe_{\ell-1}) = 1 - \max(0,Pe_{\ell-1}/2) + R\,\max(0,Pe_{\ell}/2)$ $A\,(Pe_{\ell}) = 1 - \max(0,-Pe_{\ell}/2) + \frac{1}{R}\max(0,Pe_{\ell-1}/2)$

found in Patankar [42] and for the CONDIF scheme in Runchal [53]. The parameter R appearing in Table I for the CONDIF scheme is defined as

$$R = \frac{\Phi_{i+1} - \Phi_i}{\Phi_i - \Phi_{i-1}} \quad . \tag{4.13}$$

If there is a sharp variation in Φ then R may be quite large and, conversely, if there is only a small variation in Φ, R will be small. Therefore, a limit is imposed on R so that

$$1/R_{max} \leq R \leq R_{max} \quad . \tag{4.14}$$

It can be seen, using the appropriate formulas from Table I, that R_{max} controls the amount of numerical diffusion in the scheme. In particular, large values of R result in significant numerical diffusion while small values cause little diffusion. Typical values are in the range $4 \leq R_{max} \leq 10$.

4.3.2 *Filtering*

Engquist, et al. [49] introduced nonlinear filters for shock computation. These filters are used as post-processors in conjunction with standard finite-difference schemes. The difference equations are solved at every time level; then the solutions are processed with the filter to eliminate oscillations. The filters control the total variation (i.e., they possess the TVD property), produce sharp shocks (they are second order away from shocks), and they are simple to use.

For the calculations, we use CDS and a nonlinear filter, as described below (for details, see Ref. [49]). The results are compared with those from the widely used upwinding, power-law, and CONDIF schemes. The filter produces more accurate results with no significant increase in the computation time for problems

either experiencing cell-Reynolds-number difficulties or having shock-like solutions.

The principles of the filtering technique are illustrated below using Fig. 4.3. Figure 4.3(a) shows the solution Φ^n at time t^n. Using CDS, the typical solution at time t^{n+1}, φ^{n+1}, is shown in Fig. 4.3(b). This solution exhibits an overshoot, as would be expected. Results of filtering are displayed in Fig. 4.3(c) where it can be seen that the overshoot has been completely removed. The principles of the filtering process are the following:

(i) $\varphi_{i_o}^{n+1}$ is detected as an overshoot via the test

$$[(\Delta_- \varphi_{i_o}^{n+1})(\Delta_+ \varphi_{i_o}^{n+1})] < 0 ,$$

(ii) $\varphi_{i_o}^{n+1}$ is decreased,

(iii) The new value of $\varphi_{i_o}^{n+1}$ should not be less than the value of $\varphi_{i_o-1}^{n+1}$,

(iv) $\varphi_{i_o+1}^{n+1}$ is increased by the same amount as $\varphi_{i_o}^{n+1}$ is decreased in order to maintain conservation properties, and thus to obtain the right shock speed.

The symbols Δ_- and Δ_+ denote the backward and forward differences, respectively, and are defined as $\Delta_\pm \Phi_i = \pm (\Phi_{i\pm1} - \Phi_i)$.

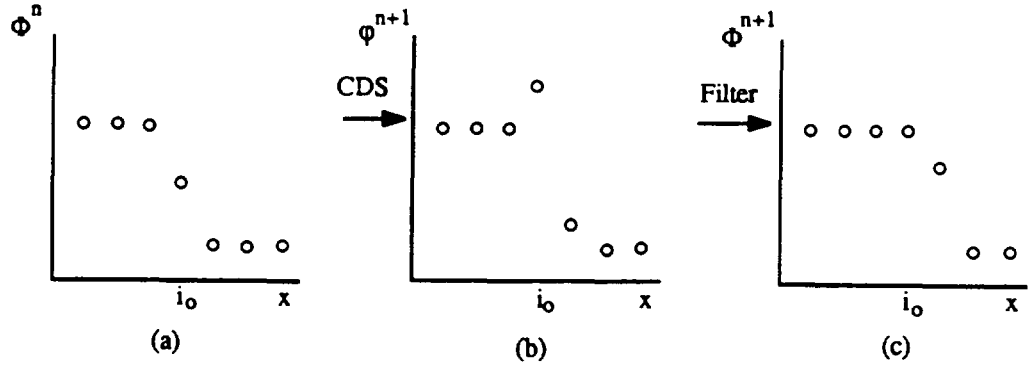

Fig. 4.3. Filtering process applied to the CDS result

The algorithm for this filtering and also for more complicated ones, can be found in Ref. [49], in which the nonlinearity and TVD properties of the filtering technique have been shown.

4.4 RESULTS AND DISCUSSION

The sample problem described above has been solved numerically using different schemes (centered differencing, first-order-upwinding, power-law, and CONDIF in conjunction with the nonlinear filter). Calculations have been carried out for high Reynolds number (Re = 10,000) to study the shock capturing ability of different schemes and also for low Reynolds number (Re = 20) to examine the cell-Reynolds-number problem. The calculations were performed on the Cray-2 supercomputer at the Lawrence Livermore National Laboratory.

In heat-pipe vapor-dynamics applications, the shock wave created in the evaporator travels towards the condensation region, where an outflow (smaller than the inflow at the evaporator) leaves the system, and the shock reflects back toward the evaporator. In this section, the reflection of a shock wave on a wall with zero permeability and with partial permeability has also been studied.

4.4.1 *Shock Capturing*

Figures 4.4 through 4.6 present the results for Re = 10,000. At this high Reynolds number, the diffusive terms are negligibly small, and the flow propagates mainly by convection. Figure 4.4 compares the shock capturing ability of different schemes at two different times (t = 0.2 and 0.75). These calculations were performed with the number of grid points, N = 41. Here, it is shown that the nonlinear filter leads to a sharp shock front, whereas the other schemes cause an overshoot and smearing of the front. The power-law-scheme results are basically the same results as those of upwinding for this case. This is due to the large-grid Peclet number. For the normalized velocity, length, and time, the shock front at t = 0.2 and t = 0.75 should be at x = 0.2 and 0.75, respectively. Although at early times all schemes calculate the shock at the right position, at later times (t = 0.75) only filtering captures the shock front at the correct location. Comparing CONDIF and upwinding, it seems that the CONDIF scheme produces

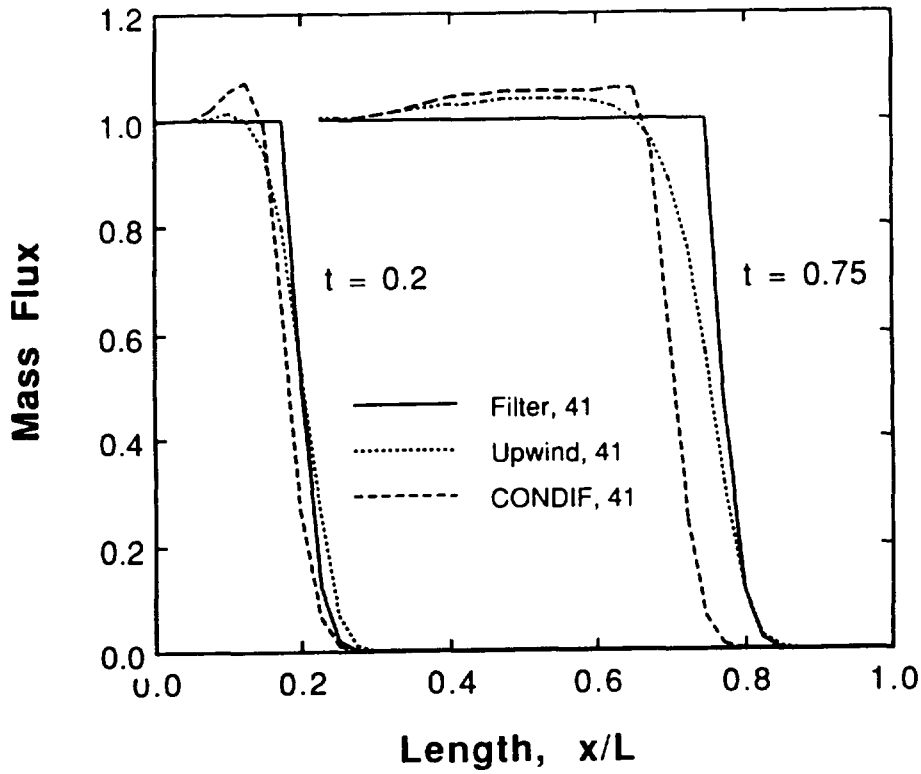

Fig. 4.4 Mass flux profile at different times for different schemes

a sharper front, but it causes more overshoot and does not catch the shock at the right position.

In order to show how accurately the filtering captures the shock, calculations have been carried out for coarse and fine meshes. Figure 4.5 shows these results for the number of grid points N = 21, 41, and 81 at early (t = 0.2) and later (t = 0.75) times. It is shown that the shock is captured within only two grid

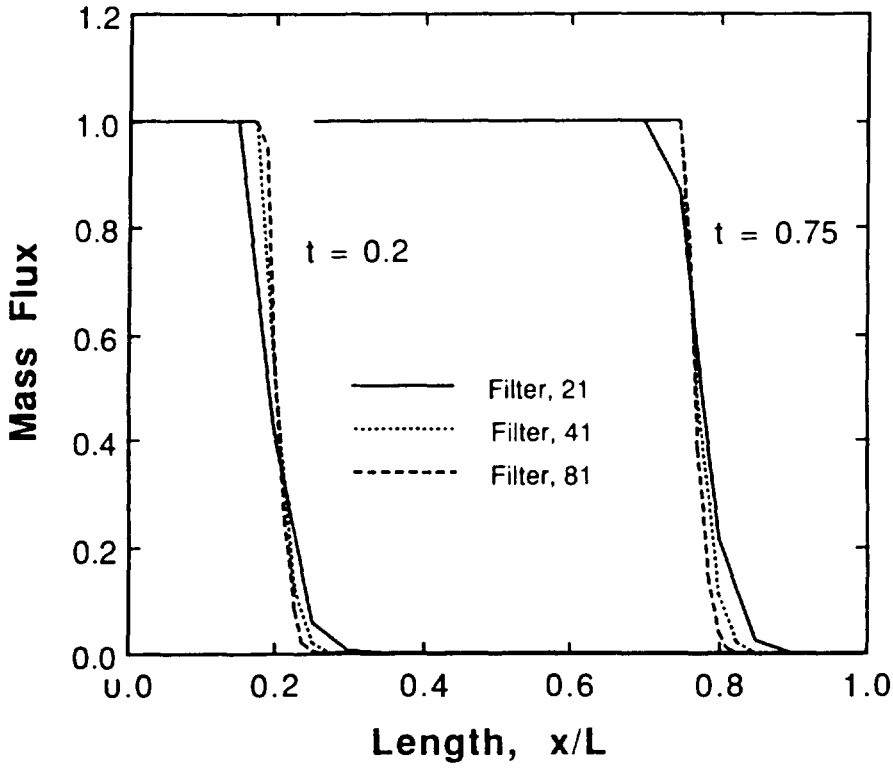

Fig. 4.5 Mass flux profile at different times for different number of nodes

spacings regardless of the number of grid points. Therefore, the shock-front width decreases significantly with a finer mesh.

The total variation of the solution function, Φ, should not increase with time for a shock-capturing scheme with no oscillations or overshoot. The total variation at any time is defined by

$$TV(\Phi^n) = \sum_{i=1}^{N-1} \left| \phi_{i+1}^n - \phi_i^n \right| \tag{4.15}$$

Then, the TVD property is expressed as

$$TV(\Phi^{n+1}) \leq TV(\Phi^n) \tag{4.16}$$

This criterion has been checked for the different schemes used in this study. Figure 4.6 shows that filtering possesses the TVD properties, whereas the upwinding and CONDIF methods do not exhibit TVD behavior.

4.4.2 *Cell-Reynolds-Number Problem*

Nonlinear filtering has also been compared with several other schemes for treating the cell-Reynolds-number problem. In this case the Reynolds number is relatively low, and the diffusion term is no longer negligible. However, for a coarse mesh, the grid Reynolds number may be greater than two, which causes oscillations. For Re = 20, the sample problem was solved for the mass flux, ρu, on a fine mesh (N = 81) using CDS. The CDS solution is compared with those of other schemes on a coarse mesh, N = 9, in Fig. 4.7 where it is seen that the CDS solution has an overshoot. Normally, when the cell-Reynolds-number is a problem, the CDS causes oscillations. However, as a result of the high compressibility of the flow in the sample problem, the pressure term in the momentum equation is of the same order as the other terms,

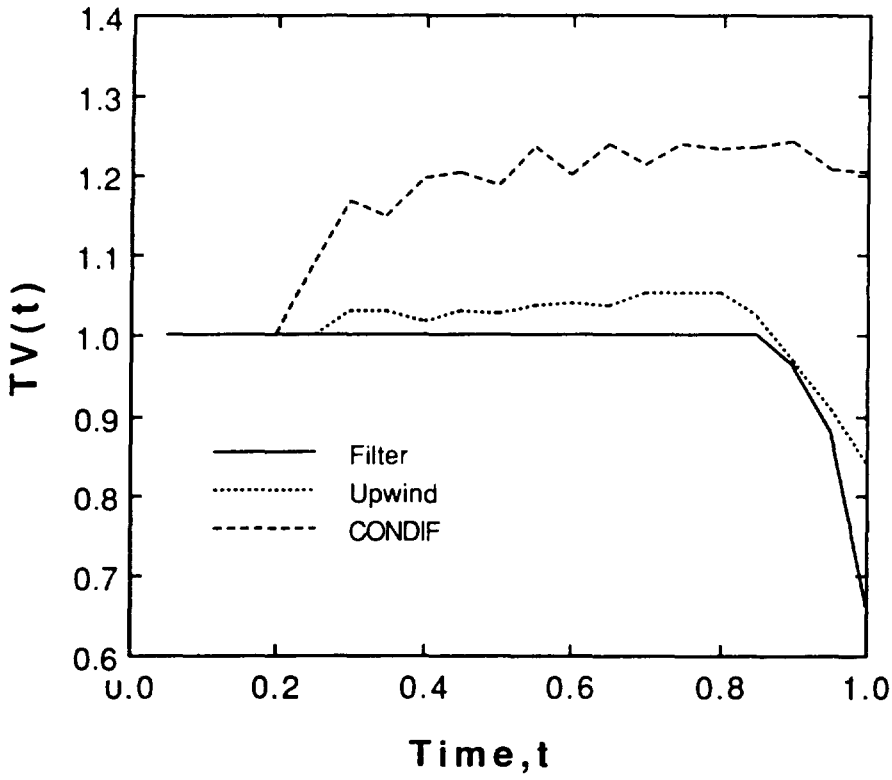

Fig. 4.6 Total variations of the mass flux for different schemes

causing an overshoot due to forcing rather than oscillations. Although all of the schemes tested eliminate the overshoot, the filtering scheme produces the most accurate solution. To show the discrepancy from the "exact solution," the CDS solution on the fine mesh is taken as the reference solution, Φ_r, and the L^2-norm of the error has been calculated as

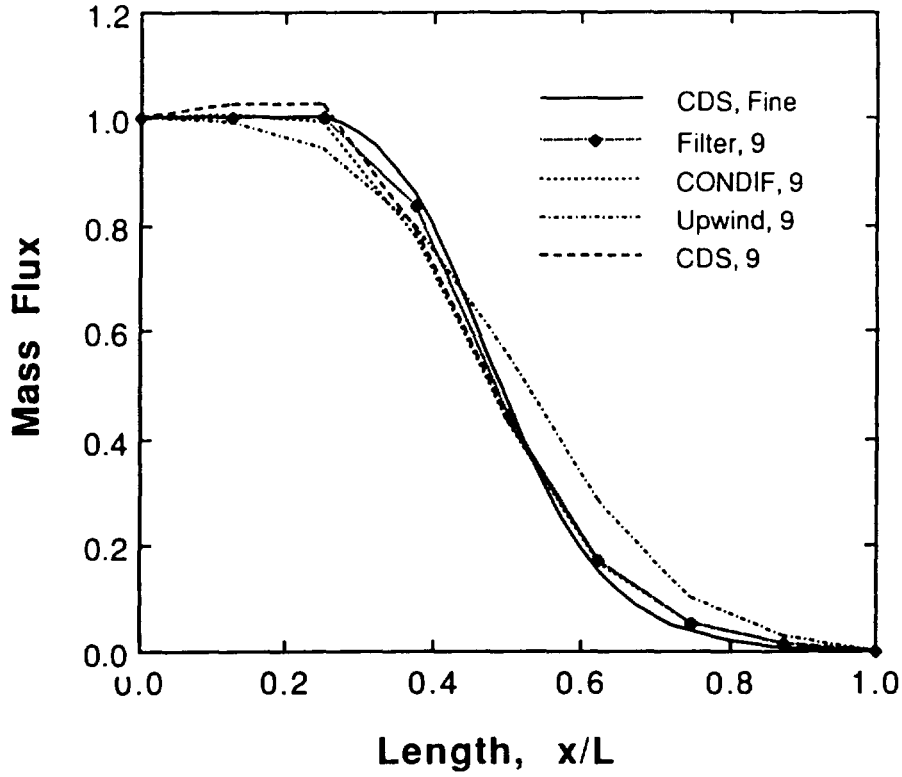

Fig. 4.7 Mass flux profiles for low Reynolds number for different schemes

$$L^2\text{-}norm = \left(\frac{1}{N} \sum_i \left| \phi_{r_i} - \phi_i \right|^2 \right)^{1/2} . \qquad (17)$$

Table 4.II shows the L^2-errors for ρu calculated at t = 0.5 for the various schemes considered. As can be seen, use of the nonlinear filter results in a significantly smaller L^2-error than any of the other methods.

TABLE 4.II

L^2-Error for Different Schemes

	L^2-norm
CDS	8.98×10^{-2}
Upwinding	6.37×10^{-2}
Power law	5.14×10^{-2}
CONDIF	3.06×10^{-2}
Filtering	1.49×10^{-2}

4.4.3 *Shock Reflection*

In this section we examine the use of nonlinear filtering in simulating reflected shocks on a partially blocked wall at $x = L$. When a shock reflects off a wall, the pressure on the wall increases to twice the value behind the shock [54]. This was verified in the computations by solving the equations for high Reynolds number, $Re = 10^4$, with the boundary condition $\rho u\ (x = L) = 0$. In order to explore the shock reflection on a partially blocked end, the governing equations were first solved for low Reynolds number, $Re = 10$. In this case, the number of grid points was $N = 21$, and no filtering was needed. The physical process is initiated by a sudden inflow at $x = 0$. The mass flux profile has the same shape as

that shown in Fig. 4.7, and the corresponding wave front propagates along the x-direction with time. When it reaches $x = L$, where only a fraction of the flow is extracted, the vapor is compressed and the pressure increases. This will cause a positive pressure gradient along x, and the front reverses direction. The mass flux profiles along x at different times are shown in Fig. 4.8. When the flow front reaches $x = 0$, the vapor is compressed all along x, and the inflow at $x = 0$ will cause the flow propagation towards the end $x = L$. When the flow front reaches the pipe's end for the second time, the increase in pressure causes more outflow, and flow reflection takes place. The process of refill and reflection of mass flux continues, and the outflow increases with each reflection until the outflow is as high as the inflow. At this time the process reaches a steady-state condition (Fig. 4.8.)

The same vapor-flow transient behavior is found at higher Reynolds number. Figure 4.9 depicts the mass flow profiles at different times for $Re = 1000$. In this case, the number of grid points is $N = 41$, and the calculated mass flow is filtered in two steps (i.e., forward and backward) at each time step. In the forward step, the filtering process (Section 4.3.2) is used from $x = 0$ to the x-location of the shock front to eliminate the nonphysical oscillations. In the backward step, the mass flow profile is filtered from $x = L$ backward to the shock front. Referring to Figs. 4.8 and 4.9, the transient process reaches a steady-state condition after approximately five sets of refill and

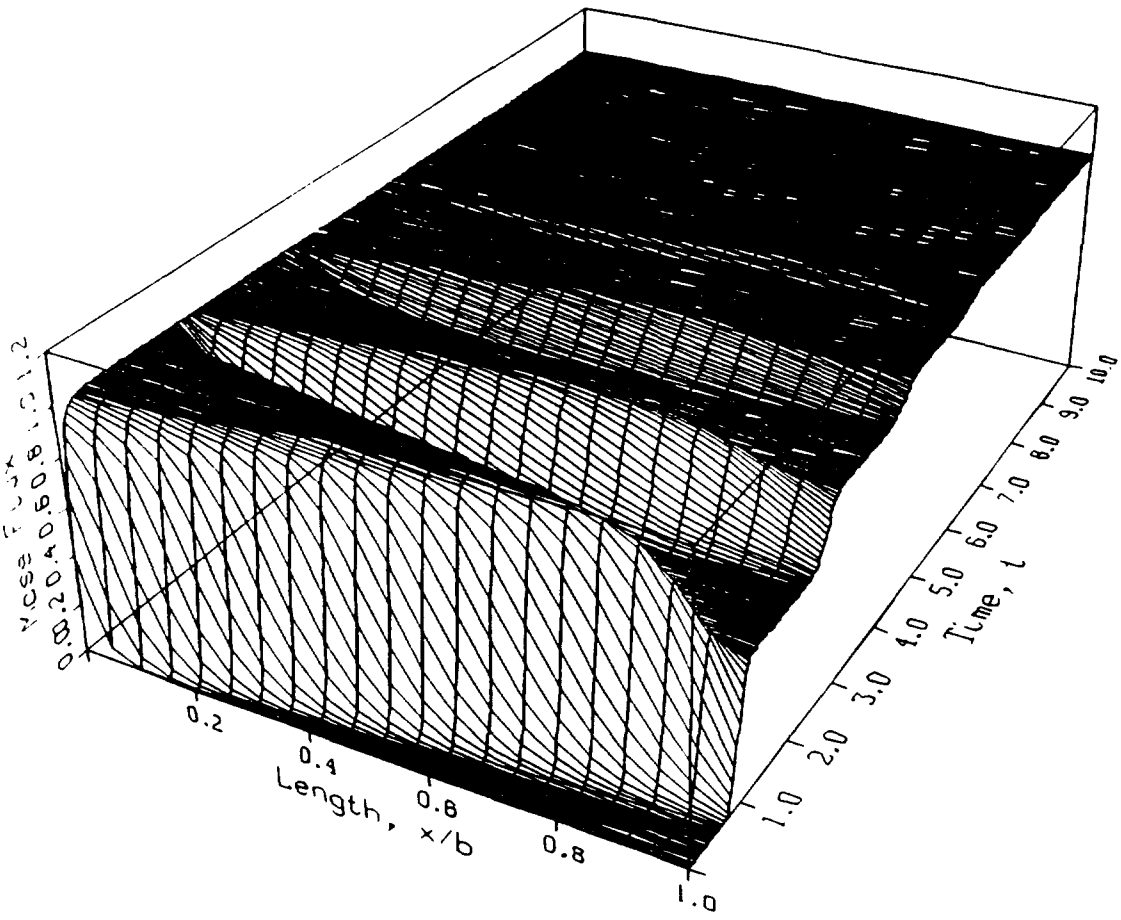

Fig. 4.8 Shock reflections at low Reynolds number, Re = 10

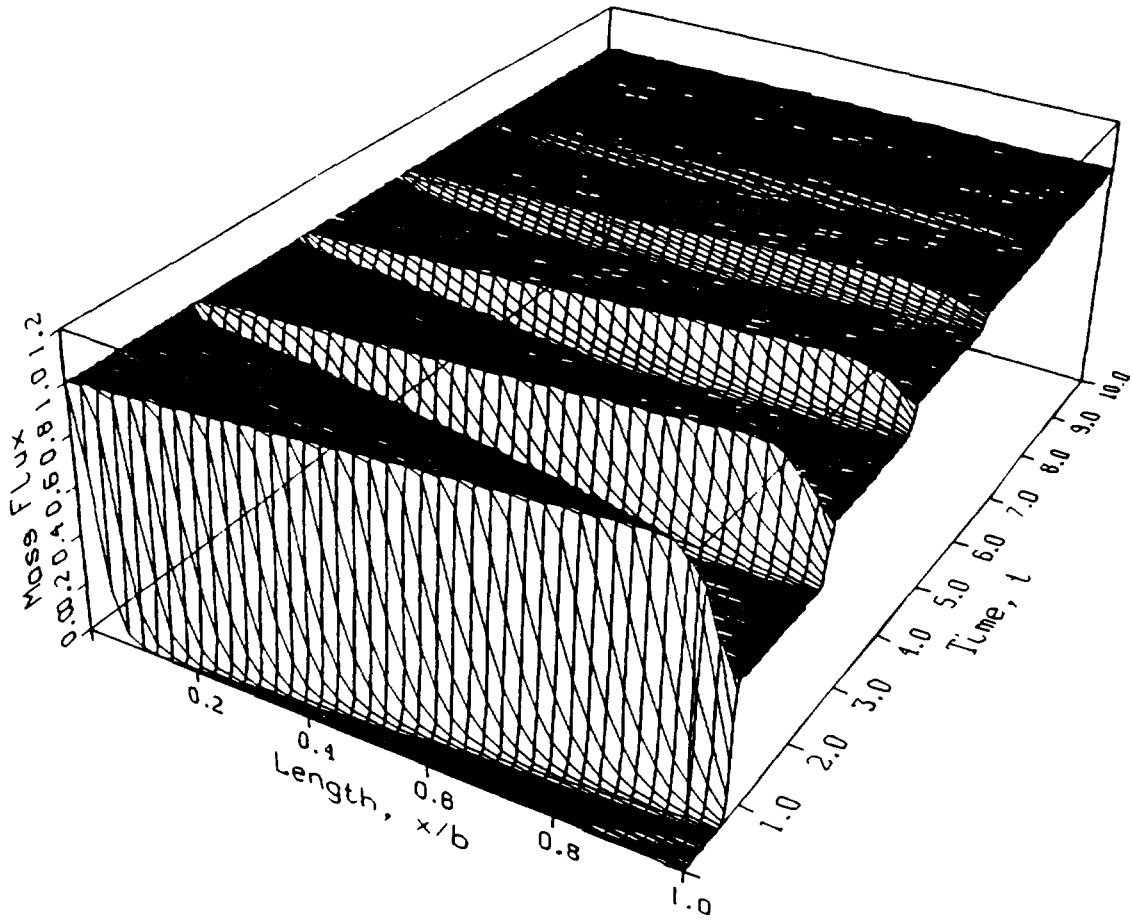

Fig. 4.9 Shock reflections at high Reynolds number, Re = 1000

reflection of flow front, nearly independent of the input mass flux (or Reynolds number).

4.5 CONCLUDING REMARKS

The use of a nonlinear filter has been examined in the context of the dynamics of compressible vapor flow. The filter was used with both low and high Reynolds numbers to examine the cell-Reynolds-number problem as well as the shock-capturing ability of the technique. The resulting solutions were compared with those obtained by using standard schemes like upwinding, power-law, and CONDIF. The filtering was found to be quite simple to use, and is significantly more efficient than earlier methods with comparable ability.

For low Reynolds numbers and a coarse grid (cell-Reynolds-number problem), the centered difference scheme produces an overshoot. Although all of the standard schemes mentioned above eliminate the overshoot, filtering produces the most accurate solution. Among these methods, upwinding produces the highest numerical diffusion, and the CONDIF method produces a more accurate solution than the upwinding and the power-law schemes.

For high Reynolds numbers, the filtering technique is able to capture the shock in only two or three grid spacings regardless of the number of the grid points, whereas the other schemes cause an overshoot and smearing of the shock front. Comparing CONDIF and

upwinding, the former produces a sharper shock front, but it causes more overshoot and the predicted wave speed is less accurate.

Nonlinear filtering was also found suitable for calculation of shock reflections. This aspect of the filtering procedure has not been tested in earlier work. When the wave front reaches a wall with partial permeability, the vapor compresses and the pressure on the wall increases. This increase in pressure causes a backflow until the vapor is compressed over the entire length.

Chapter V

STARTUP TRANSIENT OPERATION OF HEAT PIPES

5.1 INTRODUCTION

The transient behavior of vapor flow during the startup phase of heat pipe operation has been analyzed in order to examine the flow patterns for low- and high-input heat fluxes. Startup is a transient process through which the heat pipe starts its operation from a static condition and arrives at steady-state operation. The response of the vapor flow is an important design issue in dynamic thermal systems where a heat pipe is used to transfer heat following sudden increases in the heat load.

During a startup transient, the working fluid of a heat pipe may initially be very cold or frozen in the wick. Here the liquid is assumed to be very cold and the vapor, which is thermodynamically in equilibrium with the liquid, is at very low pressure. The vapor core response to a sudden-input heat flux or a sudden change in the condenser temperature is the primary focus of this work.

The vapor flow in heat pipes is a complicated problem because of the highly nonlinear nature of the governing equations and because of the inflow and outflow boundaries in the

evaporator and condenser. Different approaches have been used to simplify the problem. In most previous work, the vapor flow is analyzed under steady-state conditions as a one-dimensional (1D) flow (e.g., Edwards and Marcus[12]) and a 2D flow [17-19, 24]. In studies of the dynamic behavior of heat pipes, the vapor flow is modeled either as a quasi-steady flow [38] or as a 1D transient vapor flow along with friction coefficients approximated from a steady-state 2D model [37]. It has been shown by steady-state 2D analysis that the 1D vapor-flow model is not able to accurately predict the axial heat and mass transfer and pressure drop [14]. Furthermore, 2D steady-state studies indicate that flow reversal takes place in the condensation section under high heat flux [41]. It is therefore important to establish the conditions for this mode during transient operations.

In a theoretical study using a 1D transient model, Bystrov and Goncharov [31] showed that the time steps in the numerical calculations which are necessary to satisfy stability requirements are extremely small (order of 10^{-7}). The vapor dynamics of heat pipes was analyzed in Chapter Three, using a 2D transient model with the SIMPLER method. The primary advantage of SIMPLER is the staggered grid which makes the numerical scheme very stable and, consequently, the computational time very low. Although this method yielded interesting results, the resulting computational code is limited to low compressibility flows. However, in the startup mode of a heat pipe, there are regions of high as well as

low compressibility. Existing numerical codes for highly compressible flows, on the other hand, are only able to handle steady-state conditions because of their extremely small allowable time steps and, furthermore, they are not stable for low Mach-number problems.

The objective of this chapter is to thoroughly investigate the dynamic behavior of the vapor flow in heat pipes during the startup transient phase of its operation. The fully compressible governing equations of vapor flow are numerically solved using a transient 2D model, discussed in Chapter Two. The numerical scheme is fully implicit using a staggered grid, and it is stable for all Mach numbers between zero and one, which is a suitable range for the startup transient mode.

5.2 SOLUTION METHOD

The complete set of governing equations of the vapor flow in heat pipes were derived in Chapter Two. These equations in their nondimensional form are Eqs. (2.11) through (2.15). The boundary conditions associated with these equations are given by Eqs. (2.17) to (2.22). The vapor is initially stagnant and at thermodynamic equilibrium with the liquid in the wick structure. When the initial pressure and temperature are very low, and a rather high input heat flux is applied in the evaporator, a shock wave is created in the evaporation zone. This is shown in Fig. 5.1 for a liquid sodium heat pipe. The vapor is at, initially, $P_o = 10^{-2}$ atm and $T_o = 800$ K,

C-2

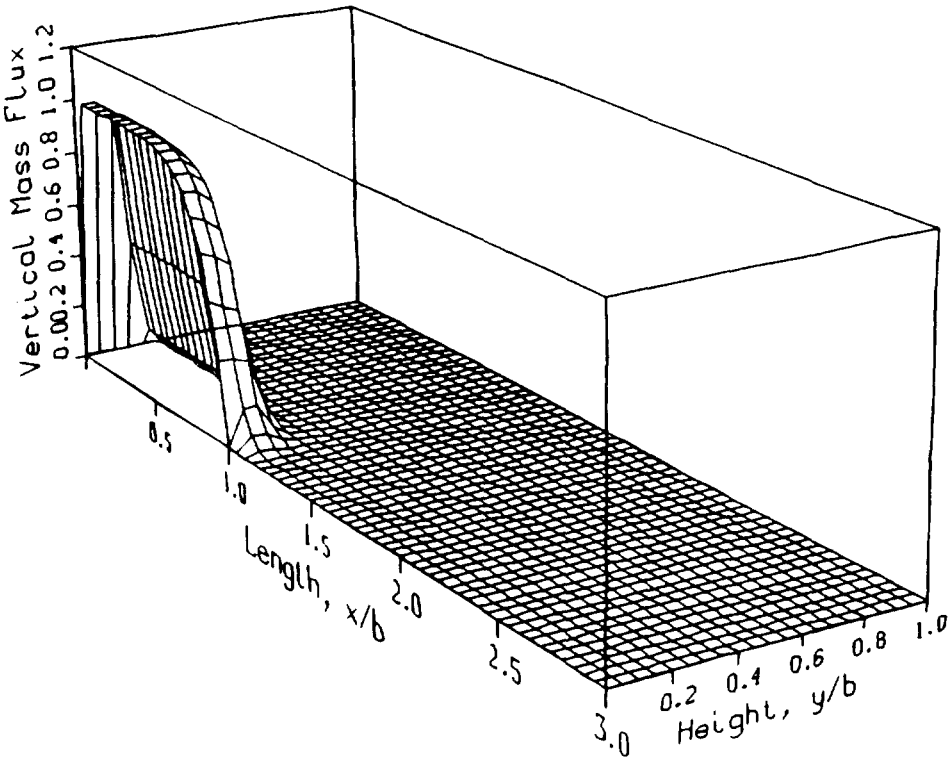

Fig. 5.1. Vapor flow in a heat pipe at the initial stage of the startup

and an input heat flux of 10^5 W/m^2 is applied at one end of the pipe. The high gradients at the shock wave makes the SIMPLER method, used earlier, inappropriate for the startup transient analysis. In Chapter Four the one dimensional forms of the governing equations were solved using standard methods such as upwinding and power law and a more recent scheme, CONDIF. It was shown that these schemes are well-behaved but that they

cause oscillations and overshoot at high compressibility and, except for CONDIF, they cause high numerical diffusion at low compressibility as well. The CONDIF scheme was also used by Issacci et al. [55] in a study of startup transient process in heat pipes. It was shown that for input heat fluxes more than 1 kW/m^2 in an Na-filled heat pipe, a shock is created in the evaporation region. Therefore, the CONDIF scheme was found to be unsuitable for shock capturing.

In Chapter Four it was shown that a centered difference scheme (CDS) used with nonlinear filtering yields a second order, stable solution in cell Reynolds-number problems and is able to capture a shock without oscillations. In this chapter, the same technique is used to solve the 2D form of the governing equations for a compressible vapor flow.

The governing equations are nonlinear and coupled. An iterative method is used to solve each equation separately, i.e., equations (2.11) to (2.15) for ρ, ρu, ρv, T, and p, respectively. The SOR method is used to solve the differenced equations. Iterations on the equations were stopped after convergence of all the variables. The convergency was assumed to be reached when the relative change of all variables in one time step was less than 0.5%. This iteration method required the least storage and fewest calculations.

5.3 RESULTS

The boundary conditions of inflow and outflow at different locations on the same boundary are highly nonlinear. Furthermore, the exit point of the evaporator and the entrance point to the condenser, on the bottom boundary, are mathematically singular points. The boundary conditions at these points have sharp gradients which perturb the numerical scheme. In order to avoid this problem, the inflow and outflow mass fluxes are multiplied by the factor tanh $\lambda(x-x_o)$. In the evaporator and in the condenser, x_o = 0 and 2, respectively. Depending on λ, this factor makes the gradients smoother at the singular points.

For the results shown in this chapter, the working fluid is liquid sodium at, initially, $P_O = 10^{-2}$ atm and $T_O = 800$ K. The geometry dimensions are $b = 5$ cm, $L_e = L_a = L_c = b$, and $\lambda = 5$. The results are shown in the following sections for low- and high-input heat fluxes and for the pressure drops along different sections of the heat pipe.

5.3.1 Error Analysis

The calculational grid for each computation was chosen by inspection of the calculated L^2-norm. The L^2-norm is defined as

$$L^2 - norm = \left[\frac{1}{NxNy} \sum_{i,j} \left(\frac{\phi_{i,j} - \phi^r_{i,j}}{\phi^r_{i,j}} \right)^2 \right]^{1/2} \qquad (5.1)$$

where Nx and Ny are numbers of grid points in x- and y-directions, respectively. Here, ϕ is one of the dependent variables (ρ, ρu, ρv, T, or P) and ϕ^r is the calculated ϕ on the finest mesh of calculations. Figure 5.2 shows the results of the error analysis for a sample calculation. With an increase in grid points, the L^2-norm error decreases exponentially, however, the computational time increases (Fig. 5.2a). In this sample analysis, for grid points greater than 21, the error does not decrease by much, whereas the corresponding computational time increases significantly. Therefore, for this case, the optimized grid point is 21.

The same error analysis is also carried out for time increments, Δt, using equation (5.1). In this case, ϕ^r is the result of calculations according to the smallest Δt. Figure 5.2(b) shows the L^2-norm error for different time increments. As expected, the error decreases as Δt decreases. The sample error analysis, described above, was carried out for different input conditions in order to choose the corresponding optimized grid points and time increments. For all the calculations presented below, $\Delta t = 10^{-2}$ to 10^{-3}.

5.3.2 Low-Input Heat Flux

Figure 5.3 shows the flow patterns in the vapor core for a low-input heat flux, $q_o = 10^5$ W/m^2. The Reynolds number based on the vapor thickness is $Re = 100$ and the computations were

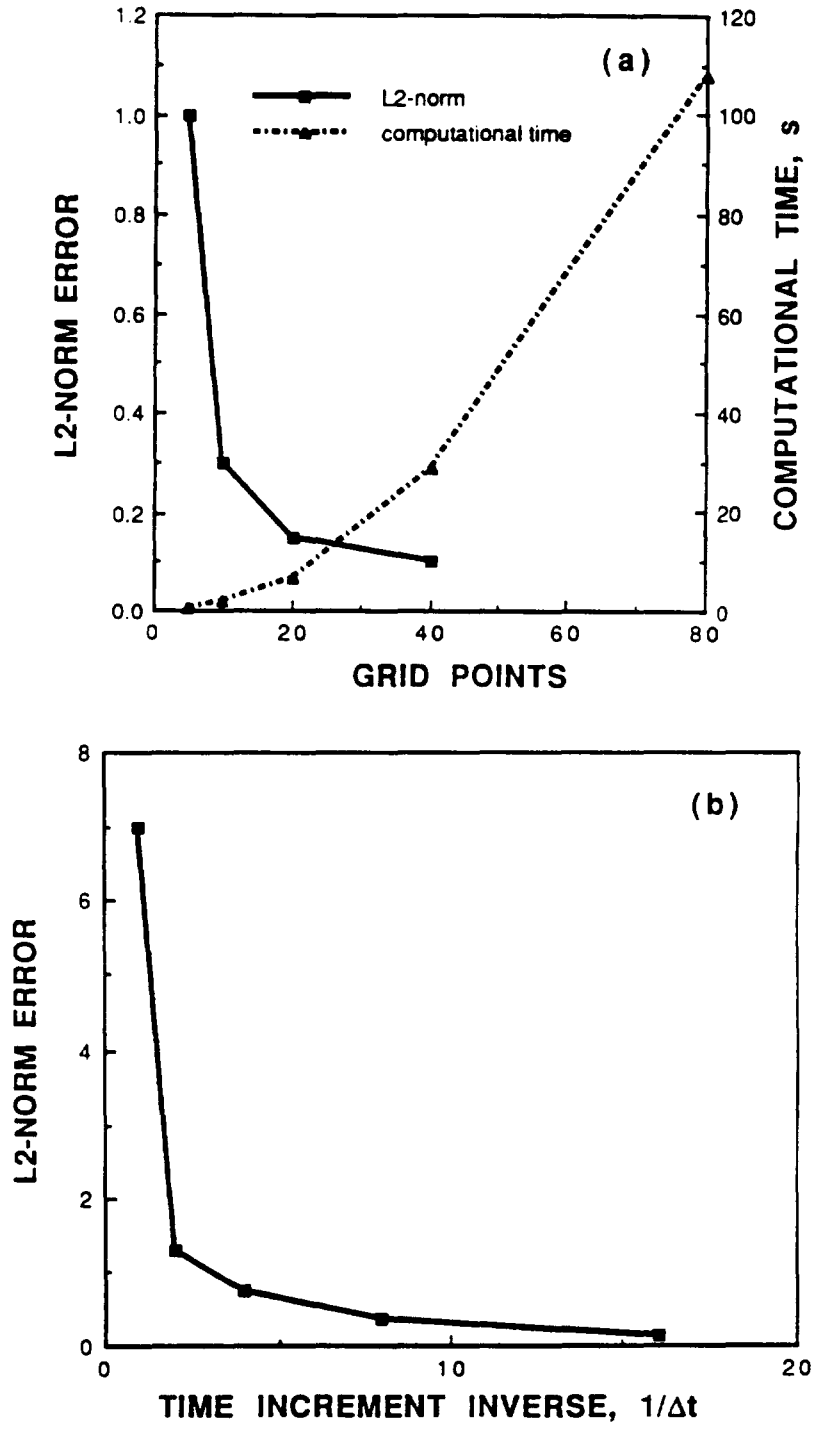

Fig. 5.2 L^2-norm error and computational time

done for an optimized grid of 21 x 61. The transient development of the vertical mass flux, ρv, at different times is shown in Fig. 5.3. At t= 0, the vapor is stagnant. Applying the input heat flux, evaporation takes place. Since the input heat flux is relatively high, a shock wave is created (Fig. 5.3a). The vapor flow develops above the evaporator and in the adiabatic region and the shock travels above the evaporator until it hits the upper boundary (Fig. 5.3b) where the vertical mass flux is blocked, ρv = 0. At this point, the vapor is compressed and the vapor pressure increases which causes a positive vertical pressure gradient and the shock reflects back (Fig. 5.3c). The figure also shows reverse flow in the top left corner which is caused by shock reflection. When the reflected shock reaches the lower boundary (Fig. 5.3d) and the vapor is compressed within the evaporation region, the vertical pressure gradient is reduced and the inflow mass flux tries again to fill the evaporation region (Fig. 5.3e). As the vapor fills the evaporation region (Fig. 5.3f), another shock reflection occurs and the flow reverses in the top left corner (Fig. 5.3g). Comparing Figs. 5.3d and 5.3g, the reverse flow after the second reflection is weaker than that in the first reflection. About eight to ten cycles of refill and reflection of mass flow are observed in the evaporation region before the process becomes steady (Fig. 5.3i). At each cycle the reverse flow is weaker and after four cycles there is no reverse flow. The vertical gradient in the mass flux, ρv, also decreases with each cycle.

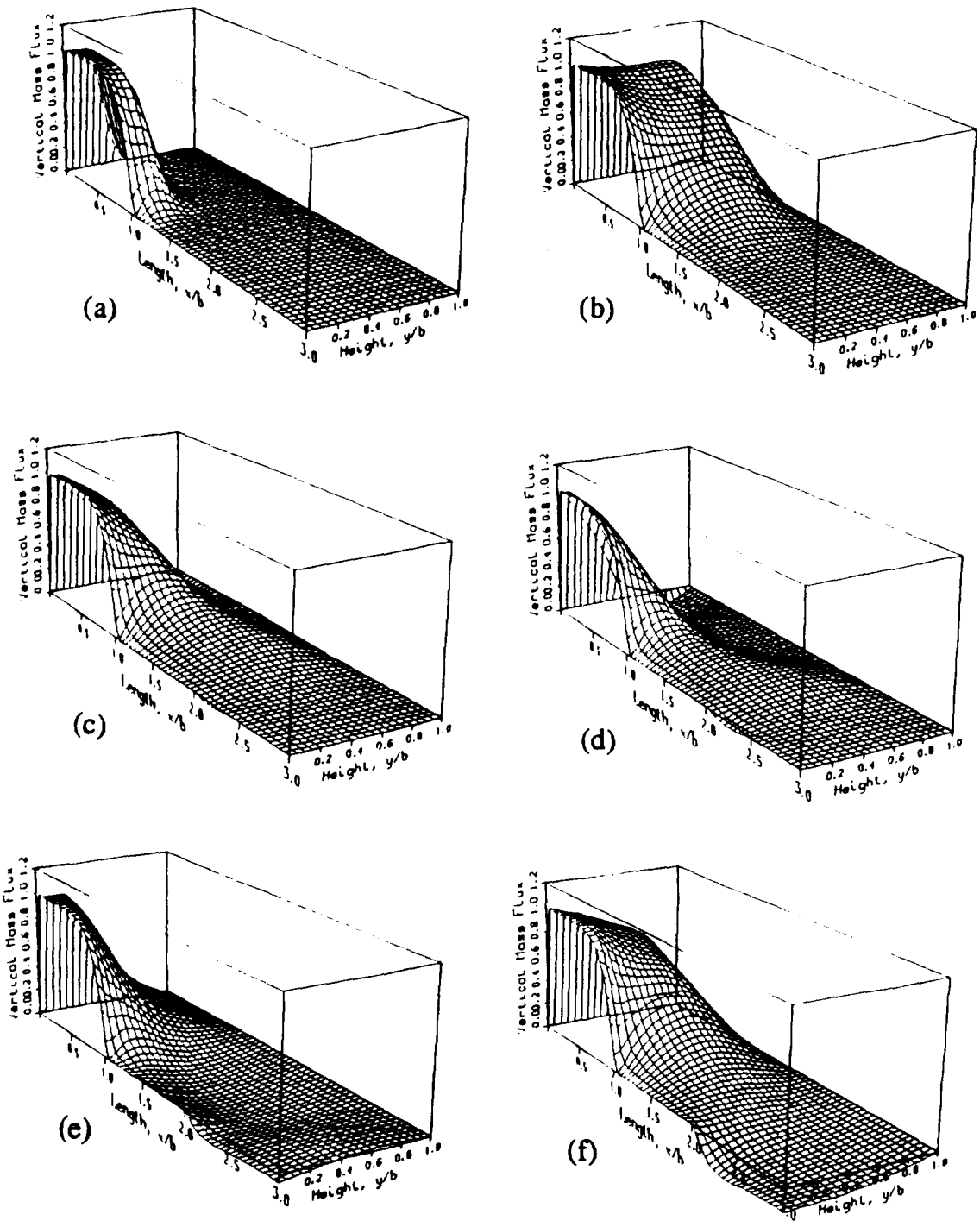

Fig. 5.3. Transient development of the vertical mass flux. Low-input heat flux

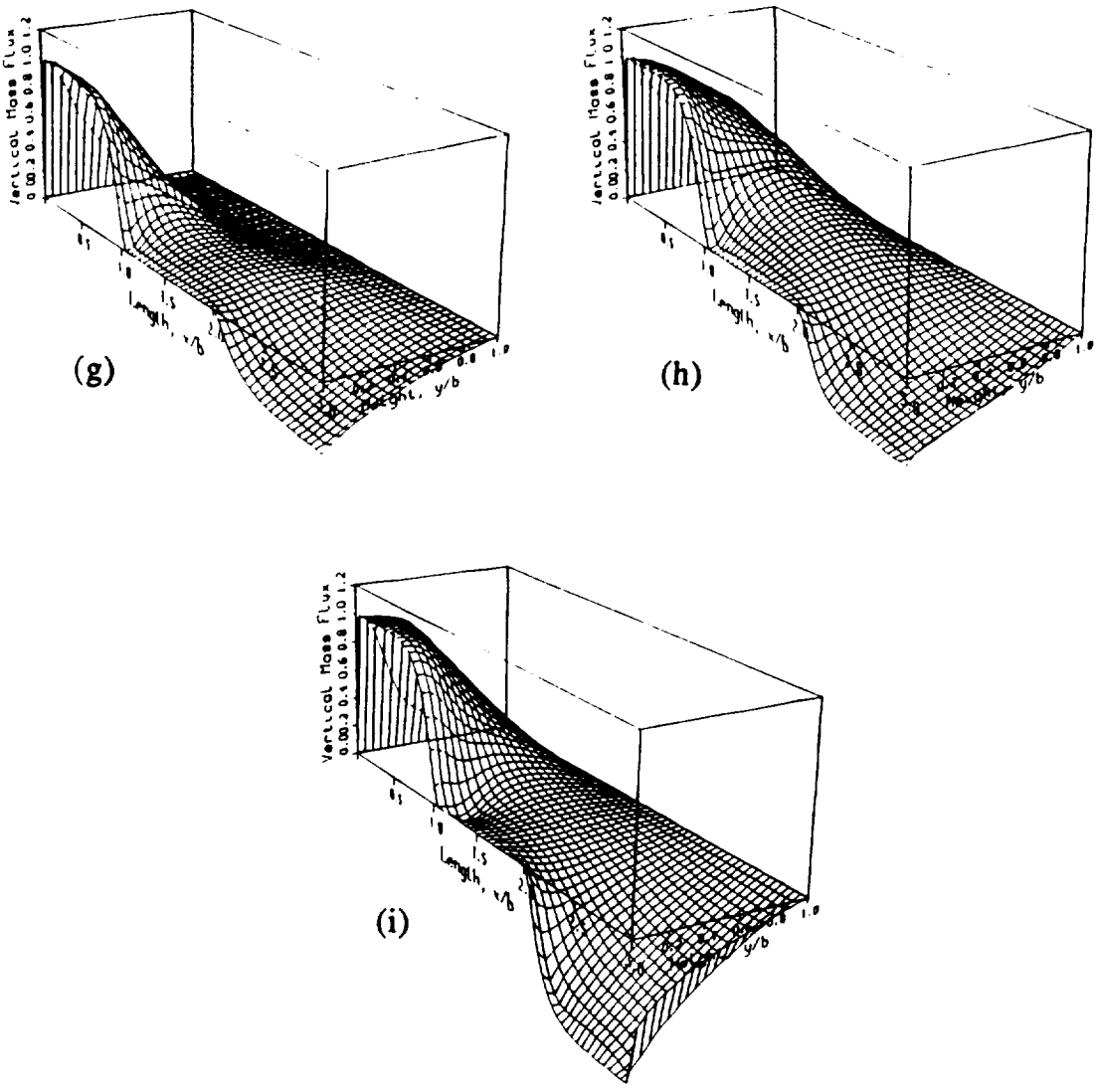

Fig. 5.3 (Con'd). Transient development of the vertical mass flux. Low-input heat flux

The transient flow pattern in the condensation region, $2<x/b \leq 3$, is also illustrated in Fig. 5.3. At early stages of the startup transient process, the vapor is at the same temperature as the liquid and, therefore, there is no condensation (Figs. 5.3a and 5.3b). When vapor at the higher temperature flows from the evaporation to the condensation region, the vapor temperature in the condenser increases. A temperature gradient is then established along the liquid layer since the temperature at the outer surface of the liquid layer is kept fixed, and condensation takes place (Fig. 5.3c). The vapor temperature in the condenser increases with time and, consequently, the condensation rate increases. At steady state, shown in Fig. 5.3i, the mass flow rate through the evaporator equals the mass flow rate out of the condenser.

5.3.3 High-Input Heat Flux

In this section the transient flow patterns are shown for a relatively high heat flux, $q_o = 10^6$ W/m^2. The corresponding Reynolds number in this case is $Re = 1000$ and the optimized grid is 41 x 121. Figure 5.4 shows the transient development of the vertical flow, ρv, at different times. In the evaporator region, multiple shock reflection and refill of vapor is observed to be the same as that for the low-input heat flux discussed above. In this case, however, the reversed flow caused by the shock reflection

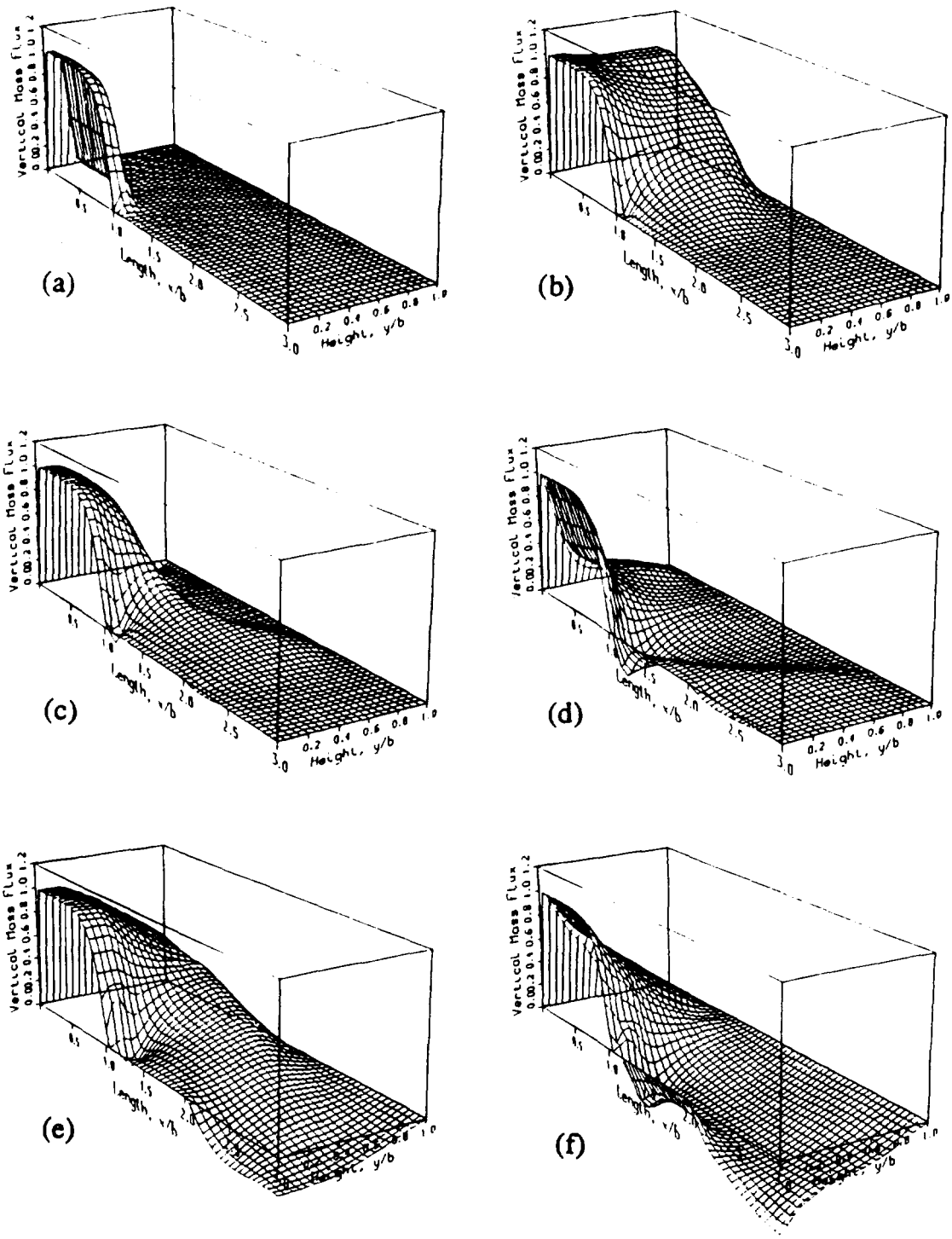

Fig. 5.4. Transient development of the vertical mass flux.
High-input heat flux

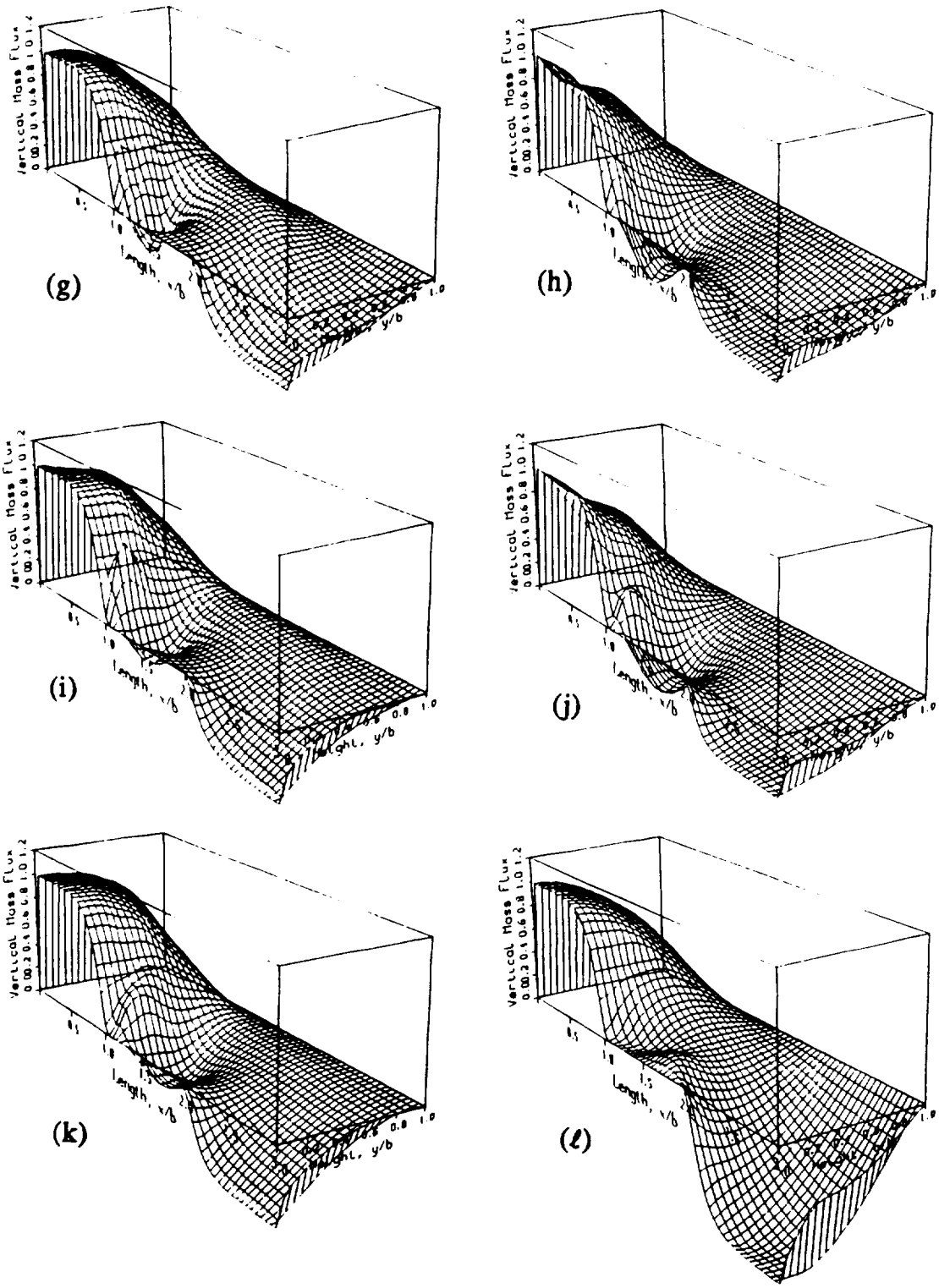

Fig. 5.4 (Con'd). Transient development of the vertical mass flux. High-input heat flux

develops with time and is sustained as the process reaches steady-state operation.

At high-input heat flux the flow pattern in the adiabatic region, $1 < x/b \leq 2$, is significantly different from that for lower heat fluxes. Figure 5.4d shows that when the shock reflection reaches the lower boundary of the evaporator, circulation is initiated in the adiabatic region. This circulation ceases when the vapor flow refills the evaporator region (Fig. 5.4e). However, the second reflection will cause a stronger circulation in the adiabatic region, as shown in Fig. 5.4f. Figures 5.4g through 5.4ℓ demonstrate the subsequent sets of reflection and refill of the vapor flow with circulation strength increasing with time. When the process reaches steady-state conditions, circulation occupies a significant portion of the region. Circulation in the adiabatic region was also observed in Chapter Three in the analysis of the operating transient mode of heat pipes.

In order to show the overall picture of flow pattern development, Fig. 5.5 was prepared to depict the vapor flow fields at different times. In this figure the arrow indicates the flow direction and the tail indicates the magnitude of the flow. Figure 5.5a shows the flow field at an early stage of the transient process after the first shock reflection. Here the flow reversal is shown to be in the left top corner of the evaporation region. The shock reflection initiates flow circulation at the entrance to the adiabatic region shown in Fig. 5.5b. Vortex formation in the adiabatic region

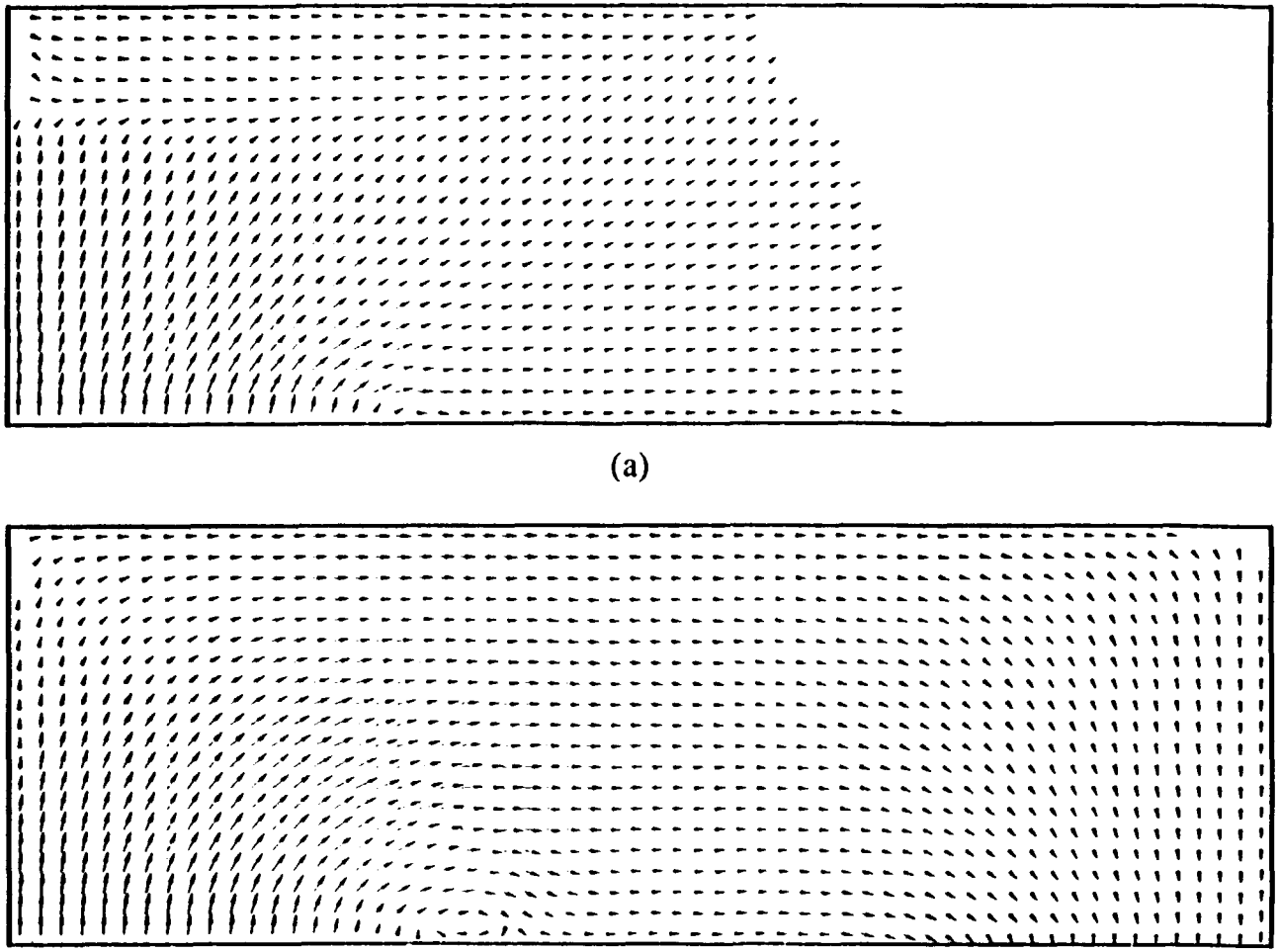

(a)

(b)

Fig. 5.5. Vapor flow fields at different time levels

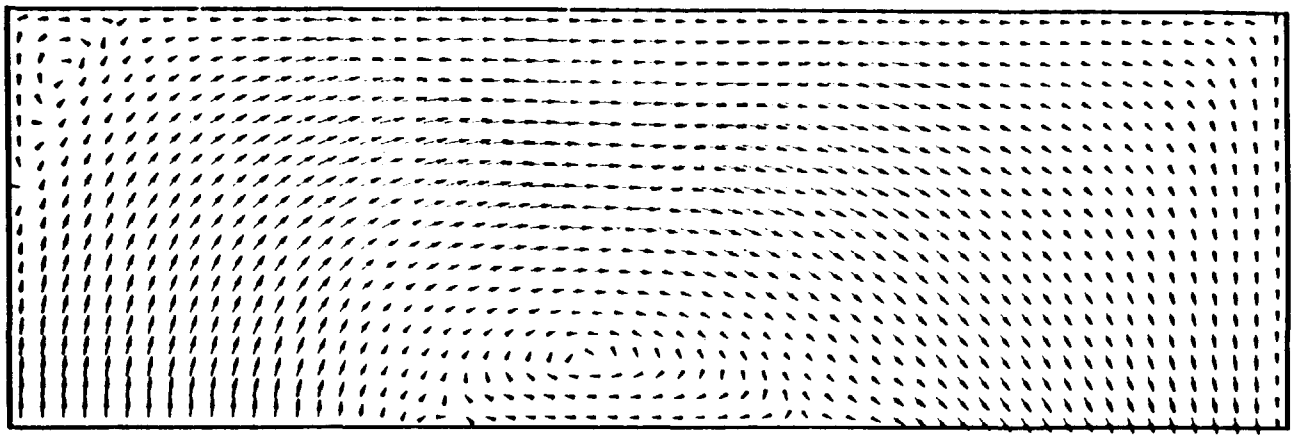

(c)

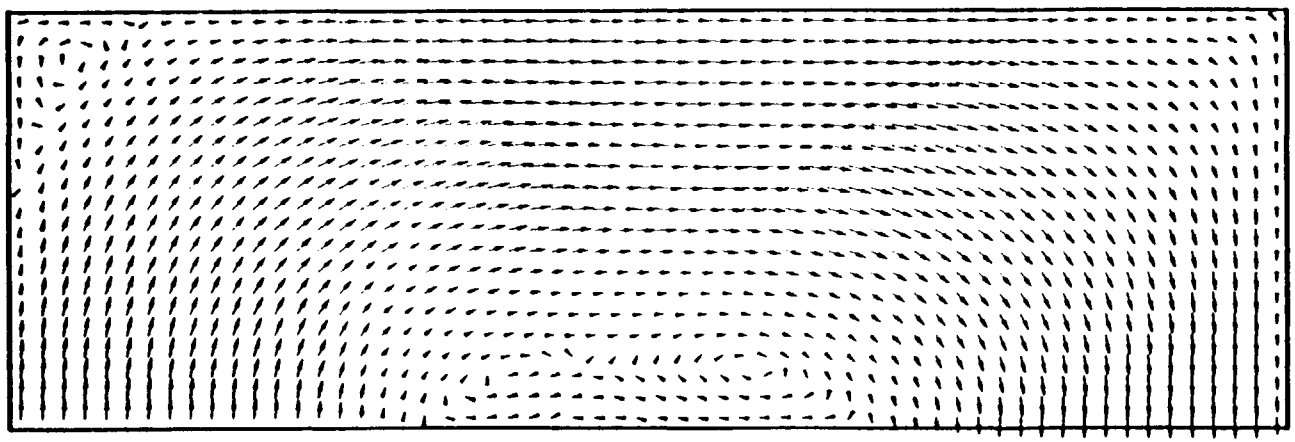

(d)

Fig. 5.5 (Con'd). Vapor flow fields at different time levels

develops with time to a stronger flow circulation (Fig. 5.5c) and another vortex can be seen in the left corner of the evaporation region. In the flow field at steady state (Fig. 5.5d), it is seen that flow circulation in the adiabatic region develops to two vortices.

One of the limitations on the heat pipe operation is the sonic limit. When the vapor velocity reaches the speed of sound the vapor flow is choked, which limits the heat flux through the pipe. Therefore, the maximum Mach number in the vapor flow should be equal or less than one. Figure 5.6 shows the development of the Mach number profile with time along the pipe, for high-input heat flux (q_o = 10^6 W/m^2, corresponding to the results presented in this section). It is shown that the Mach number is below one at the initial stage of the transient process. The vapor flow develops in the evaporation region and the Mach number increases with time. The vapor velocity reaches the speed of sound at the exit of the evaporator, where the Mach number is equal to one.

5.3.4 Pressure and Pressure Drop

One of the major issues in designing a heat pipe is to correctly calculate the pressure drop along the vapor core in different sections of the pipe. The correlations widely used in these calculations are based on simple 1D steady-state analysis. In this section, the pressure drops in different sections of the heat pipe are shown as functions of time. The calculated pressure drops

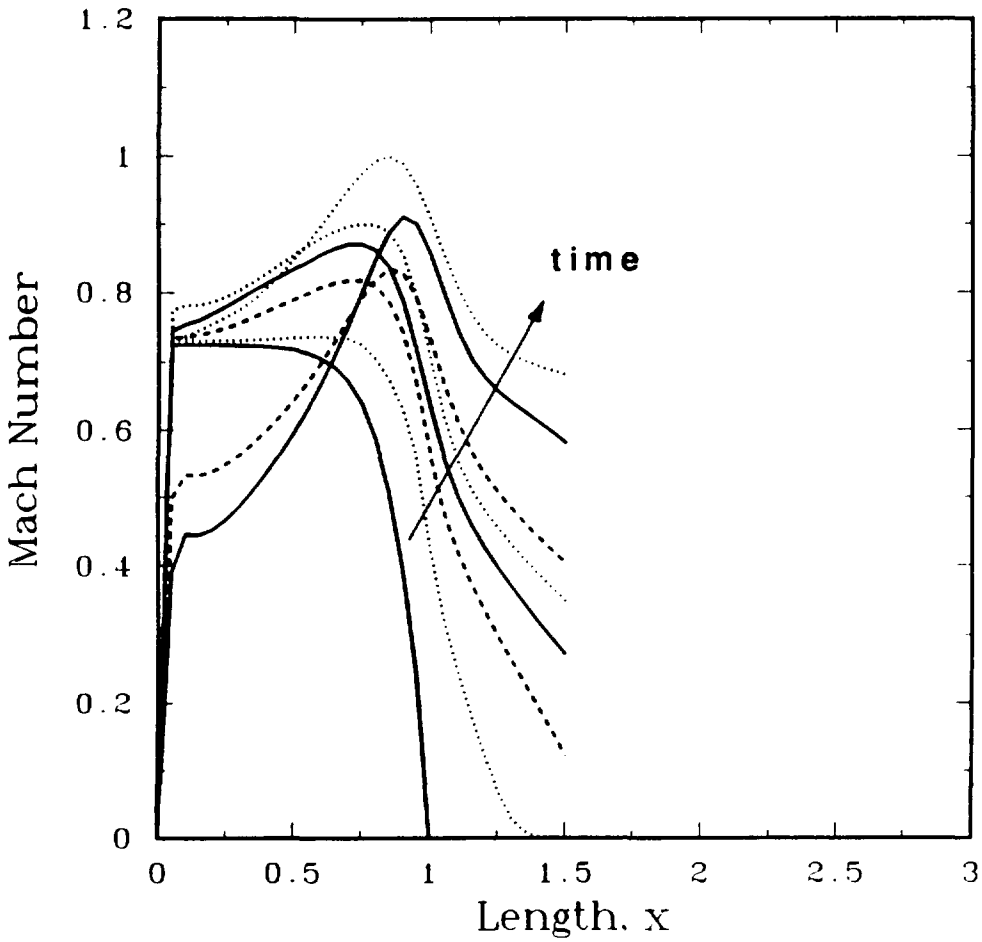

Fig. 5.6. Mach number profiles at different times; high-input heat flux

for high- and low-input (q_o = 10^6 W/m^2, and 10^4 W/m^2, respectively) heat fluxes are shown in Fig. 5.7 for different times during the transient phase. Solid lines show the maximum pressure drop in a specific region of the pipe. Averaging the pressure along the vertical cross section of the pipe and then calculating the maximum-averaged pressure drop yields

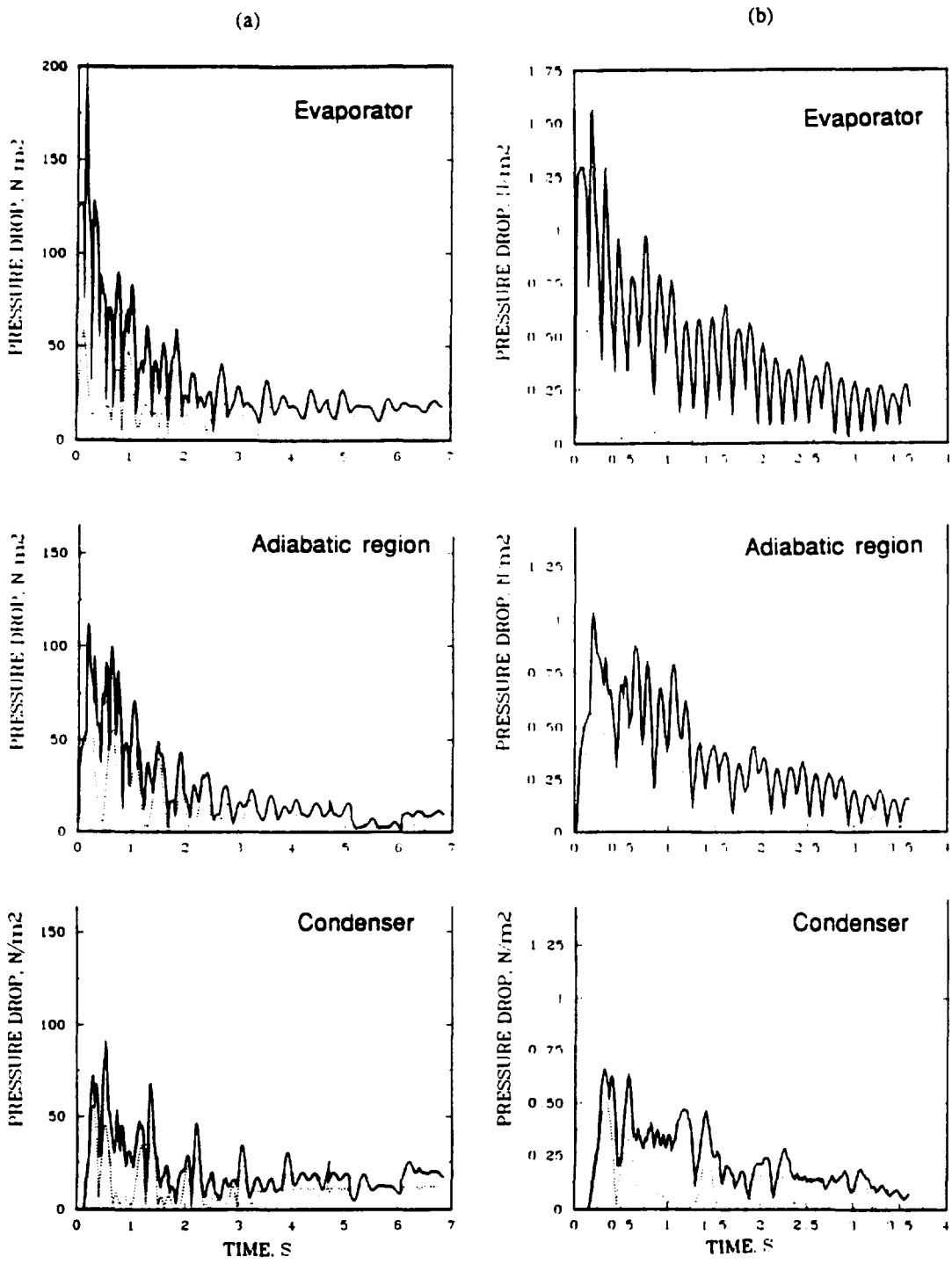

Fig. 5.7 Calculated pressure drops for (a) high- and (b) low-input heat fluxes (—— and ··· = maximum and maximum-averaged pressure drops, respectively)

interesting results which are shown (dotted lines) for different times in different sections. Both the maximum and the maximum-averaged pressure drops display nearly periodic oscillation until they converge to a constant value at steady state. Pressure oscillations are caused by multiple shock-wave reflections in the evaporation region (Figs. 5.3 and 5.4) and at each shock reflection, the local pressure increases significantly. Consequently, a large pressure difference is created along the pipe.

Another interesting result which can be seen on Fig. 5.7 is that the pressure drop is significantly higher during the initial period of the startup transient of heat pipe operation. The mean value of the pressure drop decreases with time, and at steady state its value is less than 10% of the initial pressure drop. Therefore, if a heat pipe is designed to operate in the transient mode, the use of steady-state correlations may result in significant errors.

Tien and Rohani [18] showed that the cross-sectional averaged pressure along a heat pipe is greater than the pressure calculated by Bankston and Smith [15] using a 1D analysis. Here we compare the cross-sectional averaged pressure with the calculated 2D pressure by comparing the maximum pressure drops in both cases. Although the maximum-averaged pressure drops (dotted lines on Fig. 5.7) converge to the maximum pressure drop as the process approaches steady state, it is significantly lower

during the initial transient time. This emphasizes the need for a 2D vapor flow model in an overall heat pipe transient analysis.

The pressure drop along the pipe, as mentioned before, plays an important role in the design of a heat pipe. In addition, the pressure in the evaporator may cause limitations on heat pipe operations. When a shock wave reflects in the evaporation region and the local pressure increases, the increase in the overall pressure of the evaporator may affect the evaporation rate. In order to study this aspect, the averaged (solid lines) and the saturated (dotted lines) vapor pressures in the liquid-vapor interface in the evaporator are shown as functions of time in Fig. 5.8. Here again, the periodic behavior of pressure is evident. During early transient times, the averaged pressure in the evaporator is sometimes larger than the saturated pressure. This will affect the evaporation process by decreasing the evaporation rate. Furthermore, whenever, the vapor pressure is greater than the saturated pressure, condensation takes place by nucleation of mists in the vapor. In this case the flow is not homogeneous anymore and a two-phase flow analysis should be incorporated.

5.3.5 Friction Factor

The total pressure drop in the vapor core is needed in designing a heat pipe. The averaged friction factor along the pipe is calculated by

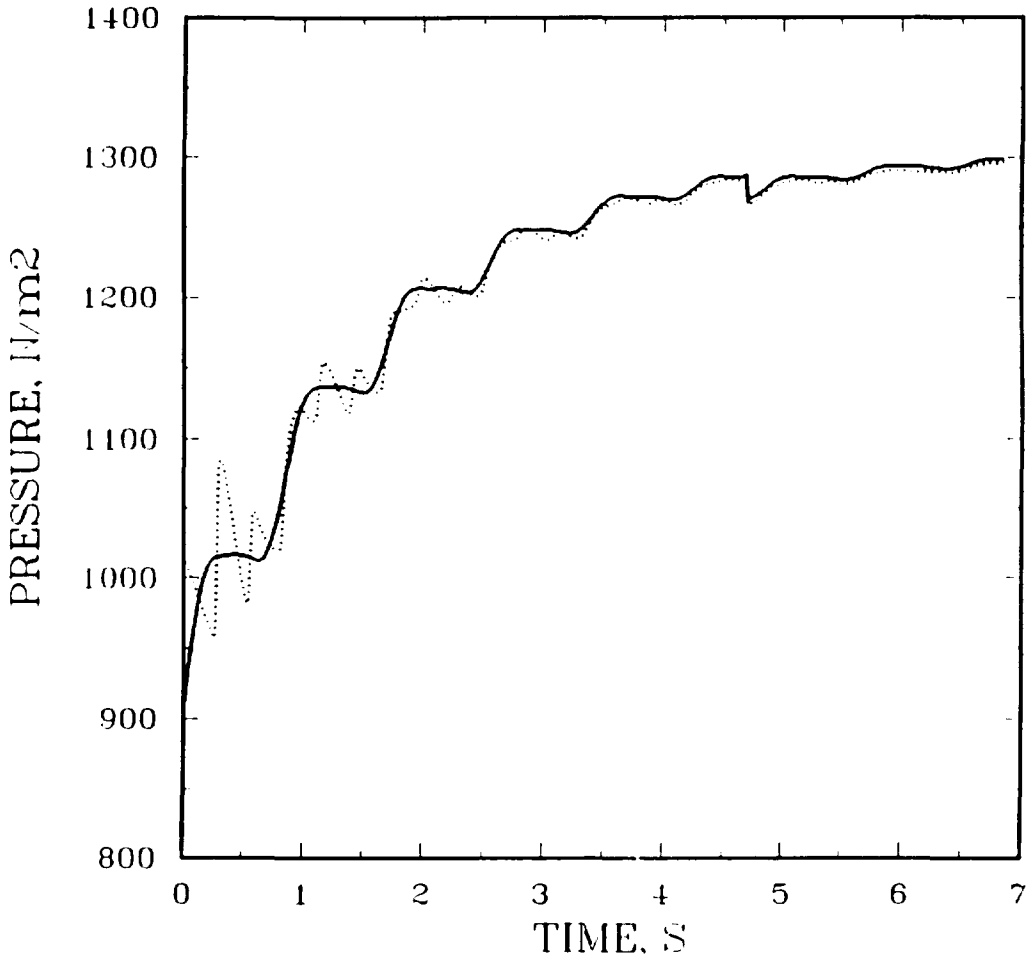

Fig. 5.8 Averaged (---) and saturated (···) vapor pressures in the evaporator

$$C_f(t) = \frac{\frac{1}{L}\int_0^L \tau_w dx}{\frac{1}{2}\rho u^2} = \frac{\frac{1}{L}\int_0^L \mu \left.\frac{du}{dy}\right|_{y=0} dx}{\frac{1}{2}\rho u^2} \qquad (5.2)$$

Figure 5.9 shows the ratio of the averaged friction factor and its value at steady state, $C_f(t)/C_f(\infty)$, for low- (Fig. 5.9a) and high- (Fig.

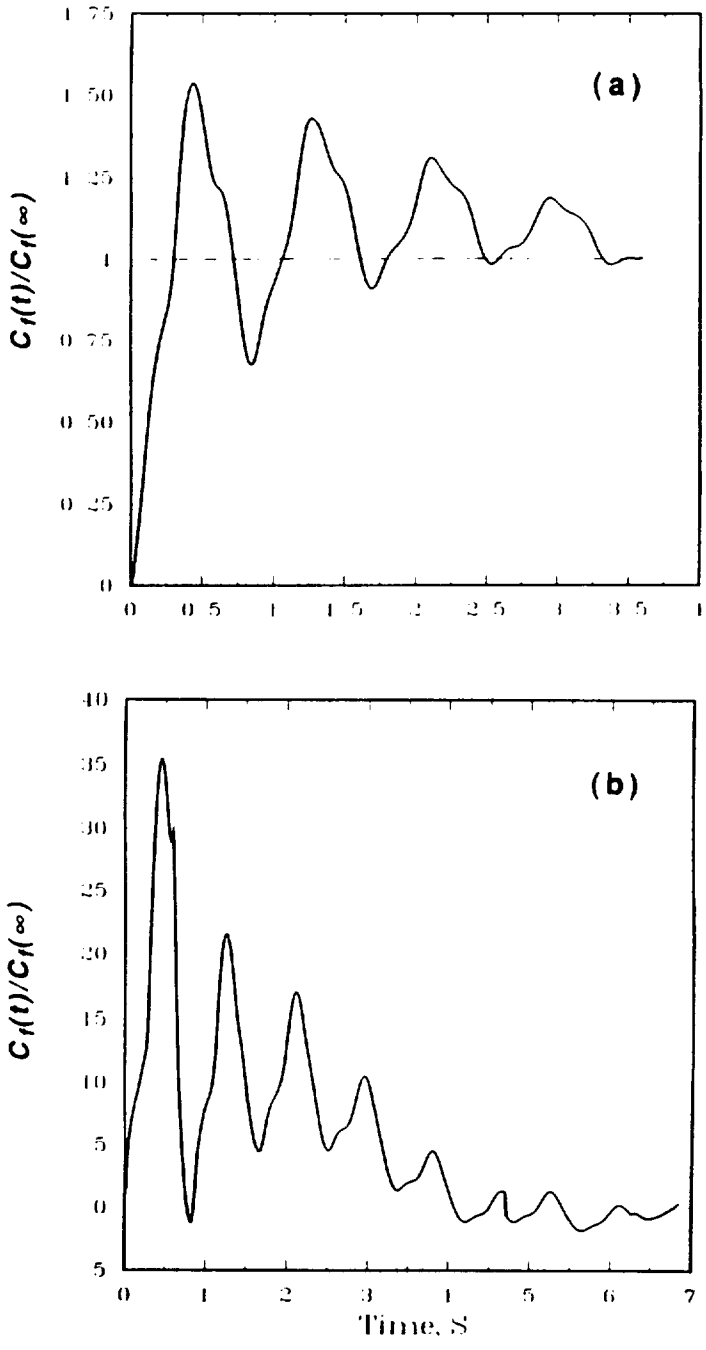

Fig. 5.9. Friction factors. a) Low-input heat flux, b) high-input heat flux

5.9b) input heat fluxes. The friction factor oscillates periodically because of the shock reflections, and converges to a constant value at steady state. Figure 5.9a shows that for low-input heat flux ($\dot{q}''_o$ = 10^4 W/m^2), the maximum-friction factor during the transient phase, is about %50 more than its value at steady state. For high-input heat flux ($\dot{q}''_o$ = 10^6 W/m^2), the friction factor is about 35 times more than its steady-state value (Fig. 5.9b). This implies that in designing a heat pipe for transient operations, the steady-state correlations may cause a significant error.

5.4 CONCLUSIONS

A nonlinear filtering technique has been used to analyze the startup vapor dynamics in heat pipes. Large variations in vapor compressibility during the transient phase render it inappropriate to use the SIMPLER scheme, as well as standard schemes for the disretization of the advective terms.

For a high heat flux, the startup transient phase involves multiple shock reflections from the line of symmetry in the evaporator region. Each shock reflection causes a significant increase in the local pressure and a large pressure drop along the heat pipe. Furthermore, shock reflections cause flow reversal in the evaporation region and flow circulations in the adiabatic region. The vapor vortex formation in the evaporator is only transient and is observed to disappear as the dynamics approach steady state. However the circulation in the adiabatic region

grows with time, and in the steady-state condition the circulation occupies a significant portion of the region.

The maximum- and maximum-averaged pressure drops in different sections of the heat pipe oscillate periodically with time because of the multiple shock reflections in the evaporator. The pressure drops converge to a constant value at steady state. However, they are significantly higher than their steady-state value at the initiation of the startup transient.

The pressure increase due to shock reflection may cause the overall pressure of the evaporator to be greater than the saturated vapor pressure. When this occurs, condensation takes place by mist nucleation in the vapor. Therefore, the condensation rate is expected to decrease.

The time for the vapor core to reach a steady-state condition depends on the input heat flux, the heat pipe geometry, the working fluid, and the condenser conditions. However, the vapor transient time is on the order of seconds. Depending on the time constant for the overall system, the vapor transient time may be very short. Therefore, the vapor core may be assumed quasi-steady in transient analysis of a heat pipe operation.

Chapter VI
EXPERIMENTS: NEEDS AND DIFFICULTIES

6.1 INTRODUCTION

Transient behavior of the heat pipe internal flows needs to be examined experimentally to understand and properly model the physical phenomena governing their behavior. The experimental data are needed to be compared with and verify the theoretical results. Experimental studies of heat pipe dynamics are very limited in the literature. Most of the experiments were carried out to measure only the maximum possible input heat flux and/or the temperature of the heat pipe external surface [27, 28]. These data are limited to few working fluids and operational conditions. Experimental data for the vapor flow in heat pipes are not available because of the complexity and sensitivity of the flow to external objects. The standard measurement methods like hot wire anemometry or thermocouples cannot be used to measure the vapor velocity and temperature. These measurement tools will disturb the energy transport process in the pipe and the results will not be reliable for comparison with the analysis.

The following is description of an experimental heat pipe, designed for transient vapor flow measurements. Then the optical measurement methods, which are non-invasive and unique for heat pipe internal flow measurements, are discussed. Experimental studies on the dryout and rewet of the heat pipe wick structure are also included.

6.2 EXPERIMENTAL APPARATUS

Figure 6.1 shows a schematic diagram of the experimental apparatus. A rectangular pipe has been designed and built to simulate a heat pipe. The bottom of the pipe is a plane wide and thin channel which contains the working fluid. Two layers of stainless steel mesh (300 series, 400 mesh) are fixed on top of the liquid channel to serve as the wick structure. The axial sides of the pipe are made of glass to permit flow visualization. The top of the pipe is insulated. One end of the bottom plate is heated by patch heaters which supply up to 1.55 W/cm^2. The other end is cooled by air flow. The middle region of the bottom plate is insulated to approximate the adiabatic conditions.

Freon 11 and freon 113 are chosen as working fluids. These fluids have low latent heats and low boiling points and are easy to handle. The low latent heat allows one to induce a liquid-vapor phase transition at low applied heat fluxes. A scaling analysis might be used to generalize the results to other fluids.

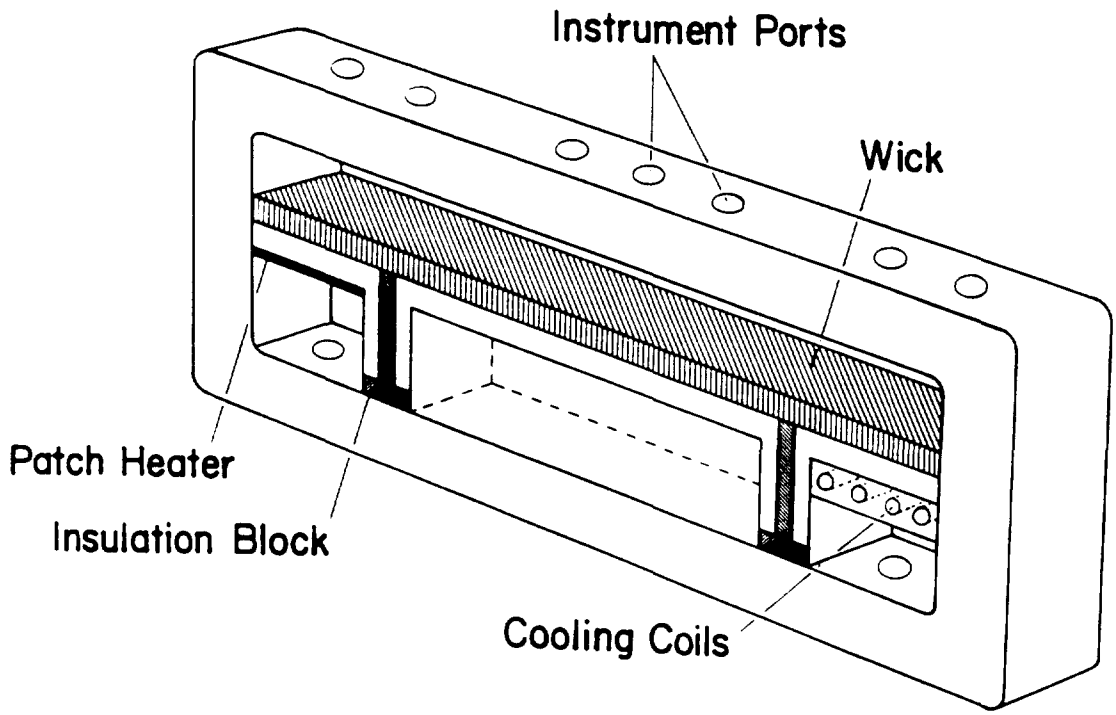

Fig. 6.1 Experimental rectangular heat pipe

The axial and vertical velocity components are measured using Laser Doppler Anemometry. The temperature and concentration profiles in the vapor core are measured simultaneously using twin beam laser holographic interferometry. These methods are described briefly in the following.

6.3 OPTICAL METHODS

Optical methods have been used for many years in heat and mass transfer measurements due their unique advantages. These methods do not disturb the examined process and the information

of the whole field is recorded on photographs, which has the advantage on the methods of point by point measurements. Furthermore, the measurements are inertialess and therefore, very fast phenomena can be investigated [56].

In this section, the use of optical methods in heat pipe experiments are discussed. The laser Doppler anemometry is used for measuring the axial and vertical velocity components of vapor flow. The advantages of the twin beam holographic interferometry are discussed as a means of measuring both the temperature and concentration distributions in the vapor core, simultaneously.

6.3.1 *Holographic Interferometry*

Interferometric methods are based on differences in lengths of the optical paths. Among these methods, holographic interferometry is the cheapest and easiest to construct with a comparative accuracy [56]. However, a highly coherent light is needed. The single beam holographic interferometry is first illustrated. Then it will be shown how this method can be modified to twin beam interferometry.

Single Beam Interferometry

Figure 6.2 is a schematic diagram of a single beam interferometer. The light source is a laser. The laser beam is split into an object beam and a reference beam. Each beam is passed through a microscope objective and a collimating lens and

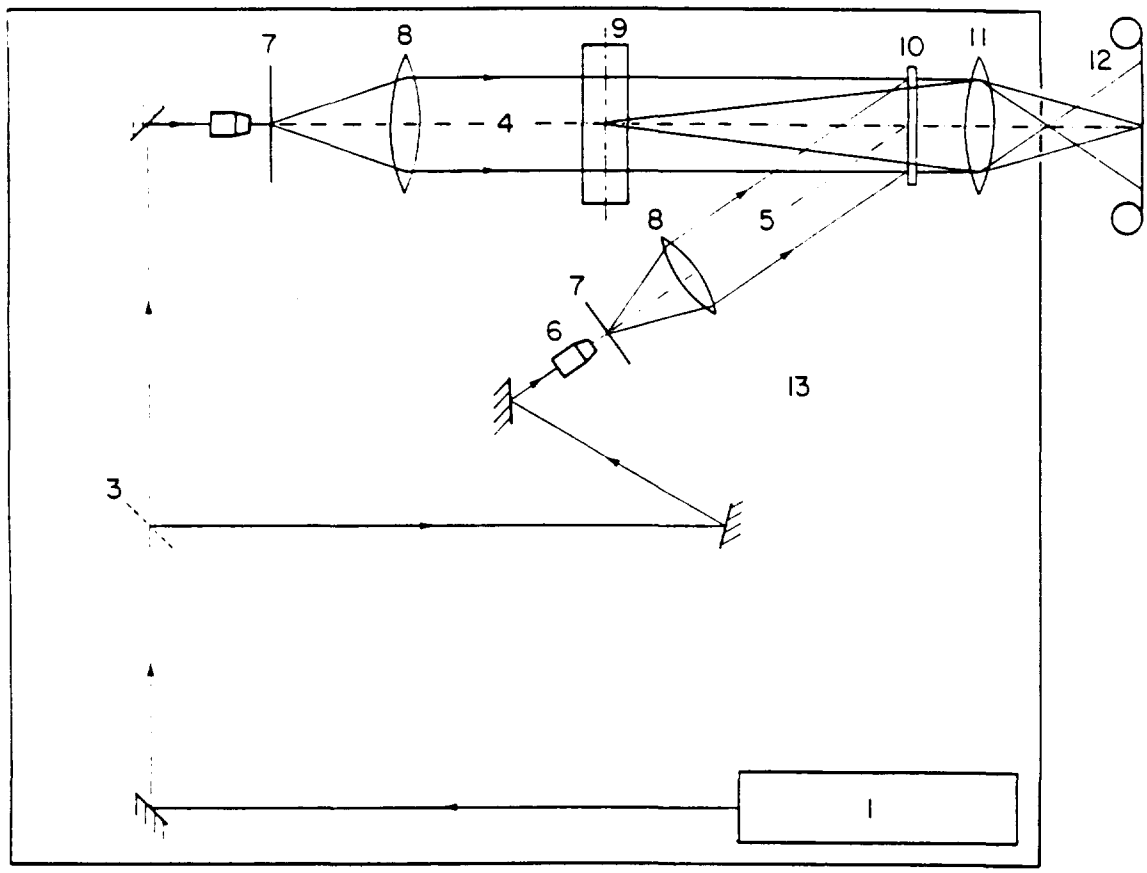

Fig. 6.2 Schematic of single beam holographic interferometer
1. Helium-Neon laser, 2. Argon laser, 3. variable beam splitter, 4. object beam, 5. reference beam, 6. microscope, 7. pinhole, 8. collimating lens, 9. test section, 10. holographic plate, 11. lens, 12. camera, 13. air-suspension table, 14. shutter

expanded to a parallel beam. The reference beam falls directly on the hologram plate, whereas the object beam passes through the experimental apparatus and then intersects the reference beam on the hologram plate.

In real-time holographic interferometry the photographic plate is exposed before the experiment starts, and the comparison beam is recorded. The photograph plate is developed and fixed while it stays in its place. The comparison beam is then reconstructed by illuminating the hologram with the reference beam. After the experiment starts a phase change occurs in the object beam and illumination of this beam on the hologram produces interference fringes. Changes in the interference pattern due to changes in the process can be continuously observed or photographed.

Interferometric methods are based on the measurement of variations of the refractive index in the test section. These variations may be caused either by temperature, concentration or pressure gradient fields. Then any of these fields alone can be determined by evaluation of the interferogram. However, if the refractive index is changed due to temperature and concentration changes simultaneously, an interferogram produced by a single beam interferometer may not be adequate to evaluate the temperature and/or concentration fields. This difficulty can be overcome by using two laser beams with two different wavelengths. This method is called twin beam (or two-wavelength) holographic interferometry and was first proposed by Mayinger and Panknin [57].

Twin Beam Interferometry

The first accurate results were obtained by Panknin [58]. Using twin beam interferometry he found good results for measurement of the temperature and concentration in simultaneous heat and mass transfer along a heated vertical plate and a horizontal cylinder with sublimation and the temperature and fuel distributions in a flame.

Figure 6.3 shows the required experimental arrangement. The twin beam interferometer is very similar to that of the single beam shown in Fig. 6.2. Here, two lasers, an Argon laser with wavelength λ_j =457.9 nm and a Helium-Neon laser with wavelength λ_k =632.8 nm, are used as light sources. The two beams lie on a horizontal plane and are perpendicular to each other when they intersect on the beam splitter. Therefore, both object and reference beams consist of two different wavelengths.

The exposure technique in twin beam interferometry is similar to that of the single beam. Before the experiment is started, the comparison beam, which now consists of two wavelengths, is recorded on a photograph plate. The photograph plate is developed and fixed. Now, if the laser beam with the wavelength, say, λ_j, is blocked, both reference and object beams will have wavelength λ_k. Then by illuminating the reference beam on the hologram, the comparison beam is reconstructed. The object beam which passes through the test section is illuminated on the hologram and produces an interference pattern for wavelength λ_k. By shining the

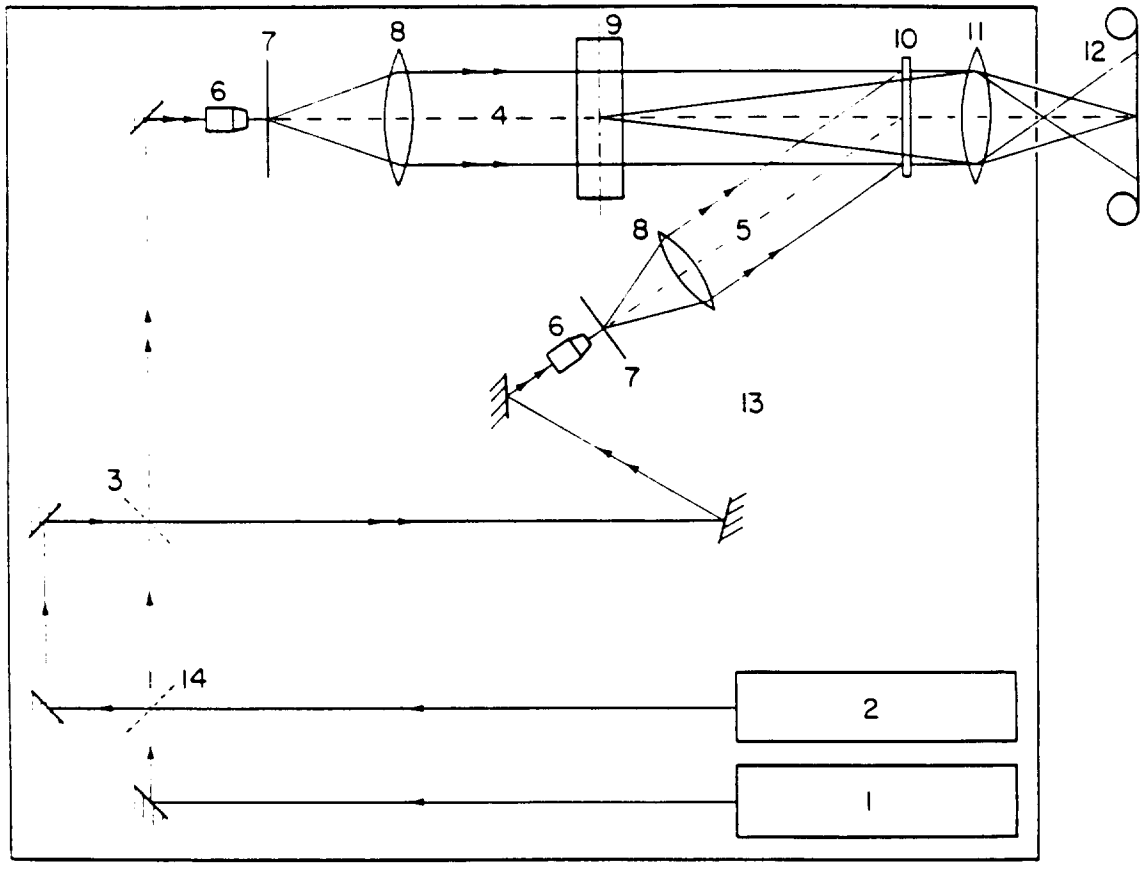

Fig. 6.3 Schematic of twin beam holographic interferometer
1. Helium-Neon laser, 2. Argon laser, 3. variable beam splitter, 4. object beam, 5. reference beam, 6. microscope, 7. pinhole, 8. collimating lens, 9. test section, 10. holographic plate, 11. lens, 12. camera, 13. air-suspension table, 14. shutter

laser beam of wavelength λ_j, another interference pattern is produced for wavelength λ_j.

The main advantages of this technique is that only one plate is developed which includes information from both wavelengths, and two interference patterns are produced by shining each laser beam, separately. Two sets of fringes are, then, evaluated to determine the temperature and concentration profiles for the tested medium. The evaluation method of fringes is discussed in the following section.

6.3.2 *Theory of Twin Beam Interferometry*

The following assumptions are made in development of the governing equations [38]:

1. The optical system is perfect, the experimental setup is mechanically stable and the lasers are ideal.
2. The object beams with the wavelengths λ_j and λ_k are ideal parallel waves.
3. The variation of the refractive index is only two dimensional and no variation in the beam direction.
4. No reflection of beam due to gradients of the refractive index.
5. Refractive index is constant outside of the test section and during recording of the comparison beams.
6. The holographic construction is perfect.

With the above assumptions the interference pattern depends only on the variation of the refractive index. In holographic interferometry the object beam, passing through the test section at different times, is superimposed on the comparison

beam, and therefore, reveal the difference in optical pathlengths in two exposures. Expressed in multiple S of the wavelength λ, this difference is written as

$$S(x,y,\lambda)\cdot\lambda = l\{n(x,y,\lambda)-n_{-}\} \tag{6.1}$$

where l is the width of the test section, in which the refractive index varies because of temperature and concentration gradients. The interference pattern shows the change of the refractive index between the recorded comparison beam (constant temperature T_{-} and constant concentration C_{-}, yield a constant refractive n_{-}) and the "measurement" beam.

An extinction of light occurs for

$$|S| = \frac{1}{2},\frac{3}{2},\frac{5}{2}\cdots \qquad \text{(dark fringes)}, \tag{6.2}$$

and an amplification for

$$|S| = 1,2,3... \qquad \text{(bright fringes)}. \tag{6.3}$$

The interference fringes are points of the same refractive index change. With temperature and concentration gradients the refractive index variation depends on both gradients. Therefore, a relationship has to be found between the refractive index change

due to the temperature gradient and that due to the concentration gradient.

The molar refractivity $N(\lambda)$, is related to the refractive index by the Lorentz-Lorenz equation as follows

$$N(\lambda)=\frac{n(\lambda)^2-1}{n(\lambda)^2+2}\times\frac{M}{\rho}\,, \tag{6.4}$$

where M is the molecular weight and ρ is the density. Fortunately the molar refractivity does not depend on temperature and pressure, but it varies with wavelength. This is the basis for the twin beam interferometry.

For gases with $n\approx 1$, Eq. (6.4) is approximated quite accurately by the Gladstone-Dale equation

$$N(\lambda)=\frac{2M}{3\rho}[n(\lambda)-1]. \tag{6.5}$$

For the ideal gases the density, ρ, can be replaced by the total pressure, p, and the temperature, T, to get

$$N(\lambda)=\frac{2RT}{3p}[n(\lambda)-1], \tag{6.6}$$

where R is the gas constant. The molar refractivity, $N(\lambda)$, for a mixture of two components is given by

$$N(\lambda) = C_a N_a(\lambda) + C_b N_b(\lambda), \tag{6.7}$$

with $C_a + C_b = 1$. In the above equation C_a and C_b are the concentration of the components a and b in the mixture and $N_a(\lambda)$ and $N_b(\lambda)$ are the molar refractivity of the components in their pure form.

Combining Eqs. (6.1), (6.6), and (6.7) yields

$$S(x,y,\lambda).\lambda = \frac{3pl}{2R}\left\{\frac{1}{T(x,y)}\left[N_a(\lambda) + C_b(x,y)(N_b(\lambda) - N_a(\lambda))\right] - \frac{1}{T_\infty}N_a(\lambda)\right\}, \tag{6.8}$$

with $C_a = 1 - C_b$, $C_{a,\infty} = 1$ and $C_{a,\infty} = 1$ (only component a presents in recording the comparison wave). For two different wavelengths λ_j and λ_k we get two equations from which the temperature and concentration distributions will be evaluated. These equations are the following

$$S(x,y,\lambda_j)\frac{\lambda_j}{\Delta N(\lambda_j)} - S(x,y,\lambda_k)\frac{\lambda_k}{\Delta N(\lambda_k)} = -\frac{T(x,y) - T_\infty}{T(x,y).T_\infty}\frac{3pl}{2R}\left[\frac{N_a(\lambda_j)}{\Delta N(\lambda_j)} - \frac{N_a(\lambda_k)}{\Delta N(\lambda_k)}\right], \tag{6.9}$$

$$S(x,y,\lambda_j)\frac{\lambda_j}{N_a(\lambda_j)} - S(x,y,\lambda_k)\frac{\lambda_k}{N_a(\lambda_j)} = \left[\frac{C(x,y)}{T(x,y)} - \frac{C_\infty}{T_\infty}\right].\frac{3pl}{2R}\left[\frac{\Delta N(\lambda_j)}{N_a(\lambda_j)} - \frac{\Delta N(\lambda_k)}{N_a(\lambda_k)}\right], \tag{6.10}$$

where $\Delta N(\lambda) = N_a(\lambda) - N_b(\lambda)$.

Figure 6.4 demonstrates how to evaluate the temperature profile, $T(y)$, and the concentration profile, $C(y)$, from two interferograms of a boundary layer produced by two different wavelengths, λ_j and λ_k [58]. For a specified direction along the boundary layer, x = constant, Fig. 6.4b shows S_j, S_k, $S_j.\lambda_j$ and $S_k.\lambda_k$ as functions of y, where $S_j = S(x = \text{const.}, y, \lambda_j)$ and $S_j = S(x = \text{const.}, y, \lambda_j)$. According to Eqs. (6.9) and (6.10) the temperature and concentration profiles at a location are found by the following equations

$$T(y) - T_\infty \approx \frac{S_j \cdot \lambda_j}{\Delta N_j} - \frac{S_k \cdot \lambda_k}{\Delta N_k}, \tag{6.11}$$

$$C(y) - C_\infty \approx \frac{S_j \cdot \lambda_j}{N_j} - \frac{S_k \cdot \lambda_k}{N_k}, \tag{6.12}$$

where $N_j = N_a(\lambda_j)$ and $N_k = N_a(\lambda_k)$. Figures 6.4c and 6.4e show the variations of $S \cdot \lambda / \Delta N$ and $S \cdot \lambda / N$ for λ_j and λ_k. Then using these distributions, Eqs. (6.11) and (6.12) yield the temperature and concentration profiles for that location. These profiles are shown in Figs. 6.4d and 6.4f.

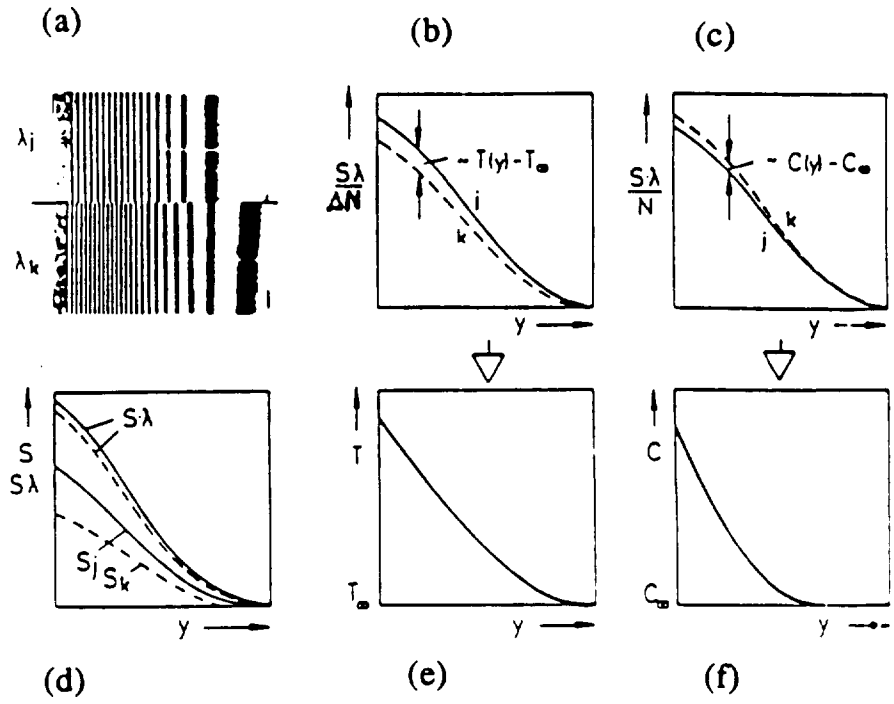

Fig. 6.4 Evaluation of interferograms [58]

a) interferograms for λ_j and λ_k

b) phase lag $S \cdot \lambda, S$

c), e) difference of modified phase lags

d), f) temperature and concentration profiles

6.3.3 *Laser Doppler Anemometry*

The laser Doppler anemometry allows the measurement of the local, instantaneous velocity of tracer particles suspended in a flow without disturbing the flow. Thus, appropriate particles must exist in the fluid and the relationship between the particles and

fluid velocity must be known. The task of a laser Doppler anemometer falls into three parts.

- Generating two coherent laser beams which interfere in a probe volume
- Detecting the light intensity scattered by tracer particles crossing the measuring control volume
- Analyzing the Doppler frequency and calculating the velocity of the particles

Figure 6.5 shows the required components of a laser Doppler anemometer and the following is a brief description of the basic principles of laser Doppler anemometry which are carefully outlined in Durst et al. [59].

Two coherent laser beams with wavelength λ and a diameter d form an ellipsoidal volume at the beam intersection point (see Figs. 6.6 and 6.7). The size of the measuring control volume is given by

$$\delta_x = d, \qquad \delta_y = \frac{d}{sin\phi}, \qquad \delta_z = \frac{d}{cos\phi}, \tag{6.13}$$

where ϕ is the angle between the two beams and δ_x ,δ_y and δ_z are the axes of the ellipsoid. Figure 6.7 shows the principles of the "interference fringe" model which was proposed by Rudd [60].

Two coherent laser beams having plane wave fronts intersect at an angle, ϕ. This yields a pattern of plane interference fringes as

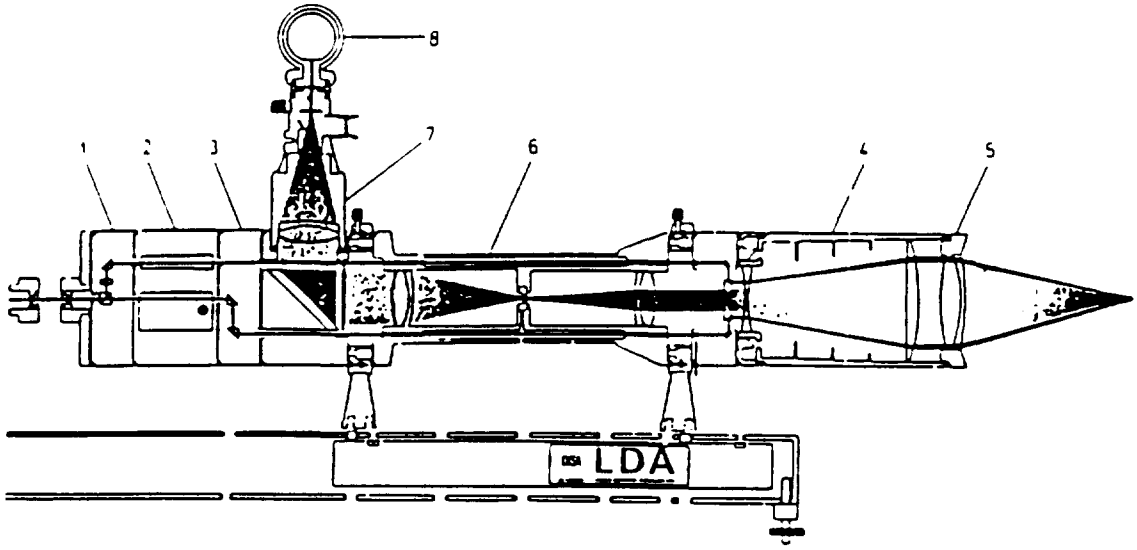

Fig. 6.5 LDA optics from DANTEC manual

1. beam splitter 2. bragg cell unit 3. beam displacer
4. beam expander 5. front lens 6. pinhole unit
7. photomultiplier optics 8. photomultiplier

shown in Fig. 6.7. The fringe spacing , Δz, is proportional to the wavelength, λ, of the light and inversely proportional to the half angle between two beams

$$\Delta z = \frac{\lambda}{2sin(\phi / 2)}. \tag{6.14}$$

As a particle moves through the region of interference fringes it will scatter light whose intensity will vary according to the light

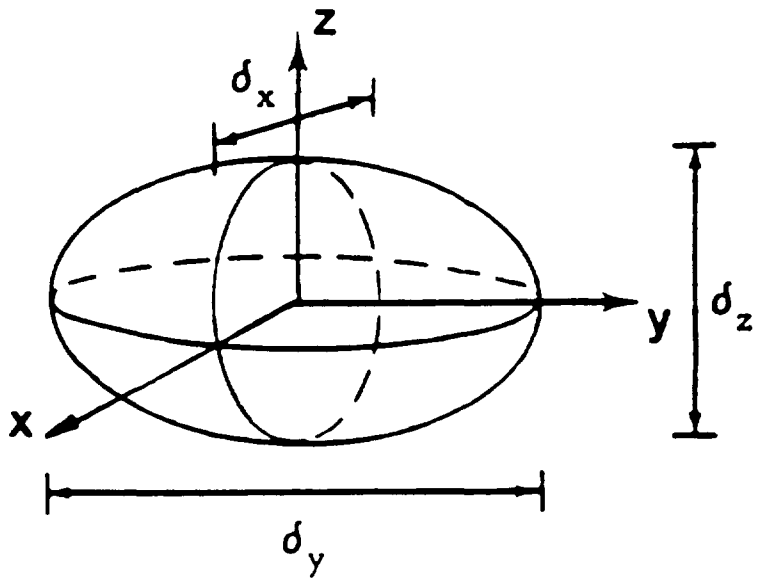

Fig. 6.6 Measuring control volume

intensity variation inside the bisector of the two beams. These light intensity variations have the Doppler frequency ν_D given by

$$\nu_D = \frac{U}{\Delta z} = \frac{2U\sin(\phi/2)}{\lambda}, \tag{6.15}$$

where U is the particle velocity component perpendicular to the fringes.

The scattered light is detected by a photomultiplier and the velocity component normal to the interference fringes is determined by analyzing the Doppler frequency. This frequency is ambiguous because it does not indicate in which direction a

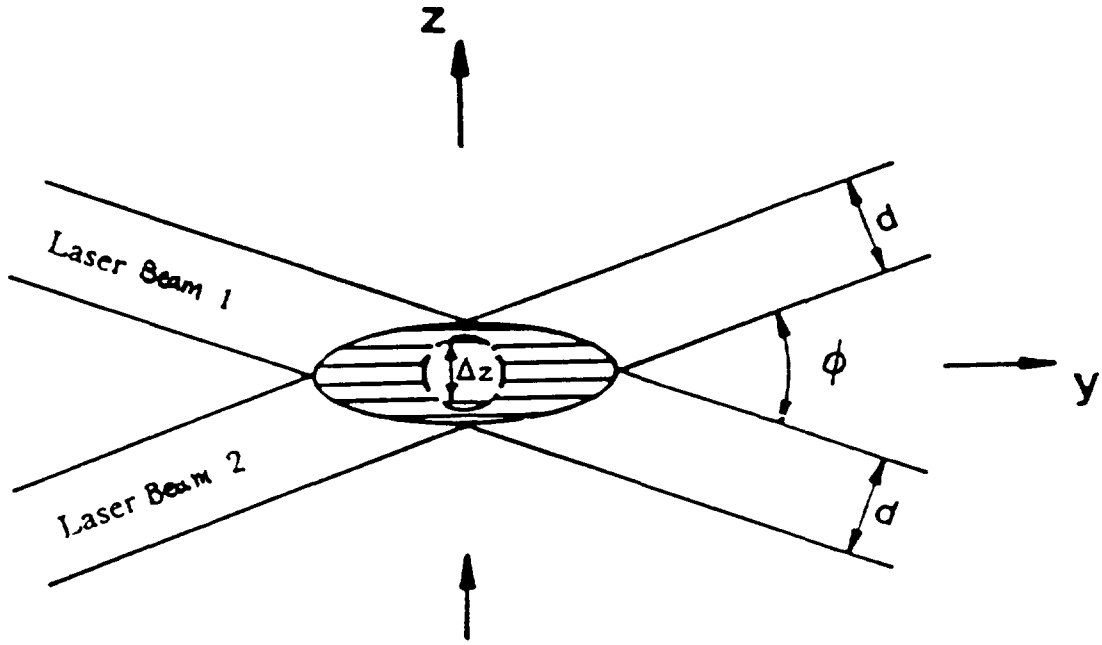

Fig. 6.7 Interference fringes in the control volume

particle moves. This lack of information can yield large errors if the flow direction is not known (e.g. in case of recirculating flow) or if the mean velocity is near-zero and the fluctuations are larger than the mean value in turbulent flow.

Frequency shifting allows the 180 degree ambiguity in the direction of a measured velocity to be resolved. The frequency shift is obtained when the two intersecting laser-beams have different frequencies. The presence of a frequency difference, ν_S,, results in a movement of the fringe pattern with velocity U_S,

$$U_s = -\nu_s \Delta z \ . \tag{6.16}$$

A frequency shift, applied to one of the laser beams, will result in an increase or decrease in the measured velocity of a particle depending on the direction of the movement. In this case the velocity can be determined clearly from the detected Doppler frequency, v_D,. If the velocity of the fringes, caused by the shift frequency, is greater than the particle velocity, then

$$U = (v_D - v_s)\frac{\lambda}{2sin(\phi / 2)}. \tag{6.17}$$

A lower Doppler-frequency than the shift frequency indicates that a particle moves in the same direction as the fringe pattern. If a particle moves in the opposite direction, the Doppler frequency will be larger than the shift frequency.

Laser Doppler anemometry depends on signals from particles suspended in the flow. Thus, it is important to know how well the motion of the particles represent the motion of the fluid. In our case there are two reasons for velocity differences:

- The particle terminal velocity is different from the vapor velocity because of greater gravitational forces on the particle as compared to the vapor.
- Drag forces caused by accelerations and velocity fluctuations can result in particle/vapor mismatch.

According to Tchen [61] the terminal velocity, C_t, of a particle in a fluid with the constant velocity U_f parallel to the gravity g is

$$U_p = U_f - C_t, \tag{6.18}$$

where

$$C_t = \frac{2}{g}\frac{r_p^2}{\mu_f}(\rho_p - \rho_f). \tag{6.19}$$

The velocity difference C_t between the particle velocity, U_p, and the fluid velocity, U_f, depends on the density difference, $(\rho_p - \rho_f)$, the viscosity of the fluid, μ_f, and the squared radius of the particles, r_p^2. For oil droplets ($r_p \approx 1$ μm) in gas, at standard state, $C_t \approx 1.5 \times 10^{-4}$ m/s.

According to Dring [62] the velocity difference between a particle and fluid caused by high-frequency velocity oscillations, depends on the Stokes number

$$St = \frac{\rho_p \omega 4 r_p}{18 \mu_f}. \tag{6.20}$$

For Stokes number $St < 0.14$ the particles follow an oscillation with the frequency ω with less than 1% velocity difference. For oil droplets in a gas, at standard states, $\omega_{max} \approx 12$ kHz.

6.4 PRELIMINARY RESULTS

Experiments have been carried out to visualize the vapor flow patterns in evaporation, adiabatic and condensation regions of the heat pipe after a sudden increase in input heat flux has been applied. A boundary layer of vapor is established very quickly on top of the wick surface all over the heat pipe. The thickness of this layer decreases from the evaporation section to the condensation region. The vapor boundary layer grows quickly and fills the whole space. Depending on the input heat flux, the whole process takes place in a few seconds. For low input heat flux, the vapor flow is found to be smooth and laminar. For higher heat fluxes the vapor boundary layer grows faster. If the input heat was high enough a few regular vortices were observed on top of the evaporation part and they expanded to the entrance region of the adiabatic part. The vapor flow in the adiabatic and condensation regions under a high heat flux are still laminar but reverse flow on top of the condenser is suspected.

6.5 DRYOUT AND REWET OF THE WICK STRUCTURE

A major limitation in the operation of heat pipes is wick dryout. The dry region of the wick will heat up, maybe even overheat, and therefore be difficult to rewet. The forces resisting dryout and augmenting rewet need to be determined before one can model a heat pipe to study its operational characteristics. Our search for data led us to conclude that it would be instructive to

first examine dryout and rewet of a thin film of fluid flowing over a flat, inclined plate, heated from below.

The stability of thin films flowing over both heated and unheated surfaces has been extensively studied. Yih [63] and Benjamin [64] analytically studied the purely fluid mechanical problem in the absence of any heat load. The neutral-stability curves obtained by Benjamin [64] show that free-surface flows down a vertical plane are unstable for all Reynolds numbers. Later, Bankoff [65], starting with a perturbation procedure provided by Yih [66], studied the combined fluid mechanical and heat transfer problem. In his study evaporation from the surface of a falling liquid film was found to have a destabilizing effect.

The stability of a dry spot, once it occurs, has been analyzed by several investigators. Murgatroyd [67], Zuber and Staub [68], and McPherson and Murgatroyd [69] predicted conditions under which a dry spot becomes stable. This was usually achieved by means of a force balance in which the pressure developed at the upstream stagnation point of a dryout region, the thermocapillary force developed as a result of the variation of surface tension with surface temperature, and other forces were taken into account.

When a liquid film becomes ultra thin, long range molecular forces become significant and must be integrated with continuum mechanics in an analysis of dryout or rewet. Bankoff [70] studied ultra thin films analytically and found that nonlinear wave theory,

bifurcation theory, and asymptotics all contribute to our understanding of the dynamics of dryout and rewet.

Experimental studies of dryout and rewet in thin films flowing over a flat plate are rare. Orell and Bankoff [71] studied the formation of a dry spot in a non-boiling, thin film of ethanol on a horizontal surface subject to a slowly increasing heat flux. It was found that noticeable thinning of the film occurred prior to rupture and that the heat flux at which rewet occurred was, on the average, 30% less than the heat flux needed for dryout at the same film thickness and flow rate. It was noted that the flow rate had a significant effect on the heat flux required for dryout, but this trend was not formally investigated.

In this section we focus on the effects of film thickness, flow rate, and inclination angle on the minimum heat flux required for dryout and the maximum heat flux allowed for rewet.

6.5.1 *Experimental Setup*

Fig. 6.8 shows the schematics of the experimental setup. The apparatus consists mainly of a flat copper plate whose dimensions are 35.5 cm x 15.2 cm x 0.24 cm. By adjusting the stopcock on an Oppenheimer tube mounted above the upper reservoir, we can control the flow rate through the knife edge gap. This gap is set between 0.025 mm and 0.080 mm depending on the fluid viscosity and the desired film thickness.

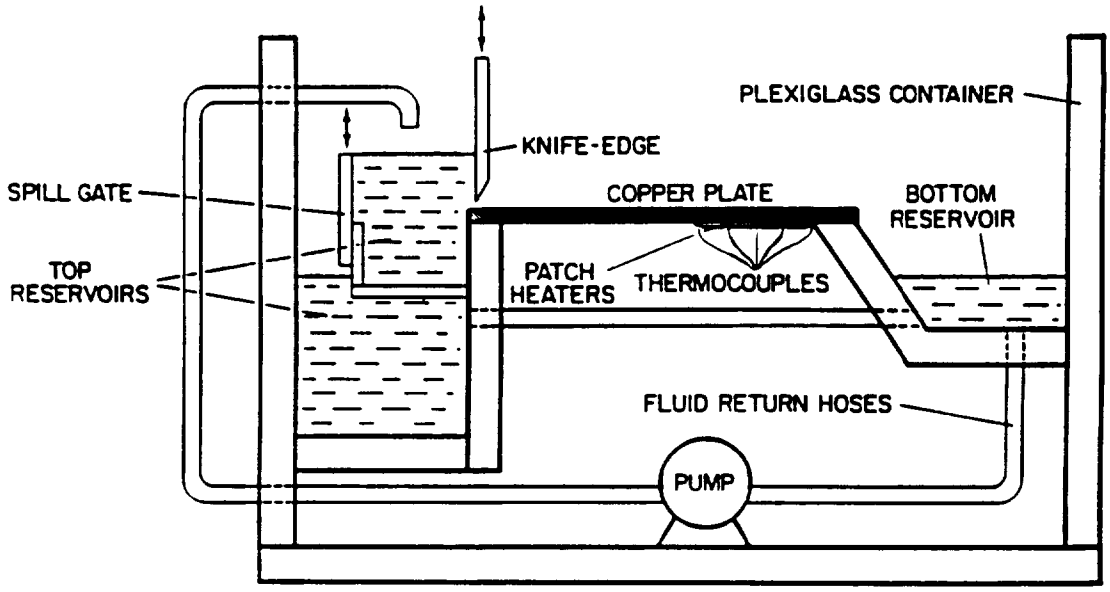

Fig. 6.8 Schematic of film dryout experiment

The last 11.4 cm of the plate constitutes the heated zone. Heat flux is provided by four 12.7 cm x 2.5 cm patch heaters which are capable of delivering 1.55 W/cm^2 at 115V. The plate temperature in this region is monitored using 15 copper-constantin thermocouples mounted 0.5 mm from the upper surface of the plate.

The thickness of the films is measured using a micrometer head with a 30^o point. This micrometer is mounted just above the surface of the fluid in the center of the heated region. Film thickness can be measured to within ±0.02 mm in this fashion.

6.5.2 *Preliminary Results*

The fluids used to form thin films exhibited very different physical characteristics. During the course of experimentation, three general mechanisms of dryout were observed. The first of these is dryout due to rupture. This mechanism occurred when water was used as the working fluid. No thinning of the film is observed when the heat flux is applied. Sometimes a small wave develops just upstream of the heated zone. Ripples are apparent in the fluid over the patch heaters. Once the plate temperature exceeds a certain value, the film becomes very unstable and any small disturbance can trigger dryout. If no disturbance occurs, rupture is eventually induced purely by heat input. Dryout is very rapid when induced by heat input and spreads over large portions of the plate in a very short time. This mechanism is probably controlled by surface tension since this parameter is much larger in water than in the other fluids used.

The second mechanism observed was dryout caused by instability due to surface waves. This mode is most apparent when using ethanol and Freon. Dryout occurs as follows: When heat is applied to the film waves appear on the surface. The film is thinner at the troughs of these waves so the evaporation rate is greater there. Vapor leaving the surface exerts a reactive force down onto the fluid which tends to deepen troughs and increase wave amplitude. Waves continue to grow until the film is thin

enough in some area that a dry spot occurs. This dry area spreads until equilibrium is reached.

The third mode is dryout due to gradual thinning. This mechanism was observed with ethanol, methanol and Freon. In this case, when heat flux is applied to the film, it begins to thin in a progressive manner. This thinning goes on until only a micro-thin layer of fluid is left on the plate. The thin micro-layer then spreads in the same way as a dryout. In fact, it is sometimes difficult to tell that the plate is still wet. If heat is applied long enough this micro-layer can also be burned off, however, this makes rewetting the plate much more difficult. This dryout mode seems to be dependent on inter-molecular forces such as London and Van der Waal's forces.

Distilled water and tap water proved to be the most difficult fluids with which to create thin films. Water did not automatically wet the plate, as did the Freon TF. Water runs down the plate in small irregular streams unless forced to do otherwise. To create a thin film with water, it was necessary to first flood the plate and then slowly drain away excess fluid until only a thin layer remained.

Once dryout occurred with water, it did not spread outward in a uniform way. Instead, the dried out regions moved about in a chaotic fashion. With standard tap water, dryout would usually encompass the entire heated zone, as would be expected. However, when distilled water was used as the working fluid,

dryout would spread over the entire plate in a very short amount of time. Thin films formed with distilled water were found to be the most unstable.

Methanol was another fluid which would not always wet the plate of its own accord. But here, the fluid could be made to form a thin film by wetting dry regions with a squirt bottle. Films of methanol were more stable than those formed with either tap or distilled water. They could only be ruptured through application of a heat flux. The other alcohol that was used was denatured ethanol. This fluid wet the plate naturally. To form a thin film of ethanol, it was only necessary to fill the reservoir at the leading edge of the plate. This was also the case for Freon TF, which was the fluid most willing to wet the plate.

Those fluids which did not willingly wet the surface of the plate were also the ones which had the most trouble rewetting the plate after dryout had been caused by a heat input. Neither tap water nor distilled water would ever rewet the plate, even after the entire system had returned to room temperature. Methanol would rewet sometimes, but other times it would leave behind small patches that could not rewet naturally. Methanol was generally unpredictable in its behavior and was very sensitive to factors such as impurities on the plate or ambient humidity. For this reason, it was not used in acquiring data. Distilled water was not used because of its extremely unstable film characteristics.

Freon TF and ethanol both rewet the dried areas in the same gradual fashion although Freon did so more rapidly.

The contact angles exhibited by the various fluids varied greatly. Although no provision was made to accurately measure contact angles, differences were obvious through observation. Distilled water and tap water formed contact angles in excess of 90 degrees while Freon TF maintained almost a zero contact angle. The contact angles for ethanol and methanol were also very small.

Perhaps as a result of its large contact angle, water did not form micro-layers. Dryout was complete in all cases, with no residue being left behind on dried areas. On the other hand, Freon TF and ethanol did form micro-layers. This behavior is not the same as that observed by Mirzamoghadam and Catton [72] in their studies of meniscus behavior.

In order to obtain a complete set of data, experiments were conducted while maintaining constant flow rate, constant film thickness, or constant angle of inclination for each of the fluids; water, denatured ethanol, methanol, and Freon TF. The thermophysical properties of these fluids are listed in Table 6.I. The method for maintaining the film at a constant thickness while varying the angle of inclination was as follows. At any given angle, increasing the level of head in the upper fluid reservoir produced a corresponding increase in the flow rate and film thickness. Thus, at each of the three angles of inclination used, the head in the upper reservoir was adjusted to produce the constant film

Table 6.I Thermal Properties of the Working Fluids

Fluid	*Freon TF*	*Ethanol*	*Methanol*	*Water*
Viscosity (cp)	*0.682*	*1.773*	*0.82*	*1.798*
Density (g/cm^3)	*1.56*	*0.791*	*0.810*	*1.00*
Surface Tension (dynes/cm)	*17.3*	*24.05*	*24.49*	*73.05*
Latent Heat ($x10^6$ J/kg)	*0.147*	*0.949*	*1.21*	*2.68*
Thermal Conductivity (W/mK)	*0.070*	*0.182*	*0.215*	*0.650*

thickness desired. The results for constant flow rates are shown in Table 6.II, while Tables 6.III and 6.IV show the results for constant film thicknesses and constant inclination angles, respectively. For accuracy and repeatability, all film thickness and flow rate measurements were made while maintaining the plate temperature at 25°C.

Constant Flow Rate

For the cases using a constant flow rate, the magnitude of the flow was different for each fluid. Because of variations in viscosity, wettability, and dryout heat fluxes, each fluid had a different flow rate which could be kept constant while varying the angle of inclination. Water required a flow rate of 0.89 ml/s while ethanol only required 0.26 ml/sec. A flow rate of 0.58 ml/s was required for Freon TF. While keeping the flow rate constant, Freon TF and ethanol exhibited similar patterns in that both the heat flux and plate temperature at dryout increased as the inclination angle decreased, as shown in Table 6.II. The opposite was true for water at constant flow rate which required an increase in heat flux and plate temperature as the angle was increased. This happened in spite of the fact that the film thickness decreased with increasing angle for all three fluids. The dryout heat fluxes for Freon TF ranged from 1.06 W/cm^2 on the horizontal plate to 0.45 W/cm^2 on the plate with a 5 degree inclination with plate temperatures at dryout ranging from 68°C to

Table 6.II Dryout and Rewet Heat Fluxes; Constant Flow Rate

Fluid	*Flow Rate (ml/sec)*	*Thickness (mm)*	*Angle*	q''_{dryout} W/cm^2	T_{dryout} $^{\circ}C$	q''_{rewet} W/cm^2	T_{rewet} $^{\circ}C$
Freon TF	*0.58*	*0.47*	*0.0°*	*1.06*	*68*	*0.53*	*57*
		0.27	*2.5°*	*0.51*	*50*	*0.37*	*48*
		0.20	*5.0°*	*0.45*	*45*	*0.25*	*41*
Ethanol	*0.26*	*0.58*	*0.0°*	*1.27*	*78*	*0.87*	*68*
		0.28	*2.5°*	*1.13*	*70*	*0.81*	*62*
		0.24	*5.0°*	*1.04*	*67*	*0.71*	*56*
Water	*0.89*	*0.52*	*0.0°*	*0.95*	*61*	-	-
		0.31	*2.5°*	*1.55*	*81*	-	-
		0.27	*5.0°*	*1.83*	*92*	-	-

45°C. Similarly, ethanol's dryout heat fluxes and plate temperatures ranged from 1.27 W/cm^2 to 1.04 W/cm^2 and 78°C to 67°C, respectively. The values for water, however, increased from 0.95 W/cm^2 on the horizontal plate to 1.83 W/cm^2 on the plate inclined at 5 degrees and at 92°C.

Rewet heat fluxes for ethanol and Freon TF followed a pattern similar to that of dryout. Increasing the angle of inclination led to a decrease in the heat flux which would allow rewet to occur. As with dryout, this seems reasonable since higher angles produce thinner films if the flow rate is held constant. With Freon heat fluxes for rewet ranged from 0.53 W/cm^2 at 57°C to 0.25 W/cm^2 at 41°C. Ethanol rewet the horizontal plate at 0.87 W/cm^2 at 68°C whereas 0.71 W/cm^2 at 56°C was the rewet limit on the 5 degree inclined plate. As mentioned before, water did not rewet the plate under any circumstances. Therefore, no rewet data is available in this case.

Constant Film Thickness

The flow rates needed to maintain constant film thickness, along with corresponding dryout and rewet heat flux data, are shown in Table 6.III. Thicknesses of approximately 0.3 mm were used for the different fluid films. All three fluids behaved similarly under the constant thickness constraint. As the angle of the plate was increased, the heat flux needed for dryout also increased. For Freon TF and water, the plate temperature also

Table 6.III Dryout and Rewet Heat Fluxes; Constant Film Thickness

Fluid	*Flow Rate (ml/sec)*	*Thickness (mm)*	*Angle*	q''_{dryout} W/cm^2	T_{dryout} $^{\circ}C$	q''_{rewet} W/cm^2	T_{rewet} $^{\circ}C$
Freon TF	*0.06*	*0.29*	*0.0°*	*0.32*	*38*	*0.19*	*35*
	0.71		*2.5°*	*0.42*	*45*	*0.32*	*43*
	1.11		*5.0°*	*0.61*	*49*	*0.37*	*44*
Ethanol	-	*0.30*	*0.0°*	-	-	-	-
	0.28		*2.5°*	*1.22*	*76*	*0.91*	*67*
	0.36		*5.0°*	*1.29*	*74*	*0.91*	*62*
Water	-	*0.31*	*0.0°*	-	-	-	-
	0.67		*1.2°*	*0.57*	*51*	-	-
	0.93		*2.5°*	*1.55*	*80*	-	-

increased with increasing angle and heat flux, while for ethanol, the plate temperature for the higher heat flux case was actually less at dryout than for the lower heat flux case. This was also the case for rewet temperatures. In examining films of water and ethanol at constant thickness, the horizontal angle of inclination was not included. Even with near zero flow rates, the horizontal films could not be made as thin as the thickest film achievable at five degrees inclination. Thus one constant thickness could not be produced at all three plate angles being observed. For this reason, data for water and ethanol at constant film thickness includes only the 2.5 and 5.0 degree inclinations. Heat fluxes and plate temperatures for dryout varied from 0.32 W/cm^2 at 38°C for Freon TF on the horizontal plate to 1.55 W/cm^2 at 80°C for water on the 5 degree inclined plate. The lowest values for rewet were 0.19 W/cm^2 at 35°C which occurred on the horizontal film of Freon TF, whereas the highest values of 0.91 W/cm^2 at 67°C occurred on a film of ethanol at a 5 degree inclination.

Constant Angle of Inclination

Table 6.IV gives the results for fluid films at constant angles. These results simulate a wicking material which exerts a constant capillary force on the working fluid. All three fluids exhibit the same pattern of increased heat fluxes and plate temperatures required for dryout as the flow rates and thicknesses are increased. Freon TF and ethanol were both run at 2.5 degree

Table 6.IV Dryout and Rewet Heat Fluxes; Constant Inclination Angle

Fluid	*Flow Rate (ml/sec)*	*Thickness (mm)*	*Angle*	q''_{dryout} W/cm^2	T_{dryout} $^{\circ}C$	q''_{rewet} W/cm^2	T_{rewet} $^{\circ}C$
Freon TF	*0.43*	*0.27*	*2.5°*	*0.38*	*45*	*0.28*	*43*
	0.71	*0.28*		*0.42*	*45*	*0.32*	*43*
	0.80	*0.30*		*0.51*	*50*	*0.38*	*47*
Ethanol	*0.31*	*0.27*	*2.5°*	*0.71*	*54*	*0.48*	*52*
	0.52	*0.30*		*0.91*	*63*	*0.68*	*56*
	0.71	*0.31*		*1.08*	*70*	*0.77*	*62*
Water	*0.74*	*0.31*	*1.2°*	*0.57*	*51*	-	-
	0.93	*0.33*		*0.75*	*55*	-	-
	1.79	*0.45*		*1.06*	*64*	-	-

inclines whereas water was run at a 1.2 degree slope. The decreased angle for water was necessary so that a wide variety of flow rates could be examined while still allowing dryout, given our heat flux limit. The thicknesses of all of the films were approximately 0.3 mm with the exception of water at high flow rate, in which case the film was 0.45 mm thick. The lowest values of heat flux and plate temperature for dryout were 0.38 W/cm^2 at 45°C for Freon while the highest values were 1.08 W/cm^2 at 70°C for ethanol. Rewet heat fluxes ranged from 0.28 W/cm^2 to 0.77 W/cm^2 at 43°C and 62°C, respectively.

6.5.3 *Conclusions*

The various fluids used to form thin films displayed very different characteristics under dryout conditions. Although dry patches were formed through input heat flux, the stability of the dry patches was largely affected by the liquid contact angle. The problem is dynamic, since dry patches are constantly changing shape. One must therefore consider the moving contact line. A generally accepted formula for predicting dynamic contact angles has yet to be proposed although Orell and Bankoff [71] proposed two methods for approximating a static contact angle. Experimental measurements of dynamic contact angles usually involve direct observation through magnification.

Some dimensionless parameters related to the dynamic contact angle were suggested by Dussan [73]. These include the

Reynolds, Bond, Weber, and capillary number, and the static contact angle. Contact angle hysteresis must also be considered. Hysteresis is affected by surface roughness and is not easily predicted.

Wettability of a fluid on a solid surface is not determined solely by the contact angle. It was found that although ethanol easily rewet the copper plate used in the experiment, methanol would not naturally wet the plate. But the contact angles for these two fluids appear similar upon observation. Using the formula suggested by Orell and Bankoff [71] the static contact angles for the two fluids are within one percent. There seem to be many factors contributing to dryout and rewet, and none of them can be considered separately.

6.6 CONCLUDING REMARKS

Transient processes in the vapor core of heat pipes are very fast (few seconds). Therefore, the mentioned optical methods which provide inertialess measurements, are the proper tools to obtain accurate results. The temperature and concentration profiles are evaluated from the holograms developed by the twin beam interferometry. In this method, the temperature is evaluated from the difference between the phase shifts corresponding to two different wavelengths (see Eq. (6.11)). This difference is usually very small, therefor, the two wavelengths used should be as far apart as possible.

In laser Doppler anemometry, seeding of particles with proper density and size is a challenging problem. In systems like heat pipes, in which the working fluid undergoes a phase change, it is not possible to have particles recirculating with the fluid flow. In this case, particles can be carefully injected into the vapor flow in the evaporation end and collected from the condensation end. But the disadvantage of this technique is that the measured velocities at both
ends are not accurate.

When the evaporation and condensation rates are high (more than 1 w/cm^2), small liquid droplets with radius of order of 1 μm are present in the vapor flow. These droplets flow with the vapor and are able to scatter the laser beam. Therefore, no seeding is required in this case.

There are several difficulties with the use of optical methods in heat pipe vapor flow measurements. Although these methods are very accurate and reliable, they are however, very expensive. The optical components are also very sensitive and not durable. Furthermore, the alignment of the laser beams passing through different parts of the measurement setup (specially in the laser Doppler anemometry), is hard to be achieved and easy to be lost.

The major problem in the experiments, on the other hand, is the condensation of the vapor on the side walls of the rectangular pipe. A liquid film is formed on the walls, which disturbs the laser beam passing through the vapor core. and causes beam reflection.

The unwanted condensation film was reduced by making the side walls out of acrylic plate which has very low thermal conductivity. The heat lost through the walls was highly reduced and, consequently, the condensation was confined to a smaller area closer to the liquid layer. In order to further reduce the condensation film, the Crystal Blue anti-fog jelly was coated on the internal surfaces of the acrylic walls.

Chapter VII
SUMMARY AND CONCLUSIONS

The transient behavior of a heat pipe vapor flow is an important component of its operation and response to variable loading conditions. However, a simple model is needed in the thermal management of systems which use heat pipes as the heat transfer medium. A comprehensive experimental and theoretical research is needed to backup and verify the simple model. This study investigates the detailed dynamics of the vapor flow in heat pipes. A complete model will combine this work with studies of the liquid phase.

The vapor flow in heat pipes is modeled and the governing equations are derived for transient two-dimensional compressible flow along with inflow and outflow boundary conditions. The equations are solved numerically for two cases; operating and startup transients. In the study of the steady state and operating transients after a sudden increase in the input heat flux, it is shown that for high-input heat fluxes, flow reversal occurs in the adiabatic and condensation regions. The circulation flow is caused

by injection and extraction of a high momentum flow in the evaporator and condenser, respectively.

During the startup transient in heat pipes, if the initial static state is at a very low pressure (which is most likely in aerospace applications), a high-input heat flux will create a shock wave in the evaporator. A nonlinear filtering technique is therefore used to capture the shock and overcome the cell Reynolds-number stability problem as a result of high velocity flow. Multiple shock reflections in the evaporator causes periodic oscillations in the pressure and, consequently, the pressure drops along the heat pipe. Depending on the transient time constant of the liquid layer and how fast the input heat reaches the vapor, the pressure drop in the vapor core may be significantly higher than its value in the steady state operation for the same input heat flux. Furthermore, the shock reflection causes a pressure increase in the evaporator. If the pressure exceeds the saturation pressure, mist nucleation will occur which will affect the evaporation rate.

The optical methods are found to be the most appropriate and unique for temperature and velocity measurements in the vapor flow in heat pipes. Although these methods are very accurate, they are very sensitive and difficult to work with. The alternative approach would probably be to build a cylindrical heat pipe and to measure the input heat flux and the corresponding surface temperature after a sudden increase in the input heat flux. The standard and simple measurement technique, like

thermocouples, could be used. Then the experimental results would verify the results of the analysis which combine the vapor and liquid phases as well as the heat pipe case. This study is left for future efforts.

REFERENCES

1. Gaugler, R. S., *Heat Transfer Device*, US Patent No. 2,350,348, 1942.
2. Grover, G. M., Cotter, T. P., and Erickson, G. F., "Structures of Very High Thermal Conductance," *J. Appl. Phys.*, Vol. 35, No. 6, pp 1990-1991, 1964.
3. Cotter, T. P., "Theory of Heat Pipes," *LA - 3246 - MS*, 1965.
4. Ranken, W. A., "Heat Pipe Development for the SPAR Space Power System," in *Advances in Heat Pipe Technology*, Reay, D. A., Ed., Pergamon Press, 1981.
5. Camarda, C. J., "Aerothermal Tests of a Heat-Pipe-Cooled Leading Edge at Mach 7, "*NASA-1320*, 1978.
6. DeMeis, R., "Heat Pipe Cooled Rockets," *Aerospace America*, Vol. 25, No. 3, 1987.
7. Dunn, P., and Reay, D. A., *Heat Pipes*, 3rd ed., Pergamon Press, London, 1982.
8. Chi, S. W., *Heat Pipe Theory and Practice: A Sourcebook*, Hemisphere, Washington, 1976.
9. Busse, C. A., "Heat Pipe Research in Europe," *Proc., 2nd Int. Conf. on Thermionic Electrical Power Generation*, Stresa, Italy, May 1968.

10. Levy, E. K., "Theoretical Investigation of Heat Pipes," *Proc., Aviation and Space Conf.*, Beverly Hills, California, pp 671-676, 1968.

11. Levy, E. K., "Effect of Friction on the Velocity Limit in Sodium Heat Pipes," *AIAA Paper No. 71-407*, 1971.

12. Edwards, D. K. and Marcus, B. D., "Heat and Mass Transfer in the Vicinity of the Vapor-Gas Front in a Gas-Loaded Heat Pipe," *J. Heat Transfer*, Vol. 94, No. 2, pp 155-162, 1972.

13. Brovalsky, Y. M., Bystrov, P. I., and Melkinov, M. V., "The Method of Calculation and Investigation of High-Temperature Heat Pipe Characteristics Taking into Account the Vapor Flow Compressibility, Friction and Velocity Profile," *Proc., 2nd Int. Heat Pipe Conf.*, pp 113-122, 1976.

14. Bankston, C. A. and Smith, H. J., "Incompressible Laminar Vapor Flow in Cylindrical Heat Pipes," *ASME Paper No. 71-WA/HT-15*, 1972.

15. Bankston, C. A. and Smith, H. J., "Vapor Flow in Cylindrical Heat Pipes," *J. Heat Transfer*, Vol. 95, No. 8, pp 371-376, 1973.

16. McDonald, J. W., Denny, V. E., and Mills, A. F., "Evaporation and Condensation in an Enclosure in the Presence of a Noncondensible Gas," in *Heat Transfer in Low Reynolds Number Flow, ASME, HTD*, Vol. 5, pp 1-11, 1971.

17. Rohani, A. R. and Tien, C. L., "Steady Two-Dimensional Heat and Mass Transfer in the Vapor-Gas Region of a Gas-Loaded Heat Pipe," *J. Heat Transfer*, Vol. 95, No. 5, pp 377-382, 1973.

18. Tien, C. L. and Rohani, A. R., "Analysis of the Effects of Vapor Pressure Drop on Heat Pipe performance," *Int. J. Heat Mass Transfer*, Vol. 17, pp 61-67, 1974.

19. Peterson, P. F. and Tien, C. L., "Gas-Concentration Measurements and Analysis for Gas-Loaded Thermosyphons," *Proc., Int. Symp. on Natural Circulation, ASME, HTD*, Boston, 1987.

20. Galaktionov, V. V., Parfenteva, A. A., Partnov, D. V., and Sasin, V. Y., "Vapor-Gas Front in the Condenser of a Two Dimensional Gas-Controlled Heat Pipe," *J. Eng. Phys.*, Vol. 42, pp 273-277, 1982.

21. Galaktionov, V. V. and Trukhanova, L. P., "Study of the Process of Heat and Mass Transfer in the Region of the Vapor-Gas Front in a Gas-Regulable Heat Pipe," *J. Eng. Phys.*, Vol. 48, pp 296-300, 1985.

22. Ooigen, H. V. and Hoogendoorm, C. J., "Vapor Flow Calculations in a Flat-Plate Heat Pipe," *AIAA J.*, Vol. 17, No. 11, pp 1251-1259, 1979.

23. Narayana, K. B., "Vapor Flow Characteristics of Selender Cylindrical Heat Pipes- A Numerical Approach," *Numerical Heat Transfer*, Vol. 10, pp 79-93, 1986.

24. Faghri, A., "Vapor Flow Analysis in a Double-Walled Concentric Heat Pipe," *Numerical Heat Transfer,* Vol. 10, pp 583-596,1986.

25. Merrigan, M. A., "Heat Pipe Technology Issues," *Proc., 1st Symposium on Space Nuclear Power Systems,* Orbit Book Co., pp 419-426, Florida, 1985.

26. Merrigan, M. A., "Heat Pipe Design for Space Power Heat Rejection Applications" *Proc., 21st Intersociety Energy Conversion Conf.,* pp 1993-1998, 1986.

27. Merrigan, M. A., Keddy, E. S., and Sena, J. T., "Transient Performance Investigation of a Space Power System Heat Pipe," *Proc., AIAA/ASME 4th Joint Thermophysics and Heat Transfer Conf.,* Boston, Mass., 1986.

28. Merrigan, M. A., Keddy, E. S., and Sena, J. T., "Transient Heat Pipe Investigations for Space Power System," *LA-UR-85-3341,* 1985.

29. Costello, F. A., Montague, A. F., and Merrigan, M. A., "Detailed Transient Model of a Liquid-Metal Heat Pipe," *Proc., AIAA/ASME 4th Joint Thermophysics and Heat Transfer Conf.,* Boston, Mass., 1986.

30. Amsden, A. A. and Harlow, F. H., "KACHINA: An Eulerian Computer Program for Multifield Fluid Flows," *LA-5680,* 1974.

31. Bystrov, P. I. and Goncharov, V. F., "Starting Dynamics of High Temperature Gas-Filled Heat Pipes," *High Temperature*, Vol. 21, pp 927-936, 1983.

32. Ivanovskii, M. N., Sorokin, V. P., and Yagodkin, I. V., *The Physical Principles of Heat Pipes*, Clarendon Press, Oxford, 1982.

33. Chang, W. S., "Heat Pipe Startup from the Supercritical State," *Ph.D. Dissertation*, Georgia Institute of Technology, 1981.

34. Colwell, G. T. and Chang, W. S., "Measurement of the Transient Behavior of a Capillary Structure Under Heavy Thermal Loading," *Int. J. Heat Mass Transfer*, Vol. 27, No. 4, pp 541-551,1984.

35. Chang, W. S. and Colwell, G. T., "Mathematical Modeling of the Transient Operating Characteristics of Low-Temperature Heat Pipe," *Numerical Heat Transfer*, Vol. 8, pp 169-189, 1985.

36. Ambrose, J. H., Chow, L. C., and Beam, J. E., "Transient Heat Pipe Response and Rewetting Behavior," *J. Thermophysics*, 1, pp 222-227, 1987.

37. Bowman, W. J., "Simulated Heat-Pipe Vapor Dynamics," *Ph.D. Dissertation*, Air Force Institute of Technology, 1987.

38. Jang, J. H., "An Analysis of Startup from the Frozen State and Transient Performance of Heat Pipes," *Ph.D. Thesis*, Georgia Institute of Technology, 1988.

39. Roche, G. L., "Analytical Studies of the Liquid Phase Transient Behavior of a High Temperature Heat Pipe," *M.Sc. Thesis*, University of California Los Angeles, 1988.

40. Issacci, F., Roche, G. L., Klein, D. B., and Catton, I., "Heat Pipe Vapor Dynamics," *Report, UCLA-ENG-88-28,* University of California Los Angeles, 1988.

41. Issacci, F., Catton, I., Heiss, A., and Ghoniem, N. M., "Analysis of Heat Pipe Vapor Flow Dynamics," *Chem. Eng. Comm.*, Vol. 85, pp 85-94, 1989.

42. Patankar, S. V., *Numerical Heat Transfer and Fluid Mechanics,* Hemispherical Publishing Co., New York, 1980.

43. Issacci, F., McDonough, J. M., Catton, I., and Ghoniem, N. M., "Non-linear Filtering for Shock Capturing and Cell-Reynolds Number Problems in Compressible Vapor Dynamics," submitted for publication in *J. Comp, Phys.*, 1990.

44. Serrin, J., "On the Stability of Viscous Fluid Motions," *Arch. Rational Mech. Anal.*, Vol. 1, pp 1-13, 1959.

45. Godunov, S. K. , "A Finite Difference Method for the Numerical Computation of Discontinuous Solutions of the Equations of Fluid Dynamics," *Math. Sb.*, Vol. 47, pp 271-290, 1959.

46. Harten, A., "High Resolution Schemes for Hyperbolic Conservation Laws," *J. Comp. Phys.*, Vol. 49, 357-393, 1983.

47. Chakravarthy, S. and Osher S., "Numerical Experiments with the Osher Upwind Scheme for the Euler Equations," *Proc. AIAA/ASME Joint Fluids, Plasma, Thermophysics and Heat Transfer Cont.*, St. Louis, Missouri, 1982.

48. Harten A. and Zwas G., "Switched Numerical Shuman Filters for Shock Calculations," *J. Engrg. Math*, Vol. 6, pp 207-216, 1972.

49. Engquist, B. Lötstedt, P., and Sjögreen, B., "Nonlinear Filters for Efficient Shock Computation," *J. Math. Comp.*, Vol. 52, No. 186, pp 509-537, 1989.

50. Courant, R., Isaacson, E., and Rees, M., "On the Solution of Non- Linear Hyperbolic Differential Equations by Finite Differences, *Comm. Pure Appl. Math.*, Vol. 5, pp 243, 1952.

51. Spalding, D. B., "A Novel Finite Difference Formulation for Differential Equations Involving Both First and Second Derivatives, *Int. J. Num. Methods Eng.*, 4, pp 551, 1972.

52. Patankar, S. V., "A Calculation Procedure for Two Dimensional Elliptic Situation," *Num. Heat Transfer*, Vol. 2, 1979.

53. Runchal, A. K., "CONDIF: A Modified Central-Difference Scheme for Convective Flows," *Int. J. Numer. Methods Eng.*, Vol. 24, No.8, pp 1593-1608, 1987.

54. Liepmann, H. W. and Roshko, A., *Elements of Gasdynamics*, John Wiley, New York, 1957.

55. Issacci, F., Catton, I., and Ghoniem, N. M., "Vapor Dynamics of Heat Pipe Startup," *Proc., 7th Sypm. on Space Nuclear Power Systems*, Vol. 2, pp 1002-1007, Albuquerque, NM, 1990.

56. Hauf, W. and Grigull, U., "Optical Methods in Heat Transfer," in *Advances in Heat Transfer*, Vol. 6, pp 134-366, 1970.

57. Mayinger F. and Panknin, W., "Holography in Heat and Mass Transfer," *Proc., 5th International Heat Transfer Conf.*, Vol. 6, pp 28-43, Japan, 1974.

58. Panknin, W., "Eine Holographische Zweiwellenlangen Interferometrie zur Messung uberlagerter Temperatur- und Konzentrationsgrenzschichten," *Ph.D. Thesis*, Technischen Universitat Hannover, Germany, 1977.

59. Durst, F., Melling, A., and Whitelaw, J. H., *Principles and Practice of Laser Doppler Anemometry*, Academic Press, New York, 1976.

60. Rudd, M. J., "A New Theoretical Method for the Laser Dopplermeter," *J. Phys. E:Sci. Instrum.*, Vol. 2, pp 55-59, 1969.

61. Tchen, C. M., "Mean Value and Correlation Problems Connected with the Motion of Small Particles Suspended in a Turbulent Fluid," *Ph.D. Thesis*, Delft, 1947.

62. Dring, R. P., "Sizing Criteria for Laser Anemometry Particles," *J. Fluids Engineering*, Vol. 104, pp 15-17, 1982.

63. Yih, C. S., "Stability of Parallel Laminar Flow with a Free Surface," *Proceedings, 2nd U.S. National Congress Appl. Mech., ASME*, pp 622-628, 1955.

64. Benjamin, T. B., "Wave Formation in Laminar Flow Down an Inclined Plane," *J. Fluid Mech.*, Vol. 2, pp 551-558, 1957.

65. Bankoff, S. G., "Stability of Liquid Flow Down a Heated Inclined Plane," *Int. J. Heat Mass Transfer*, Vol. 14, pp 377-385, 1971.

66. Yih, C. S., "Stability of Liquid Flow Down an Inclined Plane," *Physics Fluids*, Vol. 6, pp 321-327, 1963.

67. Murgatroyd, W., "The Role of Shear and Form Forces in the Stability of a Dry Patch in Two-Phase Film Flow," *Int. J. Heat Mass Transfer*, Vol. 8, pp 297, 1965.

68. Zuber, N. and Staub, F. W., "Stability of Dry Patches Forming in Liquid Films Flowing Over Heated Surfaces," *Int. J. Heat Mass Transfer*, Vol. 9, pp 897, 1966.

69. McPherson, G. D. and Murgatroyd, W., "Film Breakdown and Dryout in Two Phase Annular Flow," *Third Int. Heat Transfer Conf.*, Vol. 3, pp 111-122, Chicago, 1966.

70. Bankoff, S. G., "Dynamics and Stability of Thin Heated Liquid Films," 1987 Max Jacob Memorial Award Lecture, Houston, TX, 1987.

71. Orell, A. and Bankoff, S. G., "Formation of a Dry Spot in a Horizontal Liquid Film Heated From Below," *Int. J. Heat Mass Transfer*, Vol. 14, pp 1835- 1842, 1971.

72. Mirzamoghadam, A. and Catton, I., "Holographic Interferometry Investigation of Enhanced Tube Meniscus Behavior," *J. of Heat Transfer*, Vol. 110, pp 208-213, 1988.

73. Dussan, E. B., "On the Spreading of Liquids on Solid Surfaces: Static and Dynamic Contact Lines," *Ann. Rev. Fluid Mech.*, Vol. 11, pp 371-400, 1979.